NASA CR - 159485

NASA

MERCURY ION THRUSTER RESEARCH - 1978

PREPARED FOR

LEWIS RESEARCH CENTER

NATIONAL AERONAUTICS AND SPACE ADMINISTRATION

GRANT NGR-06-002-112

Annual Report

December 1978

Paul J. Wilbur
Department of Mechanical Engineering
Colorado State University
Fort Collins Colorado

TABLE OF CONTENTS

LIST OF FIGURES

LIST OF TABLES

PREDICTION OF PLASMA PROPERTIES IN MERCURY ION THRUSTERS

The work accomplished on the theoretical modelling of ion thruster processes is described in detail in Reference [1] and it will not be reproduced here. This model enables one to calculate discharge chamber plasma properties from basic thruster design data and controllable operating parameters.

CATHODE TEMPERATURE MEASUREMENTS ON THE SIT 8 THRUSTER

The SIT 8 thruster[2,3] was operated at its nominal discharge current, flow rate and high voltage operating conditions while the temperatures of its main and neutralizer cathode orifice plates were measured. The objective of the work was to determine if these cathode temperatures were sufficiently high to facilitate effective barium migration on the rolled tantalum foil inserts used in the cathodes. The interest in this question was stimulated by variations in the keeper characteristics of 8 cm dia thruster cathodes during operating tests.

Platinum/platinum-rhodium thermocouples were spot welded to the downstream side of the main and neutralizer cathode orifice plates. These thermocouples were installed by cutting and removing the downstream half of the enclosed keeper so a thermocouple, directed to the vicinity of the cathode tip through an aluminum oxide tube could be attached to the orifice plate. After the thermocouple had been installed the keeper was reassembled, the thruster was installed in the 1.5 m dia vacuum facility and tested. The keeper current levels and cathode heater powers were varied during the tests but the flow rates, discharge current, discharge-keeper voltage difference and the beam current remained essentially fixed. Figure 1 shows the variation in cathode tip temperature with cathode power for the main cathode. Two separate sets of curves are shown; the first one with circular data point symbols was obtained with cathode heater power only and is labelled "no discharge." The second set of curves were obtained at a mercury flow rate of 90 mA equiv, a discharge current of ∿0.6 A, a beam current of 0.072 A, a discharge-keeper

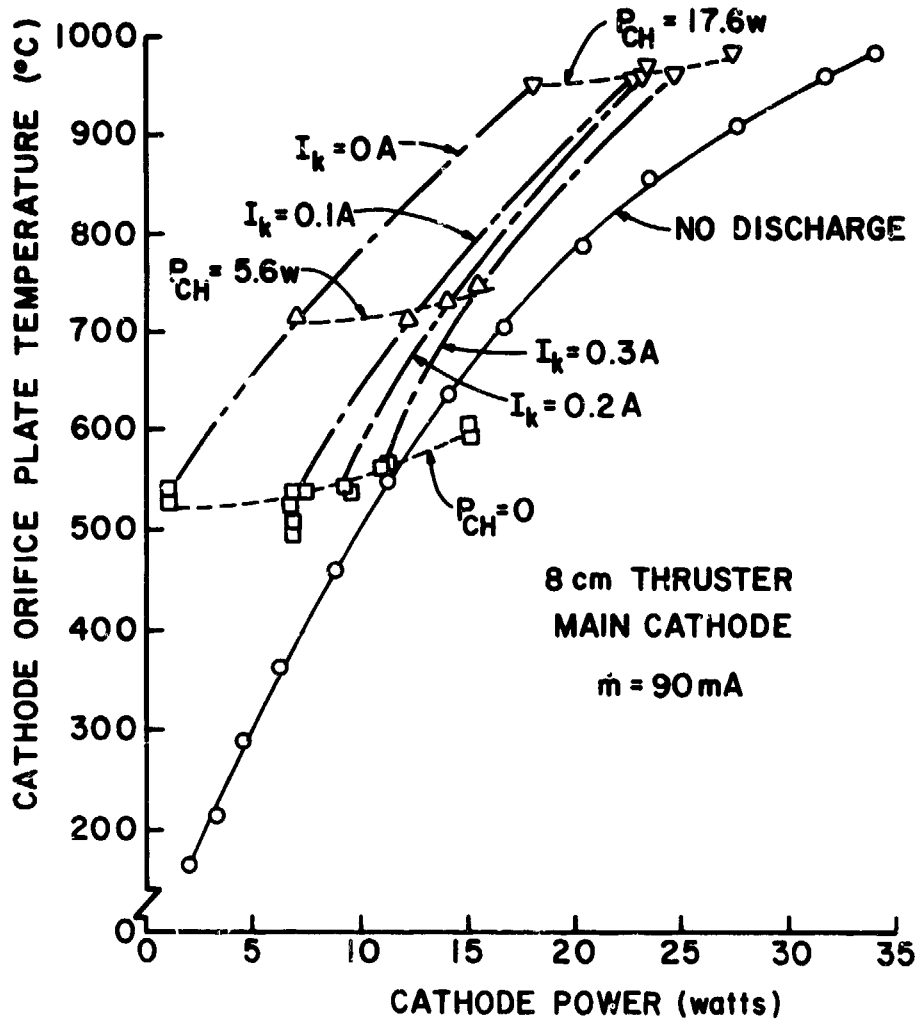

FIGURE 1. 8 CM THRUSTER MAIN CATHODE TIP TEMPERATURES

voltage difference of 29 V and the keeper currents (I_K) and cathode heater powers (P_{CH}) indicated on Figure 1. The cathode power (P_C) on the abscissa is calculated from the keeper current, keeper voltage (V_K), discharge current (I_D) and cathode heater power using the following expression:

$$P_C = P_{CH} + (I_D + I_K)\, V_K$$

Figure 1 shows that the orifice plate temperature is not influenced significantly by changes in keeper current that might reasonably be expected during the course of normal thruster operation. It also suggests that changes in cathode heater power do affect this temperature significantly and that at a cathode heater power of zero (normal operating condition) the orifice plate temperature is surprisingly low (500-600°C).

Figure 2 shows a plot of neutralizer cathode orifice plate temperature as a function of cathode power. These data also include a curve of temperature vs. cathode heater power where there was no discharge (circular symbols), as well as data obtained with the neutralizer operating. The data were all obtained at a 72 mA neutralizer emission current but at the two different flow rate conditions indicated on the figure. It was observed that flow rate changes over the range 6 mA to $\sim$ 15 mA did not affect the cathode orifice plate temperatures significantly.

The cathode power (P_C) was computed for these curves from the keeper current (I_K), the keeper voltage (V_K), the cathode heater power (P_{CH}) and the neutralizer current required to match the beam current (I_B) from the expression:

$$P_C = P_{CH} + (I_K + I_B)\, V_K$$

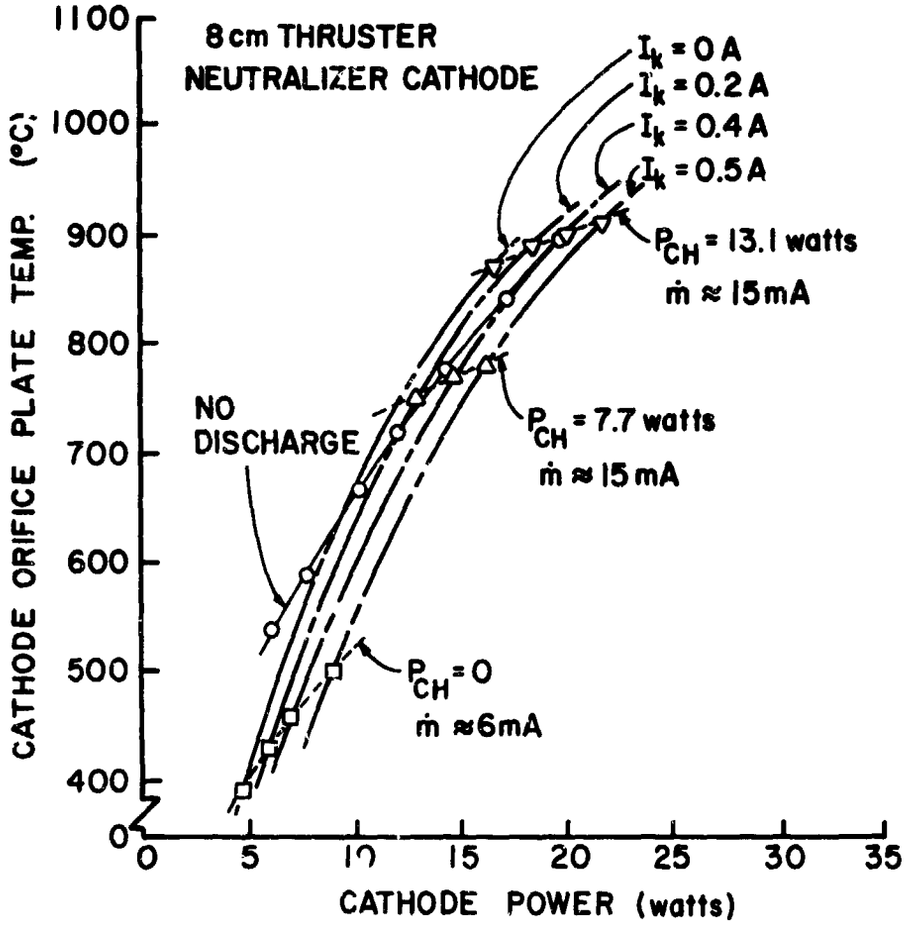

FIGURE 2. 8 CM THRUSTER NEUTRALIZER CATHODE TIP TEMPERATURES

In contrast to results obtained with the main cathode, the data of Figure 2 reveal that increases in neutralizer keeper current effect corresponding increases in orifice plate temperatures. This apparently occurs because the keeper current is a larger fraction of the total emission current in the case of the neutralizer cathode than it is in the case of the main cathode. Figure 2 is also striking because of the very low temperatures at which the neutralizer orifice plate operates in its normal, zero heater power, operating condition (400-500°C).

Conclusion

The orifice plates of the main and neutralizer cathodes operate at low temperatures under design conditions. These temperatures (400°-600°C) are probably too low to cause barium to migrate by evaporation and condensation inside the cathode. It is important to note that the insert temperatures in these cathodes could however be substantially greater than the orifice plate temperatures that have been measured. In order to determine the magnitudes of temperature differences between the orifice plate and the insert, tests were performed on a mock up of the 8 cm thruster cathodes. These tests involved the use of a quartz body through which insert temperatures could be measured optically. The work is described in the next section of this report.

HOLLOW CATHODE STUDIES

Dan Siegfried

A critical component of the 8 cm thruster hollow cathode is the cathode insert. Its design affects cathode lifetime and performance of mercury hollow cathodes. Most of the concerns about hollow cathodes revolve around the effect of insert design on the insert operating temperatures. These temperatures in turn affect both the performance of the cathode and the depletion rate of the low work function material that it contains. In addition, the recent change to a sintered tungsten insert in the CIV cathode led to a need for increased testing to explain differences in operating keeper voltages from those that had been observed with the foil inserts.

In order to investigate these effects, insert temperature profiles and insert emission currents were determined for a number of different insert configurations using a special test cathode. The effect of a number of operating parameters on keeper voltage for a cathode operating with a sintered tungsten insert were also investigated. The results of these investigations will be presented and their applicability to the CIV cathodes used in the 8 cm thruster will be discussed.

Apparatus and Procedure

In order to isolate the insert from the orifice plate electrically and to provide for direct visual observation of the insert, a special cathode was constructed using a quartz body tube in the manner suggested by Figure 3. The cathode consisted of a quartz tube (4.4 mm O.D. X 2.2 mm I.D.) with a conventional thoriated tungsten orifice plate having a 0.25 mm diameter orifice. The end of the quartz tube and the back of the orifice plate were both ground flat. The plate was held tight against the tube by a tensioning device which also acted as the keeper electrode. This electrode was separated from the orifice plate by a 2.3 mm thick spacer as shown in Figure 3. The quartz tube was covered on the outside by a cylindrical, tantalum foil radiation shield which had a narrow ($\sim$1.5 mm) longitudinal slit in it. The shield was spot welded to the perimeter of the orifice plate and was wrapped with a wire heater which was in turn covered by another slotted tantalum foil radiation shield as shown in Fig. 3. The slot in the radiation shield allowed direct visual observation of the insert and internal discharge through the quartz tube. The cathode assembly was mounted in the support structure shown in Fig. 4.

The insert was attached as shown in Fig. 4 such that it was electrically isolated from the rest of the structure by a quartz insulating tube. The insert could be moved axially during cathode operation. Three different types of inserts were used in these tests, namely: a single layer, rolled tantalum foil insert; a multiple layer, rolled tantalum foil insert and a sintered tungsten insert. Initial testing was performed using a single layer, rolled tantalum foil insert made of 0.025 mm thick foil (3.75 mm dia x 15 mm long). This testing was

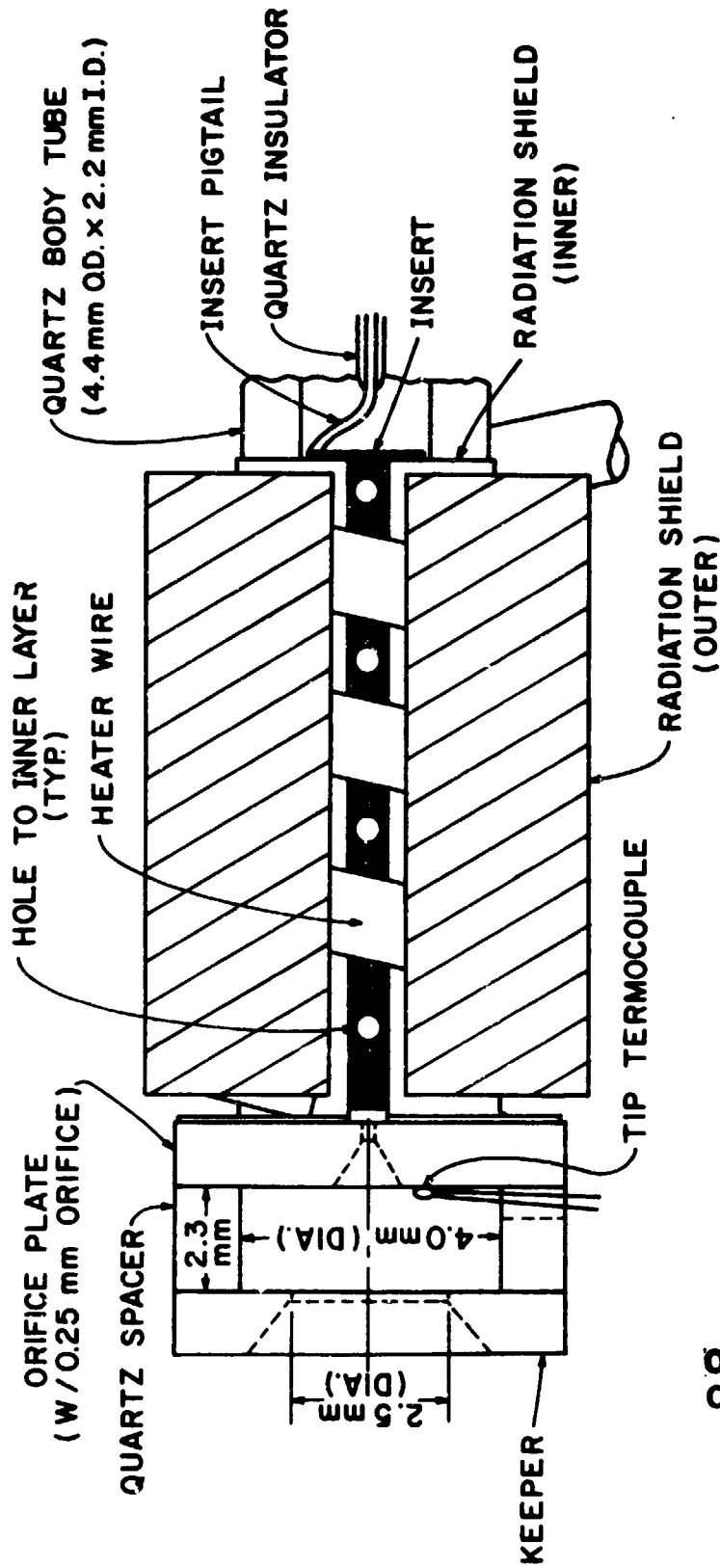

ORIGINAL PAGE IS
OF POOR QUALITY

FIGURE 3. QUARTZ BODY CATHODE SCHEMATIC

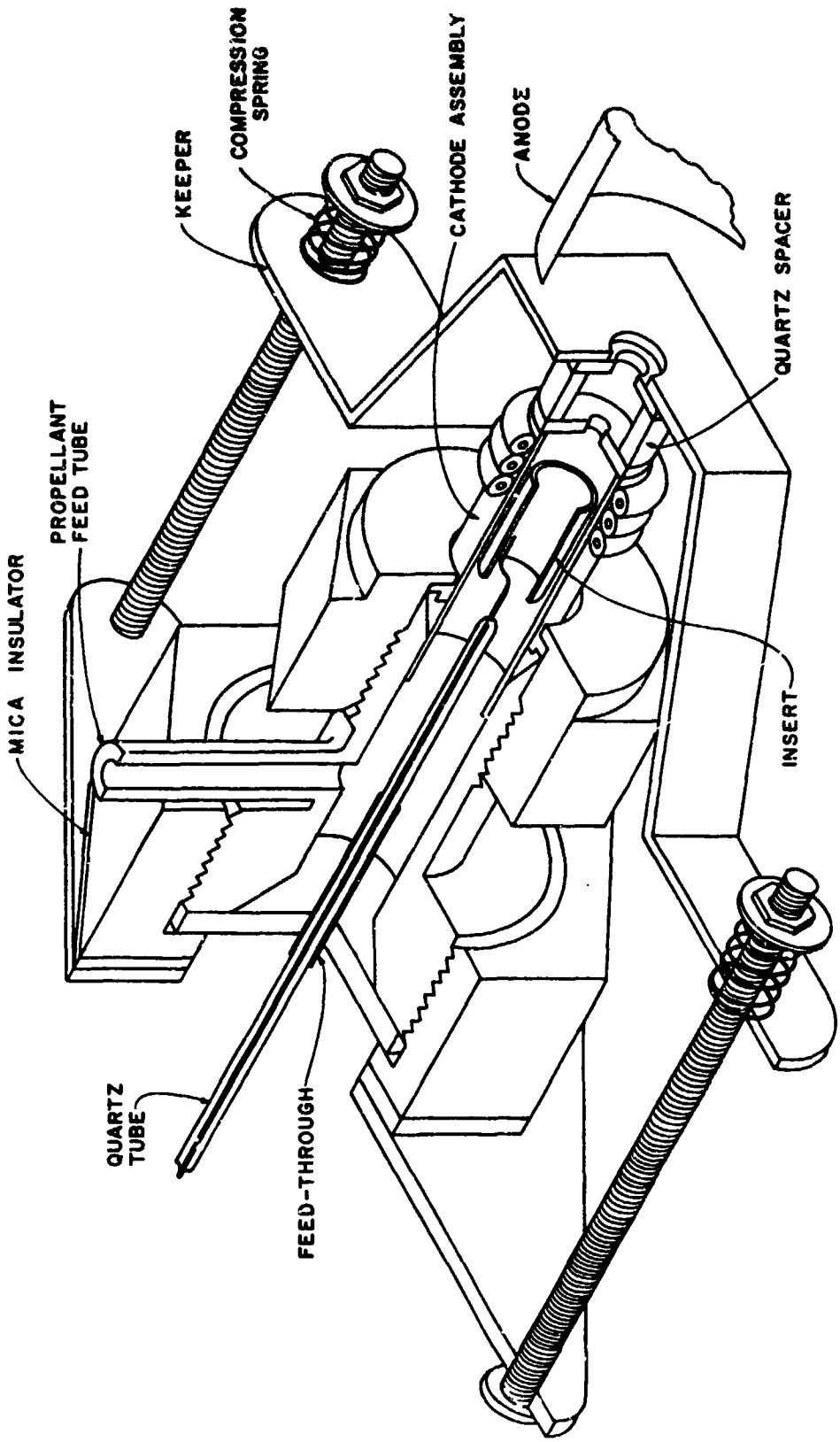

FIGURE 4. MECHANICAL ASSEMBLY OF QUARTZ BODY CATHODE

actually begun using a larger cathode body (6.3 mm O.D. X 4.3 mm I.D.) than the one described above, a 0.76 mm diameter orifice and the open keeper configuration shown in Figure 5. Further, radiation shields were not installed on this quartz body tube. This configuration was used to get a qualitative feel for the insert temperature distribution and it provided initial measurements of insert emission current. Color slides and motion pictures of this cathode were made under various operating conditions. These conditions included spot and plume modes of operation both with the insert coated with chemical R-500* emissive mix and with the insert nearly devoid of R-500. This cathode was operated at a flow rate of ∿150 mA. A similar single layer insert (0.025 mm thk. foil X 1.9 mm dia X 11 mm long) was operated in the smaller (2.2 mm I.D.) cathode of Fig. 3 but without the enclosed keeper. Temperature measurements were made on the outside surface of this insert at five points along the insert for discharge currents of 0.5 and 1.0 A and heater powers of 0 and 14 watts. Measurements were made at a flow rate of ∿100 mA.

The second type of insert tested, a multiple layer rolled tantalum foil one, was similar to the one originally used on the 8 cm thruster. The insert was ∿1.9 mm in diameter by 11.8 mm long and had 7-8 layers of 0.0125 mm tantalum foil. Four small holes extended through all but the innermost layer of foil. By aligning the holes with the viewing slot as shown in Fig. 3, the temperature of the innermost layer of the insert could be determined using the micro-optical pyrometer. This cathode was operated at a flow rate of ∿ 90 ma. Temperature measurements were made for discharge currents of 0, 0.3, 0.5, and 0.7 A at heater powers of 0 and 21.7 watts.

---

* J. T. Baker Chemical Company, Phillipsburg, New Jersey.

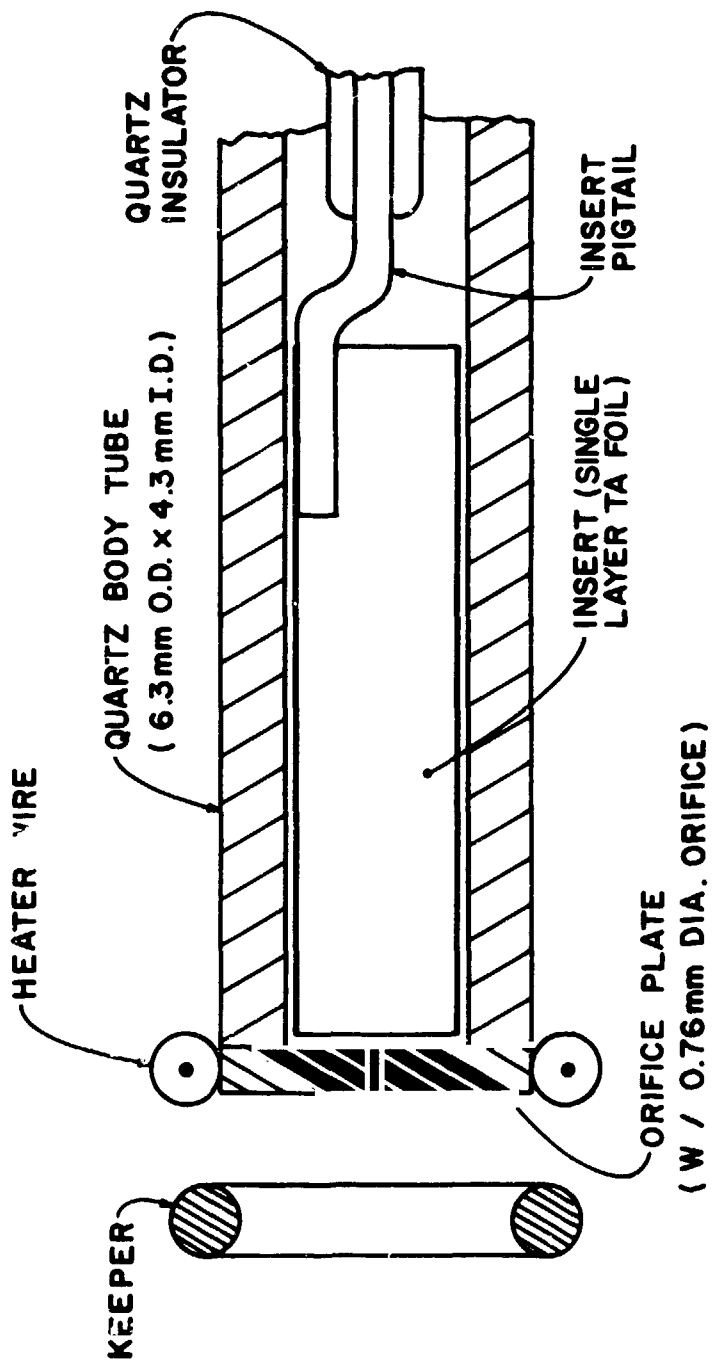

FIGURE 5. CATHODE CONFIGURATION FOR FILM SEQUENCE

The third type of insert tested was a sintered tungsten insert impregnated with barium aluminate (Semicon type S-84). This insert is identical to those that will be used in the 8 cm thruster with the exception of the four holes (0.71 mm dia.) drilled through one side wall to facilitate testing. Using the micro-optical pyrometer, temperature measurements were made along the outside surface of this insert, the inside surface of the insert opposite each of the holes drilled through the insert and on the exposed edge of the inner radiation shield slot. Temperature measurements were made at discharge currents of 0, 0.3, 0.5, and 0.7 A for the cases of 0, 20.8, and 40.8 watts of heater power. The cathode was operated at a flow rate of $\sim$ 90 ma. The effect of various operating parameters on keeper voltage was also investigated for the sintered tungsten insert operating at the heater powers and flow rate noted above. During these tests the insert-orifice place separation, the discharge current and keeper current were all varied.

In all of the above tests, insert surface temperatures were measured using a micro-optical pyrometer. This method of temperature measurement is influenced by both the emissivity of the radiating surface and the transmissivity of the quartz tube and glass bell jar. These effects were accounted for by calibrating the pyrometer against a platinum/platinum-rhodium thermocouple. The calibration was carried out for samples of both tantalum foil and the sintered tungsten insert material. In each case the material sample was spot welded to a section of swaged heater wire and the thermocouple was attached to the surface of the sample. This sample/heater assembly was then inserted into a quartz tube the same size as the cathode body and the whole apparatus was placed in the bell jar. The surface temperature of the sample was then measured at

various heater powers using both the thermocouple and the micro-optical pyrometer. All of the results contained in this report were corrected based on the calibration curves resulting from these tests.

The orifice plate temperatures in all of the tests were measured using a platinum/platinum-rhodium thermocouple spot welded to the downstream surface of the cathode orifice plate. Since the insert and the orifice plate were electrically isolated from each other and from the rest of the cathode structure in all of these tests, it was possible to measure the emission current for each of these components. Insert and orifice plate emission current data were recorded for all of the tests cited above.

The cathode was operated with a keeper current of 0.2 A for most of this testing. Exceptions to the 0.2 A keeper current will be noted in the text which follows.

Results

Emission Current Distribution

In the cathodes tested, when operating under normal conditions, the emission current contribution from the insert ranged from 80 to 90% of the total emission current (anode plus keeper current). The orifice plate current only amounted to a small fraction of the total emission current (0 to 5%). The remainder of the current can presumably be accounted for as ion current to internal cathode surfaces and to other surfaces at ground potential in the facility. The relative fractions of the current from the insert, orifice plate and structure obtained for a given operating condition were found to be constant and very repeatable. In general, the percentage of the emission current from

both the orifice plate and the insert increased slightly as discharge current or heater power was increased.

The importance of the insert in the emission process was also demonstrated by disconnecting the insert from the power supply during cathode operation. This immediately extinguished the discharge. However, disconnecting the orifice plate from the circuit showed little effect on the discharge outside of a slight (less than one volt) increase in discharge voltage. When the orifice plate was disconnected, it was found to float at 3 or 4 volts above ground potential. The fact that the orifice plate can be floated with respect to ground without significantly affecting cathode operation is considered important. By operating with the floating orifice plate one would expect to reduce orifice erosion because operation in such a condition would result in a marked decrease of the impact energy of the impinging ions.

Under certain circumstances, it was found that most of the emission current could be drawn from the orifice plate. This was first observed after applying a small drop of R-500 directly to the upstream side of the orifice plate and then installing a new rolled foil insert which did not contain any R-500. This cathode was difficult to start but when it did start it ran for a very short time in a manner similar to that described above with most of the current going to the insert. During this period the insert glowed very red over its entire length. However, after a few minutes all of the current shifted to the orifice plate, and the insert stopped glowing and could be moved away from the orifice plate or disconnected without affecting cathode operation. The shift of the emission site was probably due to either the depletion of the small amount of R-500 which had migrated to the insert during warm up or to

the activiation of the fresh R-500 on the orifice plate as a result of high temperatures achieved during the first few minutes of operation. The latter is considered more likely. After operating in this mode for a few minutes, the current gradually shifted back to the insert, stabilizing at approximately the insert-to-orifice plate current ratio found for normal operation. This appeared to be the preferred operating mode as the discharge remained in this configuration for the remainder of the test. Similar operation with most of the current going to the orifice plate was observed at other times in the testing but was always associated with startup after installation of a new insert or addition of R-500 to the orifice plate. In all cases, after a few minutes of operation, the emission would shift to the insert in what is considered to be the normal condition of operation.

Another type of quartz cathode was also tested. This is shown in Fig. 6. This cathode did not have a metal orifice plate but had an orifice formed by heating the quartz until the end shrunk inward to give the desired orifice size. The channel formed in this manner had the shape illustrated in Fig. 6 with a minimum diameter of 0.76 mm.

This all-quartz cathode started easily. During the initial operating period it ran in a stable manner at conditions indistinguishable from the cathode with the metal orifice plate which it replaced. During this initial period, the cathode was operated over a wide range of conditions and was started and stopped a number of times. Both plume and spot modes of operation were observed. The cathode operated easily at discharge currents in the range of 5 to 10 A, although operation at discharge currents above 5 A was limited to brief periods (10 sec. or less) for fear of damaging the orifice. At high currents the quartz orifice tended to

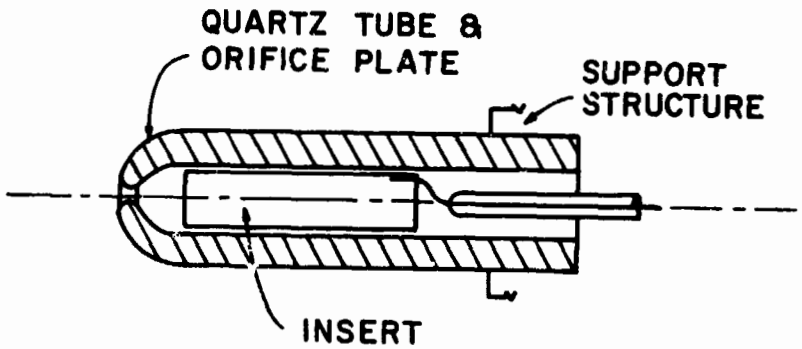

FIGURE 6. ONE-PIECE QUARTZ TUBE CATHODE

enlarge reaching a maximum of ∿1.0 mm after which the size remained approximately constant. During subsequent operation it was found that this cathode was difficult to start, that it required rather high flow rates (150-250 mA) to operate, and that it operated at fairly high discharge voltages (22-28 v.). Although a specific cause for this change in operating conditions was never positively identified, the evidence suggested that the abnormal operation was due to mercury vapor leakage from the point between the quartz tube and the mounting structure.

These experiments indicate that the hollow cathode will operate in a normal manner with electron emission from the insert alone. In fact, though the orifice and orifice plate may enter into the emission process to some extent, the insert appears to be the preferred emission site. The combined ion flux to the insert and electron emission from the insert accounts for more than 80% of the discharge current. The successful operation of the cathode with the quartz orifice indicates that the main functions of the orifice appear to be as a flow restriction to maintain a high neutral density inside the cathode and as a current path to the downstream discharge.

Insert Temperatures

The initial operation of the quartz tube cathode using the larger (4.3 mm I.D.) quartz tube with a 3.75 mm dia single layer, foil insert (Fig. 5) provided a number of interesting qualitative results worth describing. Since the insert was a single layer of 0.025 mm foil, the relative emission activity of a particular area inside the insert could be estimated on the basis of the local temperature of the foil as indicated by its color. When this cathode was operated at low currents with

sufficient R-500 present, the insert had a glowing orange band located near its midpoint. As the current was increased this glowing region extended downstream along the insert until the entire downstream portion of the insert was glowing uniformly. When the discharge changed to the spot mode, the hottest region shifted to the downstream edge of the insert which radiated intensely. The temperature was observed to decrease monotonically toward the upstream end of the insert. When the cathode was operated with an insert that was nearly depleted of R-500, the hot spot associated with the emission region would migrate randomly along the surface of the insert. This migration was most rapid at low currents immediately after the cathode had been operated at rather high currents ($\sim$5 A) and was apparently related to the discharge seeking the most advantageous surface conditions for emission. In all cases, when the discharge shifted to the spot mode, the hottest region immediately shifted to the downstream edge of the insert. The randomly migrating emission spot observed in these tests, again stresses the importance of surface work function on the emission process. The localized heating which was observed with the tantalum foil inserts adds support to earlier contentions that the predominant cathode mechanism is thermionic emission enhanced substantially by the high fields which exist because of the extremely dense, highly conductive plasma that is present.[4]

The phenomena described above were filmed using Ektachrome Super 8 motion picture film and Ektachrome High Speed 35 mm slide film. The film was edited to a three minute sequence showing the effects of mode transition and the moving insert spot associated with depletion of R-500. A 16 mm copy of the motion picture and accompanying description are available for viewing upon request.

Insert temperature profiles are shown in Figs. 7 through 13 for the 2.2 mm I.D. (Fig. 3) cathode using the three different types of inserts: namely, the single layer, rolled tantalum foil; the multiple layer, rolled tantalum foil; and the sintered tungsten inserts. All of the figures show the insert temperature as a function of axial position along the insert measured from the orifice plate. In addition, the orifice plate temperatures are indicated on an adjoining axis to the left of the figure and operating conditions are shown in tabular form using the following symbols: I_D (discharge current), I_K (keeper current), I_I (insert current), I_o (orifice plate current), V_D (discharge voltage), and V_K (keeper voltage).

Figures 7 and 8 are for the single layer tantalum foil insert operating at heater powers of 0 and 14 watts respectively. Figures 9 and 10 show the temperatures of the inner layer of foil for the multiple layer tantalum foil insert operating at heater powers of 0 and 21.7 watts respectively. For the sintered tungsten insert an attempt was made to measure temperatures on the inside of the insert by sighting through the holes drilled through the insert along one side. It was found that the presence of the plasma radiation made these internal surface measurements unreliable. However, based on the conductivity of the insert material and on observations made by viewing the insert as the discharge was turned off, it was estimated that the temperature difference between the inner and outer surfaces of the insert was less than 25°C. Figures 11, 12, and 13, therefore, show the temperatures measured on the outer surface of the sintered tungsten insert operating at heater powers of 0, 20.8, and 40.8 watts respectively.

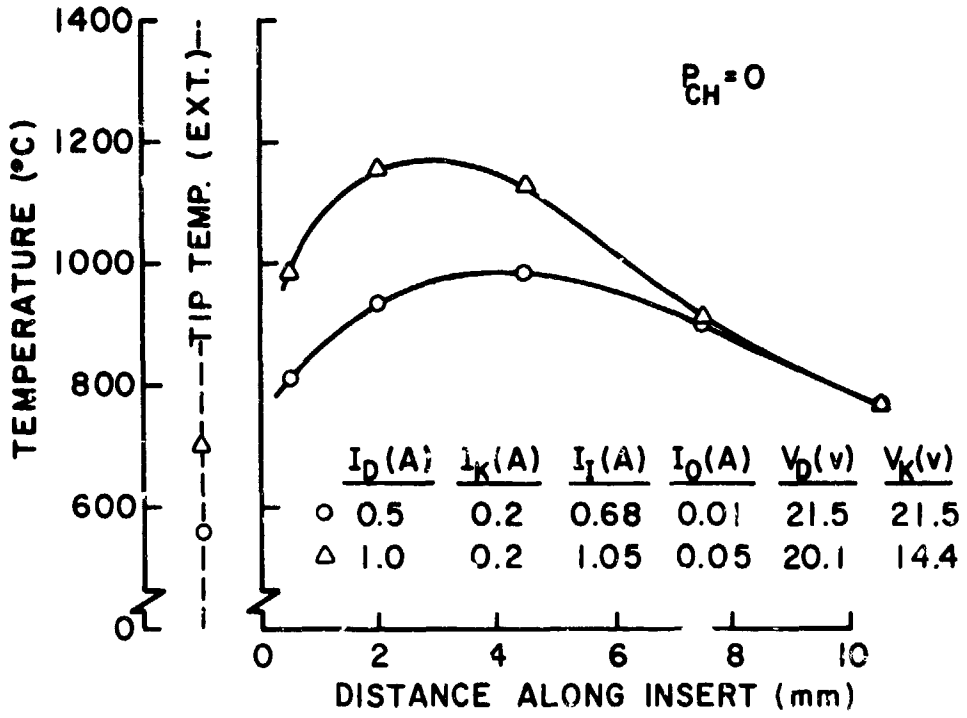

FIGURE 7. SINGLE LAYER FOIL INSERT TEMPERATURE PROFILE (ZERO HEATER POWER)

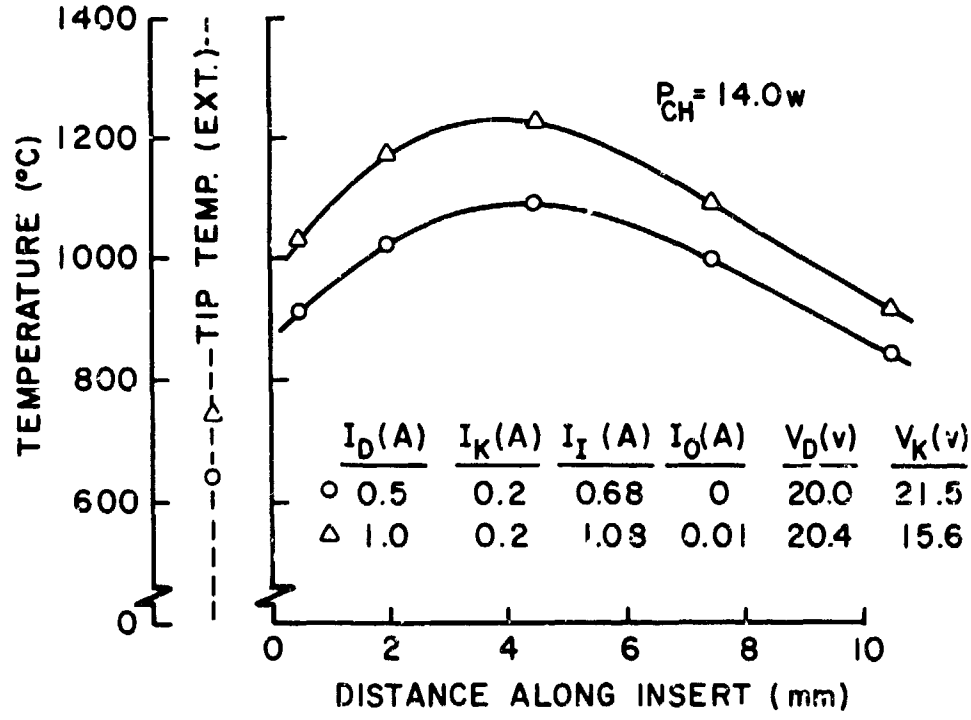

FIGURE 8. SINGLE LAYER FOIL INSERT TEMPERATURE PROFILE (14 WATT HEATER POWER)

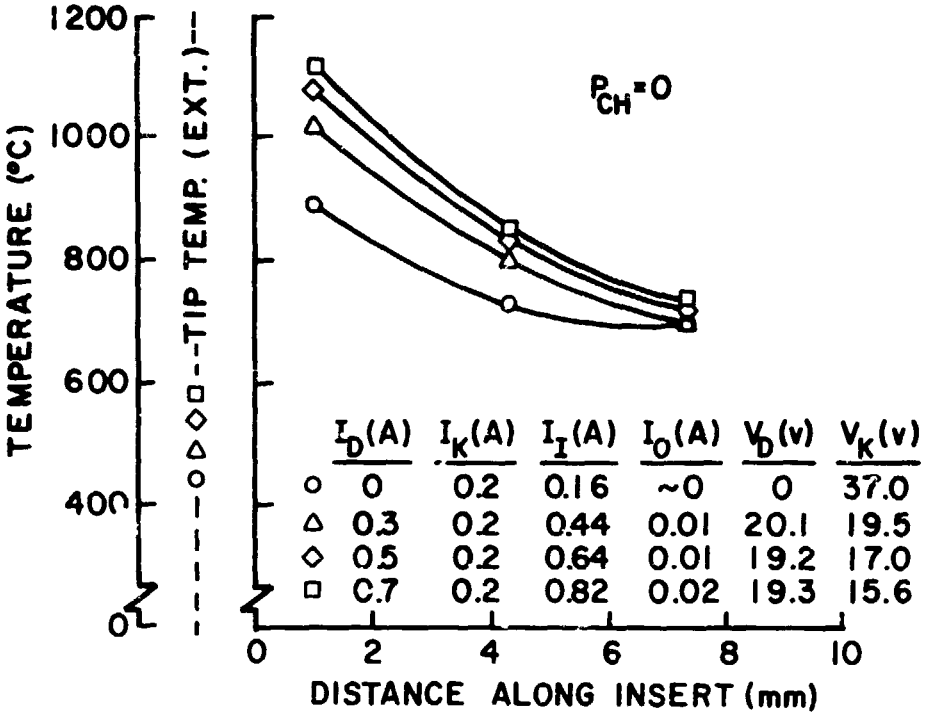

FIGURE 9. MULTIPLE LAYER FOIL INSERT TEMPERATURE PROFILE (ZERO HEATER POWER)

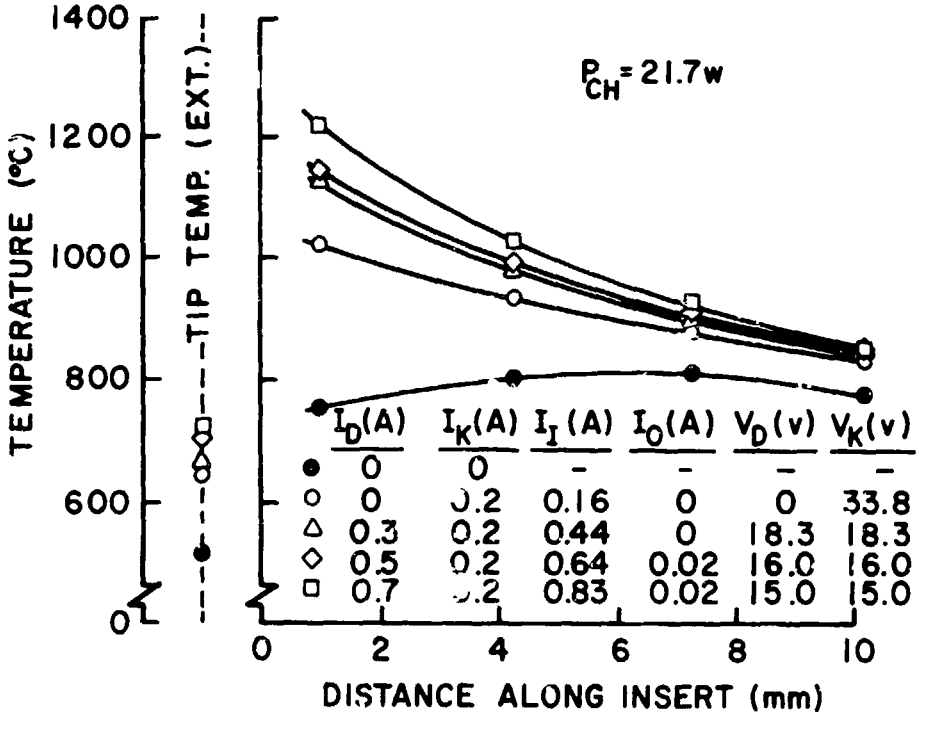

FIGURE 10. MULTIPLE LAYER FOIL INSERT TEMPERATURE PROFILE (21.7 WATT HEATER POWER)

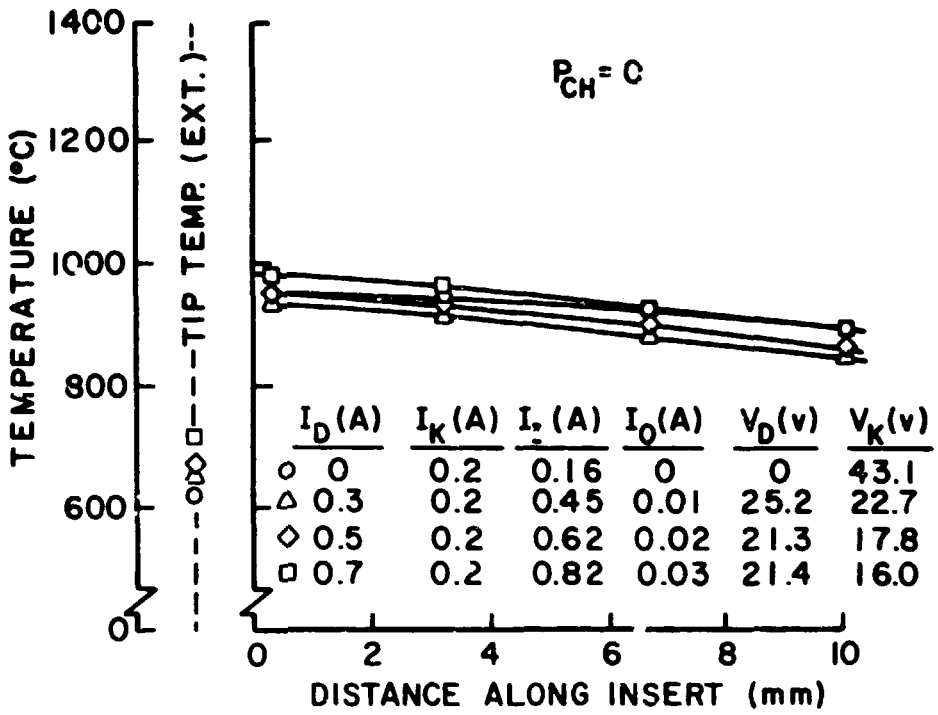

FIGURE 11. SINTERED TUNGSTEN INSERT TEMPERATURE PROFILE (ZERO HEATER POWER)

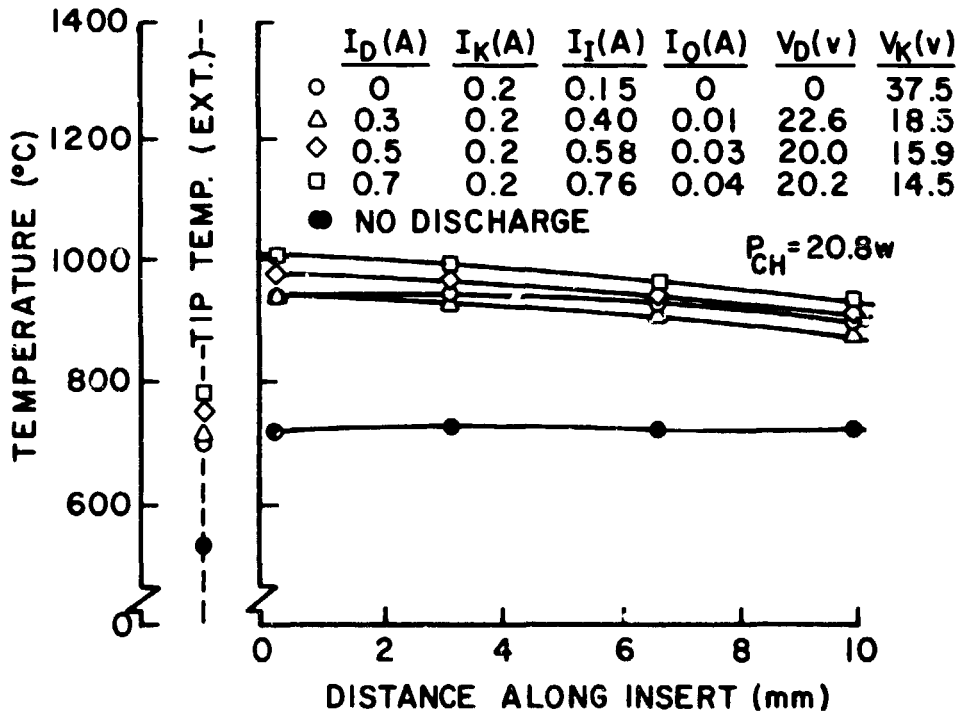

FIGURE 12. SINTERED TUNGSTEN INSERT TEMPERATURE PROFILE (20.8 WATT HEATER POWER)

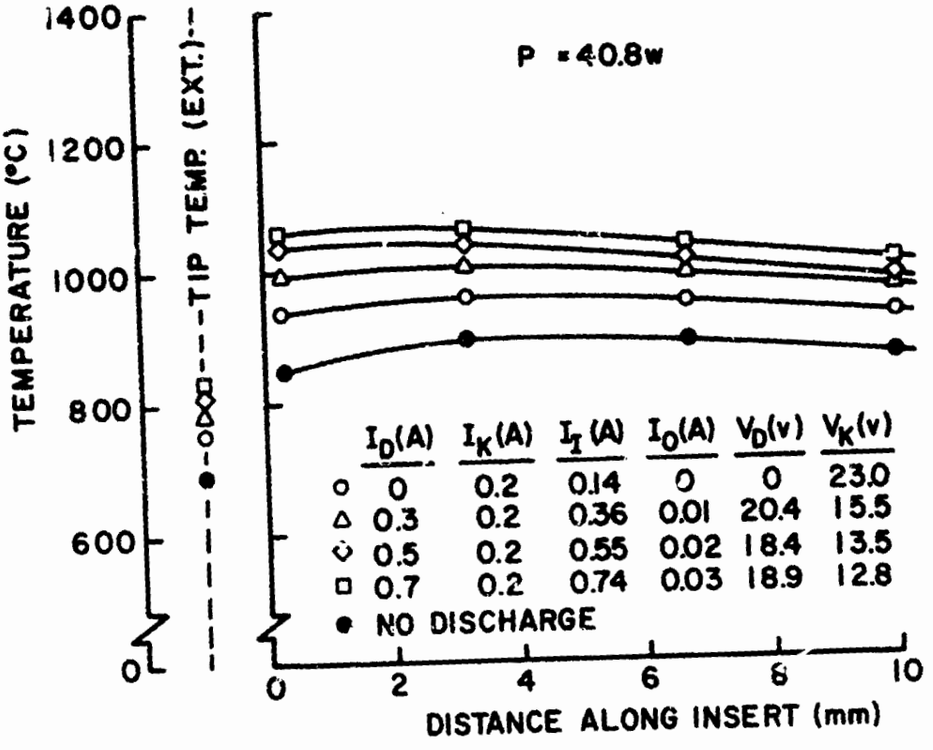

FIGURE 13. SINTERED TUNGSTEN INSERT TEMPERATURE PROFILE (40.8 WATTS HEATER POWER)

There are significant differences in the temperature profiles for the three types of inserts. The single layer foil insert shows the highest temperature at a point 3 or 4 mm upstream of the end of the insert. This is different than either the multiple layer foil insert or the sintered tungsten insert both of which had a maximum temperature at or near the downstream end of the insert. This observation of the single foil insert is also in conflict with qualitative visual observations of the single layer foil insert in the 4.3 mm I.D. cathode which suggested the maximum temperature existed at the downstream end of the insert except in the plume mode. The majority of the data suggests that under normal operating conditions the maximum insert temperature occurs on the downstream end of the insert. This agrees with earlier results[4] based on Langmuir probe data that showed the maximum plasma potential and plasma densities to also occur adjacent to the downstream end of the insert. Since heating of the emission site results presumably from energy transferred to the insert by ions impacting the surface after falling through the potential drop associated with the local sheath, the high plasma density on the downstream end of the insert would be expected to cause the maximum temperature to occur at that position also. The case where the maximum insert temperature was upstream of the end of the insert was found only with the single layer, foil insert and was probably due to this hot area having the lowest surface work function. This could be because this was the region where R-500 was initially applied or because evaporation or migration took place in such a way that these regions developed the lowest work function. On the other hand, the multiple layer, foil insert replenishes R-500 only from the ends where it can evaporate from between the foil layers and would

presumably have a considerably lower work function on each end, so the emission would be expected to be greatest on the upstream end. The sintered tungsten insert has a larger thermal mass and better thermal conductivity than the two foil inserts. It would therefore be expected to exhibit less severe temperature gradients and to have the low work function material evolve fairly uniformly from all surfaces. These observations agree at least qualitatively with the temperature profiles for the three types of inserts.

The single layer tantalum foil insert was investigated mainly because of the ease of taking temperature measurements at any point along its surface and because it lent itself to qualitative investigation of effects such as the moving spot associated with a lack of R-500. This insert has no apparent practical application, so the rest of the discussion will center around the results of the multiple layer, rolled tantalum foil insert and sintered tungsten insert.

A comparison of the multiple layer, rolled foil and sintered inserts can begin with a discussion of the obvious differences between the shapes of the profiles. Figures 9 and 10 show that the multiple layer rolled tantalum foil insert sustains much steeper axial temperature gradients than does the sintered tungsten insert (Figs. 11, 12, 13). The maximum insert temperature for both types of insert is found at or near the downstream end of the insert. However, the increase in temperature, effected by an increase in discharge current, is greater with the rolled foil insert than it is with the sintered insert. This is made particularly obvious in Figs. 14 and 15 which show the maximum insert temperature plotted against the discharge current for a number of heater powers for the rolled foil and sintered inserts respectively. The data in Figs. 14

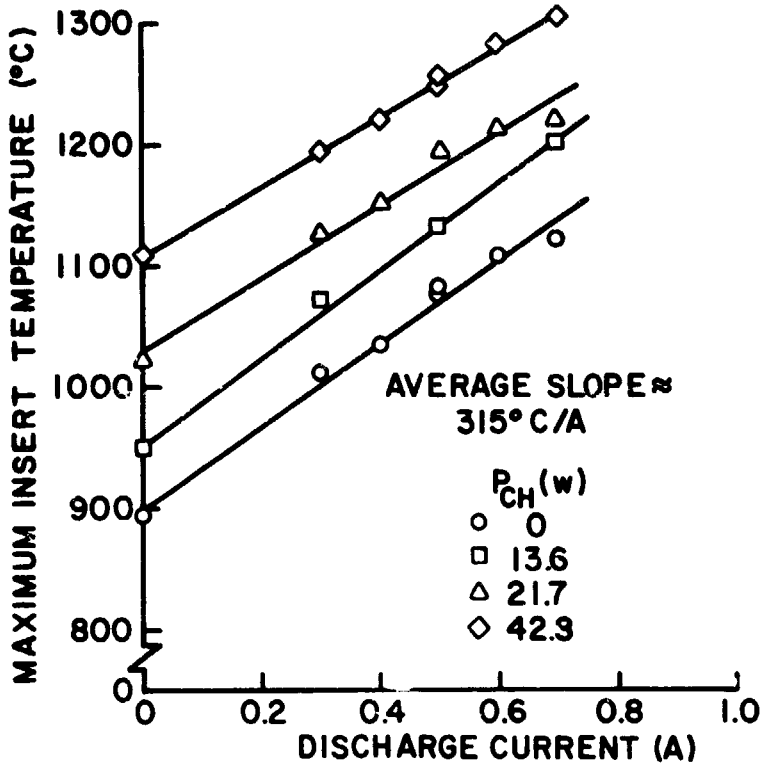

FIGURE 14. MAXIMUM MULTIPLE LAYER FOIL INSERT TEMPERATURE VS. DISCHARGE CURRENT

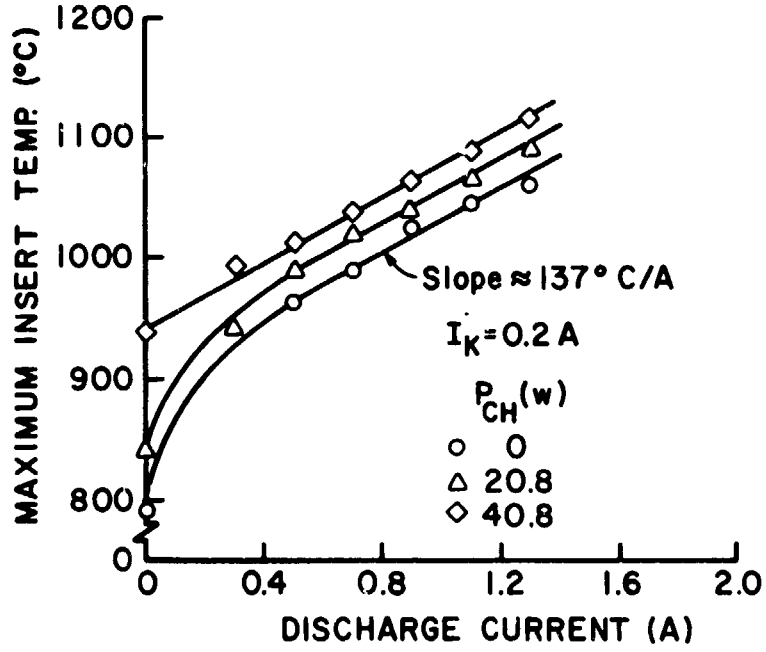

FIGURE 15. MAXIMUM SINTERED TUNGSTEN INSERT TEMPERATURE VS. DISCHARGE CURRENT

and 15 for the different heater powers can be fit reasonably well by straight lines and these lines are approximately parallel for each insert. This indicates that the effect of discharge current on the maximum insert temperature is essentially independent of the heater power. This change in temperature with discharge current is much greater for the rolled foil insert than with the sintered insert. The rolled foil insert sees a change in the maximum insert temperature of ∿315°C for each ampere change in discharge current (Fig. 14), while the data in Fig. 15 for the sintered insert shows a slope of only ∿13/°C/A. Both the steeper axial temperature gradient and the greater sensitivity to discharge current seen with the rolled foil insert can be explained qualitatively by its lower effective thermal conductivity. Most of the energy input to both inserts apparently occurs on the inner surface at their downstream end where most of the emission activity is also presumably taking place and where the plasma densities are the highest. The thermal conductance for the rolled foil insert is relatively low in either the axial or the radial direction when compared to corresponding conductances for the sintered tungsten insert. In the axial direction the energy conducted away from the downstream end of the rolled foil insert is small because the foil is so thin (0.0125 mm). In the radial direction the energy conduction is also small because of the poor thermal contact between the layers of the insert. The two major modes of energy removal from inserts are therefore radiant exchange between the outer surface of the insert and the cathode body (in this case the inner radiation shield of Fig. 3) and conduction through the pigtail on the upstream end of the insert. Because the sintered insert conducts energy more readily in both the radial and axial directions, the observation that

it is not as strongly influenced by increases in discharge current as is the rolled foil insert, is reasonable. On the other hand, the energy input to the tip of the rolled foil insert is not readily conducted away in the axial direction and is effectively shielded from dissipation in the radial direction by its outer layers which act effectively as radiation shields.

Keeper Voltages for Sintered Tungsten Inserts

The recent change to the sintered tungsten type of insert for use in the 8 cm thruster resulted in a somewhat high keeper voltage. A reduction in the keeper voltage was considered desirable, so the effect of changes in a number of parameters on keeper voltage were investigated. Figure 16 shows the keeper voltage as a function of the separation between the orifice plate and the downstream end of the insert for a discharge current I_D = 0.5 A and a keeper current I_K = 0.2 A and for three different heater powers (P_{CH}). The minimum keeper voltage occurs when the insert is near but not touching the orifice plate. The reason for the slight keeper voltage decrease of $\sim$ 0.5 v with the insert in this position may be associated with the additional surface area of the insert that is uncovered as the insert is moved out of contact with the orifice plate. The Debye length is estimated to be extremely small ($\sim 3 \times 10^{-5}$ cm) in this region so that a small retraction of the insert could conceivably expose the end surface of the insert to the plasma making that region available for emission. The maximum insert temperatures showed a very slight ($\sim$5°C) decrease as the insert was moved to the position where the keeper voltage was a minimum. Further upstream motion of the insert did not affect the insert temperature substantially

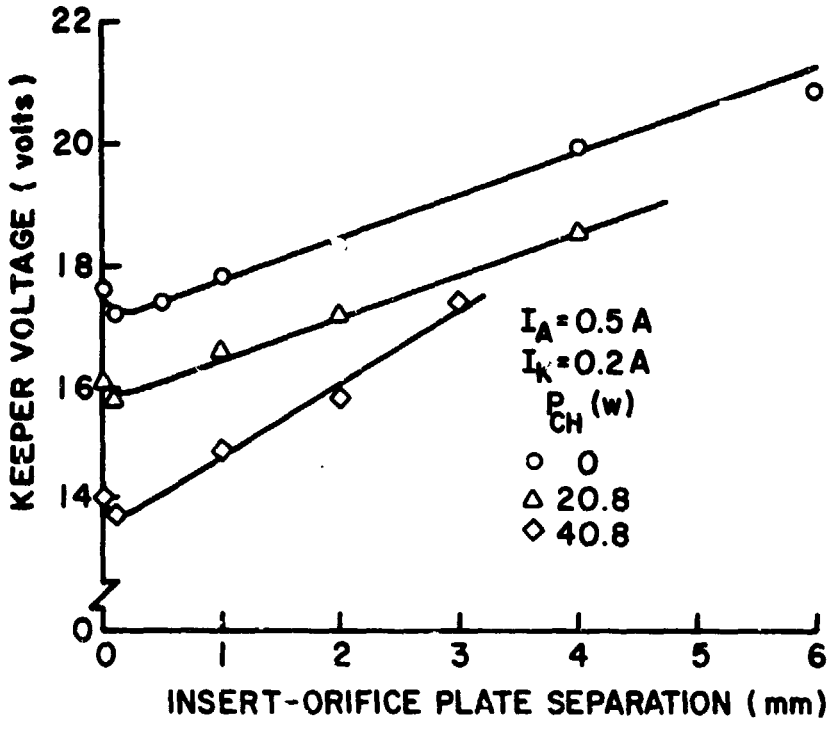

FIGURE 16. KEEPER VOLTAGE VS. SINTERED TUNGSTEN INSERT-ORIFICE PLATE SEPARATION

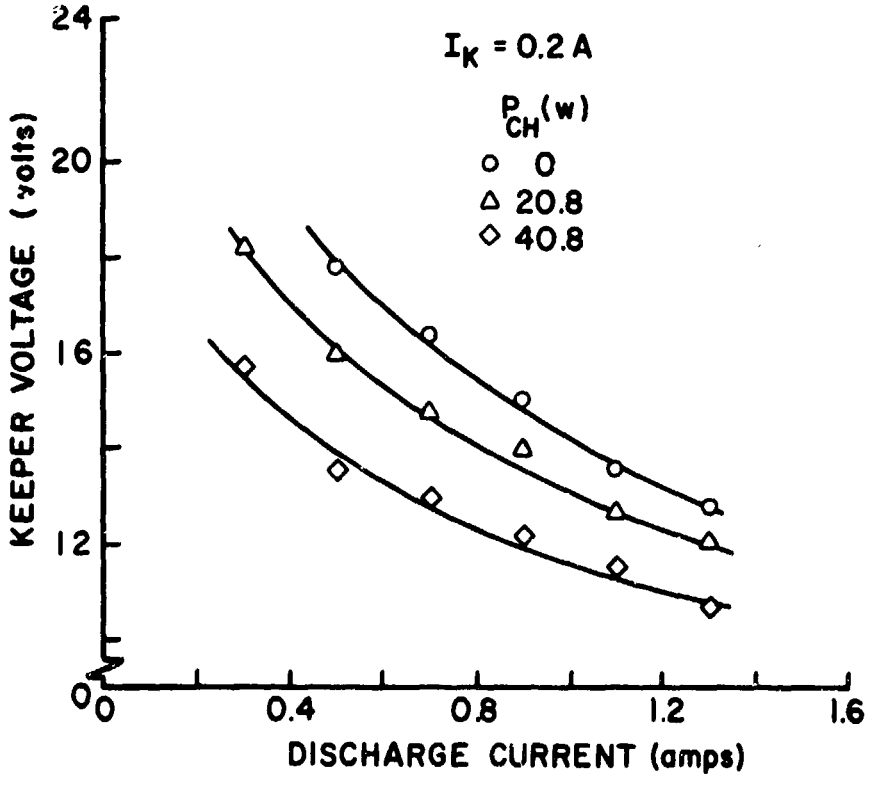

FIGURE 17. KEEPER VOLTAGE VS. DISCHARGE CURRENT (SINTERED TUNGSTEN INSERT)

until the insert was a few millimeters upstream. At this point the insert temperatures began to climb. It was also interesting to note that the orifice plate temperature dropped by about 45°C as the insert was pulled away from the orifice place and the keeper voltage dropped to its minimum. It is believed that this temperature drop occurred as a result of reduced heat transfer from the insert to the orifice plate.

Figure 17 illustrates the effect of discharge current on keeper voltage at a constant keeper current of 0.2 A for three heater powers. The keeper voltage is observed to decrease substantially as the discharge current is increased.

Figure 18 shows the keeper voltage as a function of keeper current at a discharge current of 0.5 A for three heater powers. This figure suggests what appears to be an attractive method for reducing keeper voltage. The keeper voltage at the nominal operating conduction (I_D = 0.5 A; I_K = 0.2 A, P_{CH} = 0) is 17.5 v. By running with a heater power of 40 w, it is possible to reduce this by 4 volts to 13.5 v. This would have an additional benefit in raising the maximum insert temperature to ∿1010°C (Fig. 19) where the test cathode data suggest the cathode operates very stably. Coupling this heater power increase with a reduction in keeper current would result in a further reduction in keeper voltage without the loss in keeper discharge stability which ordinarily accompanies a reduction in keeper current. Figure 18 shows that decreasing the keeper current to 0.1 A for a heater power of ∿ 40 w causes an additional one volt decrease in keeper voltage to V_K = ∿ 12.5 v. Figure 19 shows the effect of keeper current on maximum insert temperature for the cathode operating at 0.5 A discharge current. For operation at a keeper current of 0.1 A and with a heater power of ∿ 40 w the maximum insert temperature is ∿ 1000°C.

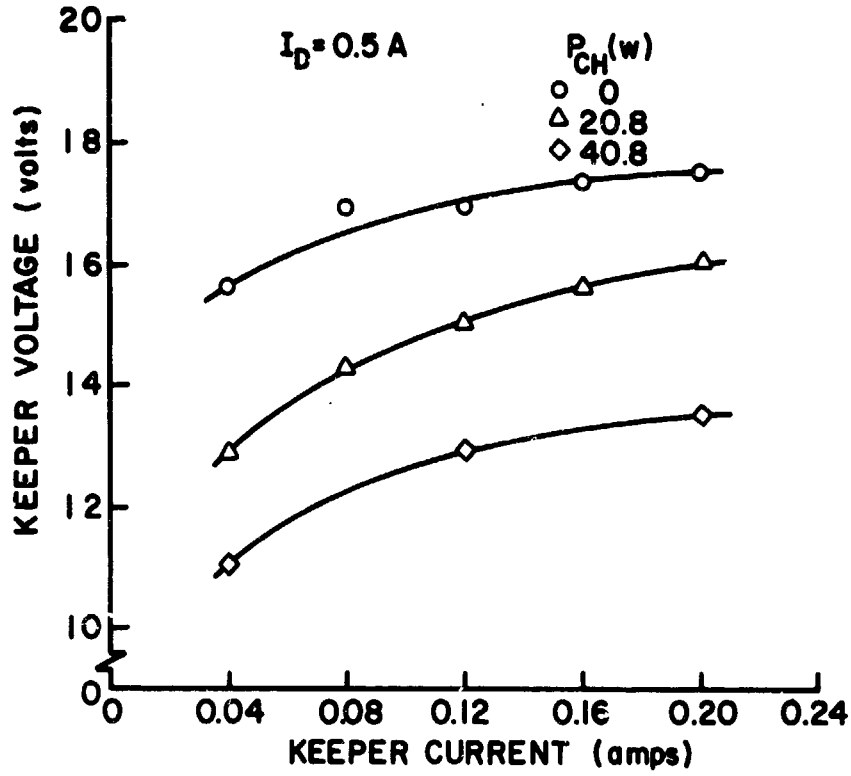

FIGURE 18. KEEPER VOLTAGE VS. KEEPER CURRENT (SINTERED TUNGSTEN INSERT)

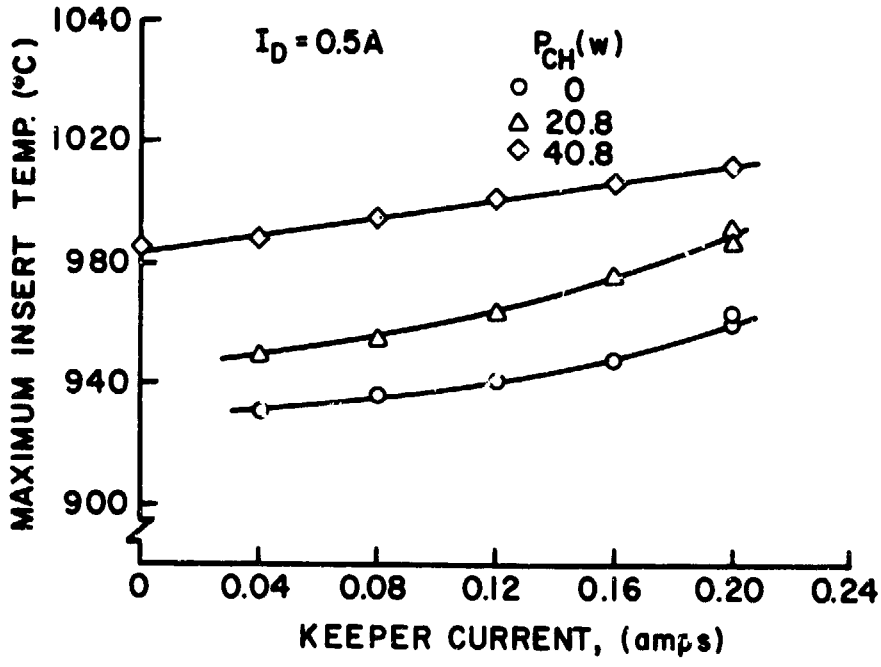

FIGURE 19. MAXIMUM SINTERED TUNGSTEN INSERT TEMPERATURE VS. KEEPER CURRENT

Application of Results to CIV Cathode

The thermal configuration of the cathode-heater assembly used in these tests is quite different from that of an actual CIV cathode assembly. In order to utilize the test results presented here directly, some parameter common to the two cathodes needs to be defined. A reasonable choice for this parameter is the temperature of the surface with which the insert undergoes radiative heat exchange, that is the inner radiation shield in the case of the test cathode and the cathode body tube in the case of the CIV cathode. This is considered a reasonable choice because the major mode of heat exchange between the insert and these surfaces should be radiative. Figure 20 shows the temperature near the downstream edge of the inner shield as a function of electrical heater power for the case where there is no discharge in the quartz body test cathode. This figure can be used to provide a tie between an actual CIV cathode and the test cathode in the following way. First, the cathode tip temperature would be measured in a CIV cathode at the heater power being considered but with no discharge. This temperature should be about equal to the corresponding cathode body temperature for the CIV cathode. It would then be used to enter Figure 20 to determine the heater power required in the test cathode to produce this same temperature at the inner radiation shield. Once the test cathode heater power is known, it can be used along with discharge and keeper currents to enter Figures 11 to 13 and 19 to determine the insert temperature profile that should prevail in the actual CIV cathode under corresponding conditions. Although this technique is crude, it should provide a reasonable estimate of insert temperatures in other cathodes employing this same insert. As an example of the application of this procedure assume

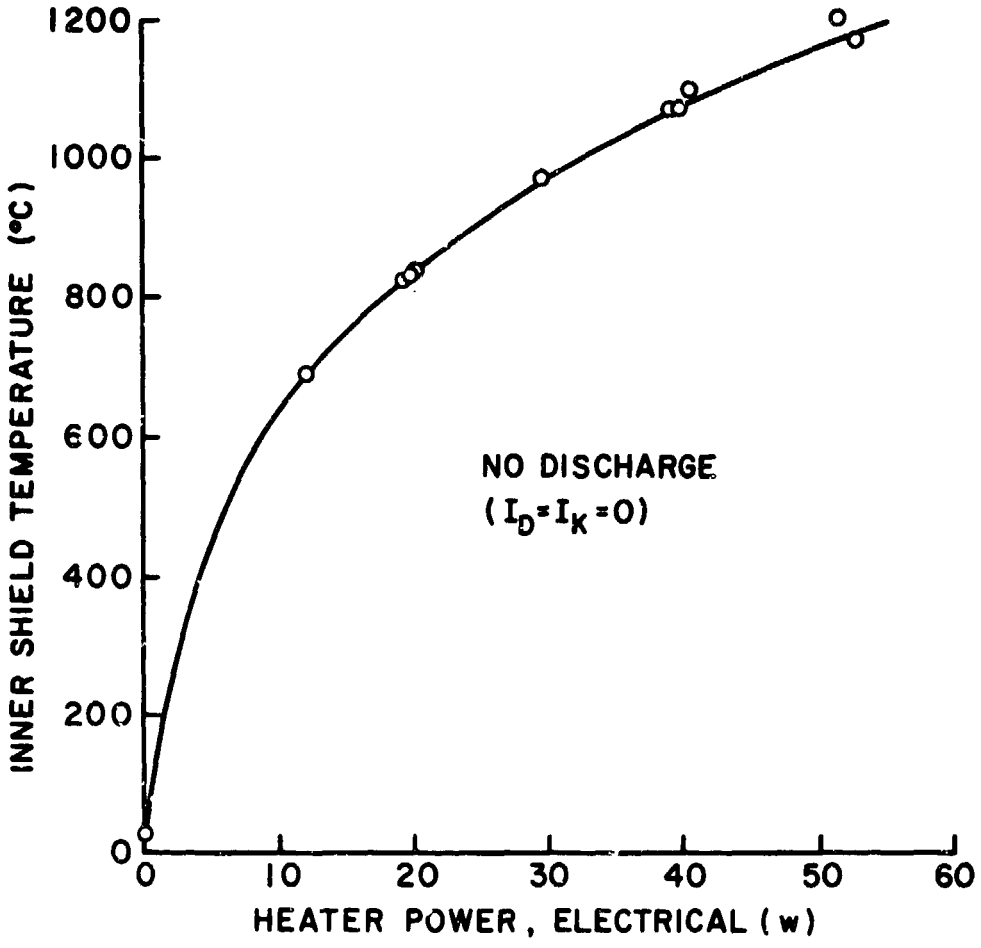

FIGURE 20. INNER SHIELD TEMPERATURE VS. HEATER POWER (QUARTZ BODY TEST CATHODE-SINTERED TUNGSTEN INSERT)

the tip temperature for the CIV cathode without a discharge is 975°C for a heater power of 10 watts. Figure 20 shows that a 975°C shield temperature corresponds to a heater power of ∿ 30 w in the quartz body test cathode. The results for the test cathode shown in the earlier figures can now be entered at a 30 watt heater power to determine insert temperature. For example, using Fig. 19 and interpolating between curves for a heater power of 30 w, one sees the maximum insert temperature in the CIV cathode at a 10 watt heater power should be ∿ 1000°C at a discharge current of 0.5 A and a keeper current of 0.2 A. Although estimating keeper voltage reductions in a CIV cathode from these data is open to considerable question, Fig. 18 does suggest that for these same discharge conditions (I_D = 0.5 A, I_K = 0.2 A) increasing CIV heater power from zero to 10 watts (zero to 30 watts in the test cathode) might reduce keeper voltage by ∿ 2.75 volts.

Effect of Excessive Insert Temperatures

During the course of the sintered insert tests, the cathode was operated at a heater power of 65-70 w. Operation at this high heater power showed that excessive temperatures can cause a rapid but reversible degradation of cathode performance. With the cathode operating at a discharge current of 0.5 A (I_K = 0.2A), the heater power was increased to 65-70 w. Though the cathode temperatures were not being measured at this time, the shield temperature was probably on the order of 1300°C and the insert temperature in excess of 1150°C. After a few minutes at these conditions, the keeper and discharge voltages started to increase substantially. The physical reason for this is not apparent. The heater power was immediately cut back to 20 w but the voltages remained

high (V_D = 25 v; V_K = 20 v). Cathode operation was continued at a heater power of 20 w, and the voltages gradually returned to normal after about 1½ hours. One possible explanation of this phenomenon might be that the high insert temperature somehow resulted in surface depletion of barium causing the high operating voltages. The surface was then reconditioned by migration of material from within the insert after the temperature was reduced back to normal levels. Additional tests which verify this observation and provide some physical explanation are considered desirable.

Conclusions

In the normal operating condition 80 to 90% of the emission current from a hollow cathode comes from the insert. The hollow cathode will operate in a normal manner with electron emission from the insert alone. The main functions of the orifice appear to be as a flow restriction to maintain a high neutral density inside the cathode and as a current path to the downstream discharge.

The maximum insert temperature generally occurs at the downstream end of the insert; and its rate of increase with increasing discharge current is essentially independent of heater power. This rate amounted to $\sim$ 315°C/A for the rolled tantalum foil insert and $\sim$ 137°C/A for the sintered tungsten insert. The local surface work function is apparently important in determining the location of the emission and thereby influences the insert temperature profile. When insufficient low work function material is present the insert can develop local hot spots which migrate randomly across its surface. Excessive cathode heater powers can result in a substantial rise in both discharge and keeper

voltages for sintered tungsten inserts. This effect is at least partially reversible when cathode heater powers are returned to normal levels.

Keeper voltage for the sintered insert could be decreased by increasing the heater power and decreasing the keeper current in a manner that should result in stable discharge condition with lower keeper voltages and reasonable ($\sim$ 1000°C) insert temperatures. Knowledge of the CIV cathode body temperature as a function of heater power when there is no discharge is proposed as a link to the results of a test cathode, which has a different thermal configuration than the CIV cathode.

SCREEN HOLE PL A SHEATH INVESTIGATION

Graeme Aston

The physical characteristics of the plasma sheath that surrounds the screen holes of an ion accelerator system are not well understood. Knowledge of how the screen hole plasma sheath varies in position and shape as a result of plasma density (i.e., beam current) and grid geometry variations is important. These physical characteristics of the screen hole plasma sheath affect directly such things as the divergence of the beam ions ejected from the accelerator system, direct ion impingement upon the accelerator grid with its associated erosion, ion bombardment and erosion of the screen grid, and the magnitude of the ion current which can be extracted from the plasma. Some theoretical and experimental work has been done on determining the physical characteristics of the screen hole sheath.[5,6] However, the available information is sketchy, limited to a couple of idealized cases and of little use in facilitating a general understanding of the sheath phenomena. Therefore, it was felt that a thorough experimental investigation of the screen hole plasma sheath was necessary. This report deals briefly with some of the important aspects of this investigation and presents some of the preliminary results that have been obtained, with comments on possible further work.

Accelerator System Scaling

In order to make accurate measurements of the physical characteristics of the screen hole plasma sheath (i.e., position, shape and structure), it was necessary to use a large accelerator system so adequate spatial resolution could be achieved and so the probe would not perturb the plasma significantly. This was done by increasing the screen hole diameter from a value of 2.06 mm, which is typical of ion thruster accelerator systems, to a diameter of 12.7 mm. The other geometrical parameters were also scaled directly by the ratio of these two diameters so geometric similarity was maintained. It was important to determine whether the maximum normalized perveance per hole and ion beam divergence characteristics of such large apertures were any different from those of the smaller ones typical of most ion thrusters.

Figure 21 shows the effect of screen hole diameter on the maximum normalized perveance per hole value for grid sets having similar non-dimensionalized geometric parameters. The symbols used in Figure 21 are total accelerating voltage (V_T), discharge voltage (V_D), net-to-total accelerating voltage ratio (R), grid separation distance (ℓ_g), screen grid hole diameter (d_s), accelerator grid hole diameter (d_a), screen grid thickness (t_s) and accelerator grid thickness (t_a). The non-dimensionalized grid set parameters shown in Fig. 21 are similar to those of the SHAG accelerator system, which is presently used in most ion thrusters. From Fig. 21 it can be seen that there is little effect on the maximum normalized perveance per hole as the screen hole diameter is increased above about 2.0 mm. There is a pronounced effect though when the screen hole diameter is reduced below 2.0 mm. However, this effect in the region below 2.0 mm has been reported previously[7] and

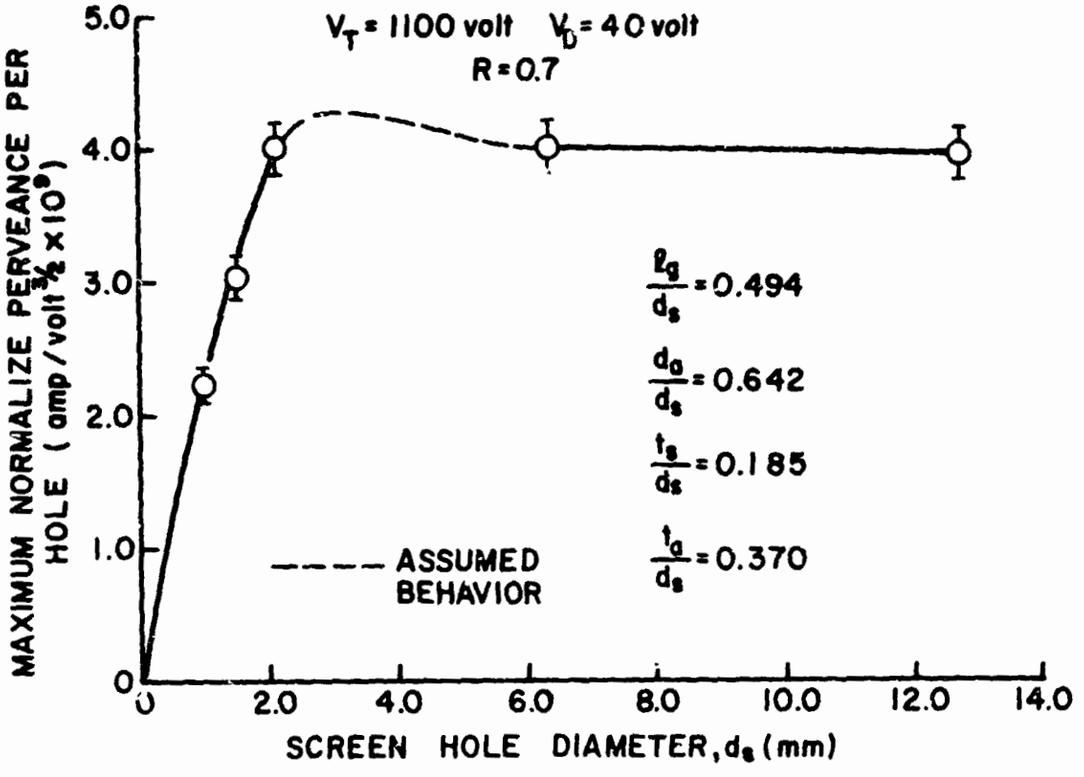

FIGURE 21. THE EFFECT OF SCREEN APERTURE DIAMETER ON MAXIMUM PERVEANCE

presently does not appear to represent a region of interest for ion thruster accelerator systems presently. Ion beam divergence data were also obtained for the larger grid sets shown in Fig. 21 (d_s = 6.35 and 12.7 mm); these divergence characteristics were in close agreement with those already shown to be similar for the three smaller grid sets (d_s = 2.06, 1.5 and 1.00 mm). So in summary, scaling up grid systems from 2 mm dia screen grid apertures to larger sizes does not appear to affect the maximum normalized perveance per hole or ion beam divergence characteristics so long as similar non-dimensionalized grid parameters are maintained. This result greatly extends the range of usefullness for the ion beam divergence data published previously.[7,8]

Sheath Probing Technique

Figure 22 illustrates the basic screen hole sheath probing technique that will be used in studying screen grid sheath movement. Briefly, the probe (Fig. 22a) consists of a tantalum electrode of which all but the end has been encased in quartz tubing. The tantalum probe end, which is exposed to the ion source discharge chamber plasma, is a 0.70 mm diameter ball formed by striking an arc to the wire tip with a heli-arc welder. Figure 22(b) shows the probe positioned within the ion source. The ion source fabricated for this study had a mildly divergent magnetic field and a cylindrical anode 8-cm in diameter. As seen in Fig. 22(b), the probe is connected to the anode through a variable resistor.

The probing technique consists of first aligning the probe at some point of interest on the central hole of the seven hole accelerator system (Fig. 22(c)). The probe is then moved back deep within the discharge plasma and the plasma density is varied until the desired beam

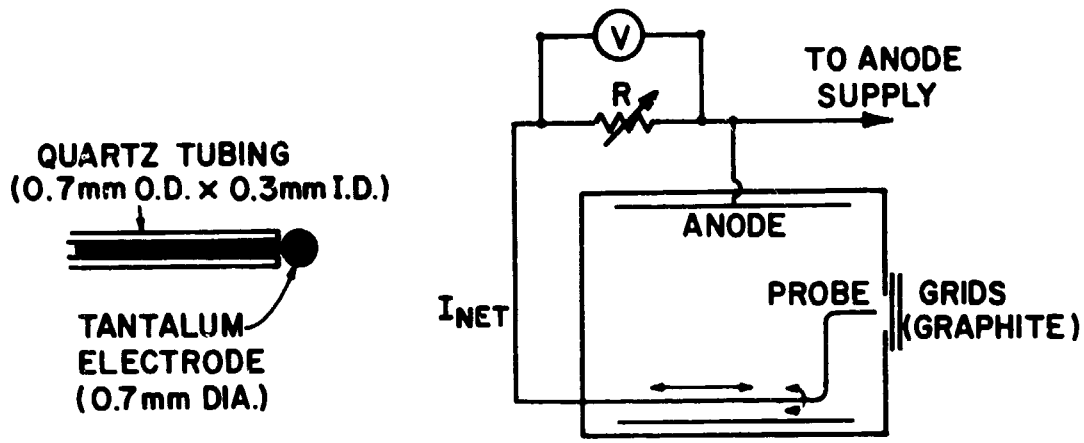

(a) SCREEN HOLE SHEATH PROBE GEOMETRY.

(b) ION SOURCE, SHOWING PROBE LOCATION AND CIRCUITRY.

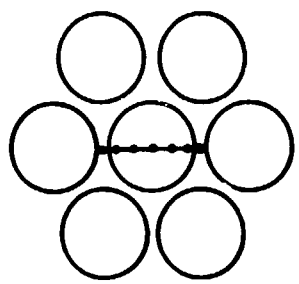

(C) SEVEN HOLE, HEXAGONAL ARRAY, ACCELERATOR SYSTEM SHOWING TYPICAL SCREEN HOLE SHEATH PROBING LOCATIONS ON THE CENTRAL HOLE.

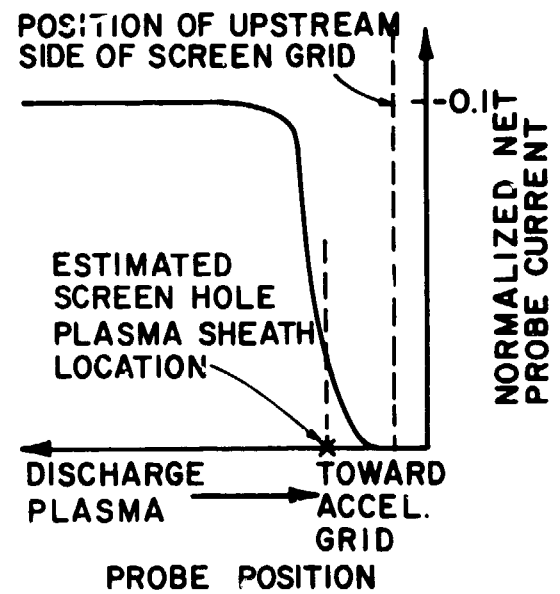

(d) EXPECTED PROBE SIGNAL AS A FUNCTION OF PROBE POSITION.

FIGURE 22. SCREEN GRID PLASMA PROBING STUDY

current (and hence, screen hole sheath position of interest) has been reached. The variable resistor is then adjusted until a potential difference of one volt is detected across it by a high impedance voltmeter. The resistor is then left untouched as the probe is moved into the sheath. Since the sheath represents a region of rapid drop off in electron density, it follows that as the probe enters the sheath region the electron current to the probe will begin to fall off. This will reflect itself as a decrease in the voltage drop across the variable resistor. As a result of moving the probe from deep within the discharge plasma, through the central screen hole sheath and on into the ion acceleration region, one obtains a probe current versus probe position trace similar to the one shown in Fig. 22(d). Since the variable resistor is not altered once a peak signal voltage of one volt has been obtained, reductions in this voltage caused by moving the probe into the sheath are proportional to reductions in electron current reaching the probe. Hence, the designation of normalized net probe current shown in Fig. 22(d). This quantity is negative to reflect the fact that electrons are the dominant current carriers within the plasma. Figure 22(d) permits a determination of the screen hole plasma sheath location to be made. For a first cut, the plasma sheath location was defined as that point where the normalized net probe current had dropped to 10% of its peak value of -1.0 which had been measured with the probe situated deep within the plasma.

Figure 23 shows probe response curves obtained with the probe aligned on the axis of the central screen hole. For these data the following parameters were held constant:

screen hole diameter d_s = 12.7 mm,

grid separation ratio ℓ_g/d_s = 0.390,

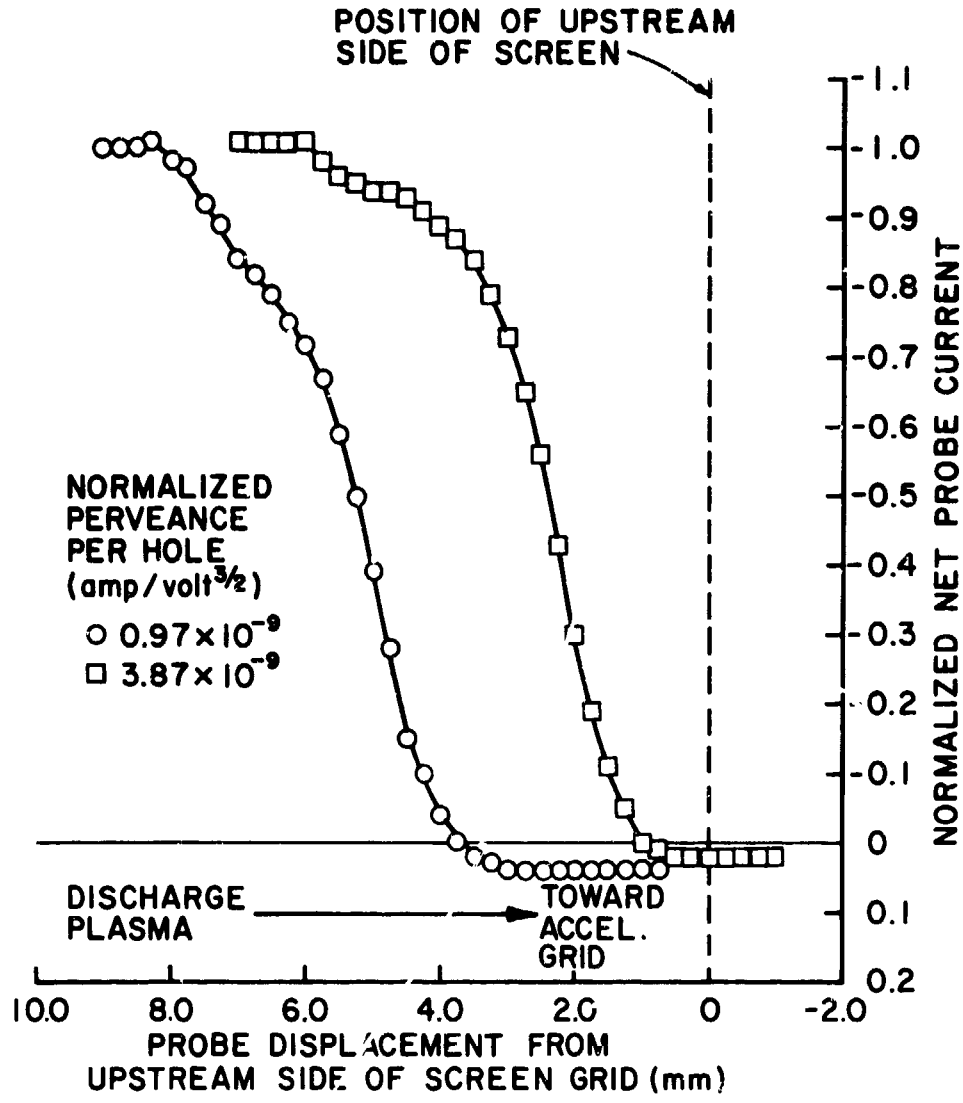

FIGURE 23. TYPICAL SHEATH PROBE TRACES

accelerator hole diameter ratio $d_a/d_s = 0.642$,

screen grid thickness ratio $t_s/d_s = 0.120$,

accelerator grid thickness ratio $t_a/d_s = 0.180$,

total accelerating voltage $V_T = 1100$ volts,

net-to-total accelerating voltage ratio $R = 0.7$,

discharge voltage $V_D = 40$ volt.

The curves in Figure 23 show how with increasing beam current (or normalized perveance per hole) the center of the sheath moves downstream into the screen hole. The maximum normalized perveance per hole obtainable with this grid set was 4.70×10^{-9} amp/volt$^{3/2}$, so the two normalized perveance per hole conditions shown in Fig. 23 correspond to beam current increases from 20% to 80% of the maximum beam current obtainable from the grid set.

Additional probe response curves were obtained at the normalized perveance per hole values examined in Fig. 23. These additional data were taken at probe locations other than the screen hole sheath axis and together with the curves of Fig. 23, and the arbitrary screen hole sheath position definition discussed earlier, it was possible to reconstruct the sheath position and shape. The results of this reconstruction are shown in Fig. 24. The sheath for the smaller beam current is, on the average, 2.5 mm further back from the screen grid than that for the larger beam current. Also, the small beam current sheath has a shape, particularly at its extremities, that one classically assumes will give poor ion focusing; a condition that is known to exist at low beam currents.[7,8] The error bars shown apply to each data point. The size of these error bars is determined by uncertainties in the probe positioning apparatus. It should be noted that when the beam

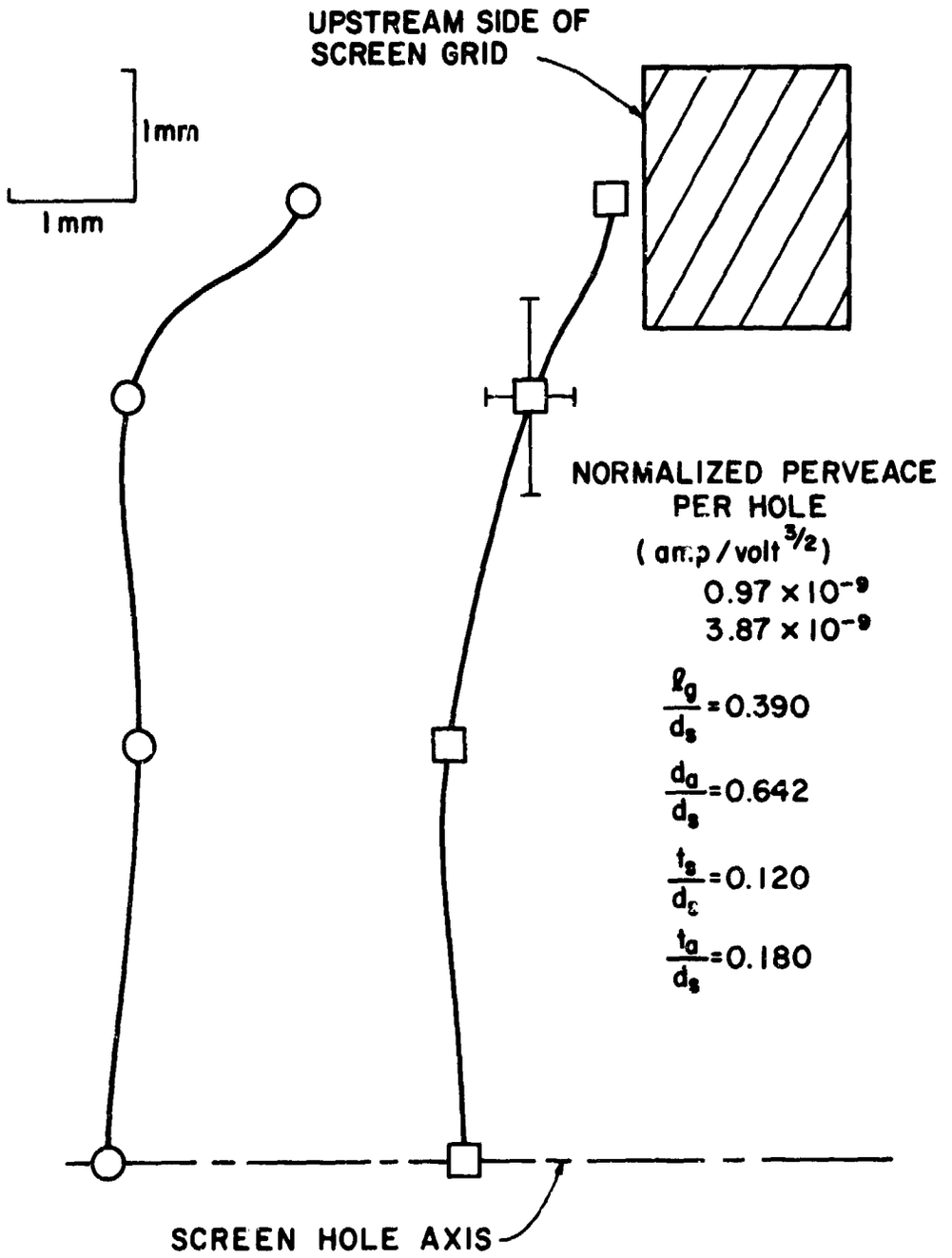

FIGURE 24. SCREEN APERTURE PLASMA SHEATH CONFIGURATIONS

current was increased to very near its maximum, the screen hole sheath was observed to move into the screen hole itself.

Refinements in the Experiment

The sheath probing technique discussed earlier was developed originally to provide an estimate of the sheath position only. However, the probe response curves presented in Fig. 23 indicate a sheath thickness of the order of a few millimeters. It is felt that this thickness is great enough to permit determination of the sheath structure (i.e., the electron and ion number density profiles through the sheath). The present sheath probe design is unsatisfactory for this task because this probe remains biased at near anode potential as it is moved within the sheath. Figure 25 illustrates the shortcoming of holding the probe at a fixed potential as it is moved axially. With the present probe at position XX the surrounding plasma is only slightly perturbed due to its presence because the probe potential is very near anode potential and hence only a few volts below plasma potential. But, when the probe is moved to position YY the potential in the sheath may be ten or twenty volts below the discharge plasma potential. Hence, the probe, because it is biased constantly at near anode potential, could be 15 volts positive of the potential at position YY without the probe present. Thus, with the probe at position YY, electrons which would ordinarily be reflected back into the discharge because of the retarding accelerator grid potential could reach the probe tip. This can occur because the electrons are being attracted by the near-anode potential biased probe. So, in a sense the sheath has been stretched because of the presence of the probe. This error would appear to be a systematic one and so the

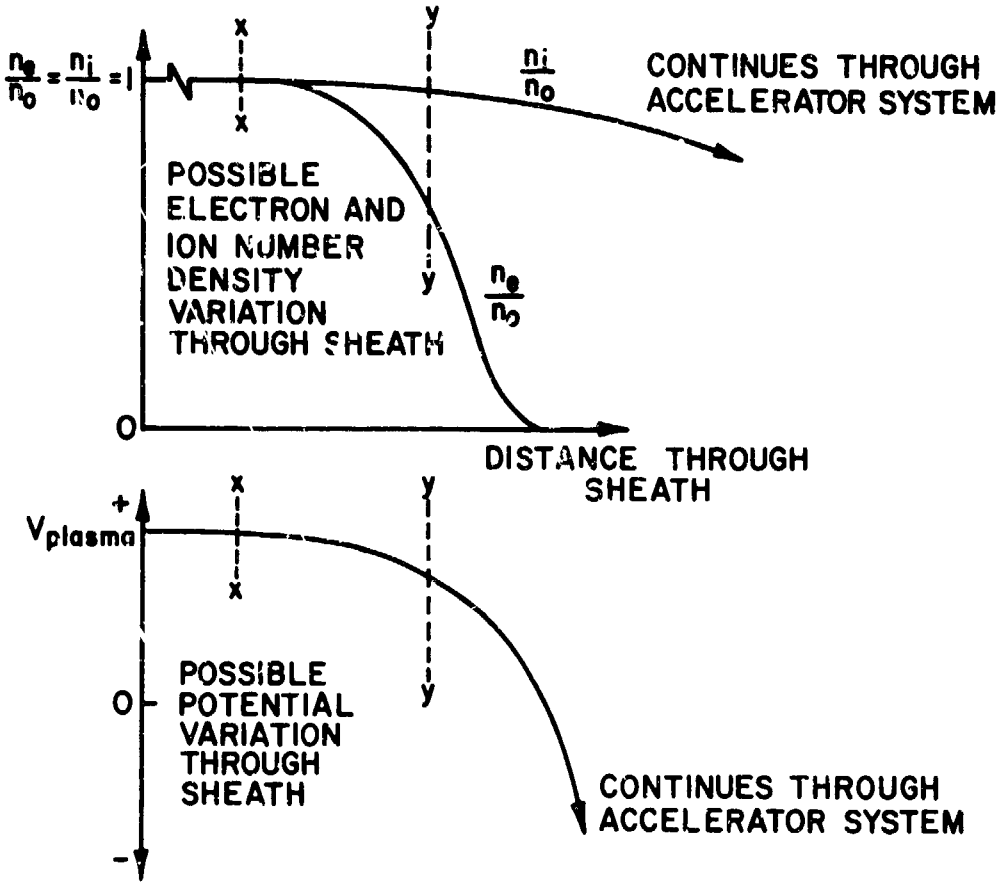

FIGURE 25. QUALITATIVE PLASMA PROPERTY VARIATIONS THROUGH THE SCREEN GRID SHEATH

results presented in Fig's. 23 and 24 are probably still qualitatively correct. The magnitude of this sheath stretching effect is estimated to be small because only the high energy tail of the Maxwellian electrons and the primary electrons would be capable of following the sheath probe for any significant distance and their percentage of the total electron population can be expected to be small.

One could determine the electron and ion number density profiles through the sheath if he could obtain the potential variation through the sheath as a function of distance. What is required then is a probe, positioned at any arbitrary position Y1 within the sheath, that can be used to determine the potential of the equipotential contour passing through that point. The probe can then be biased to plasma potential, the electron current to it can be measured and the local electron and ion densities can be calculated. Usually, plasma potential can be estimated fairly accurately from a Langmuir probe trace. Although conditions within the sheath are not those of a plasma, it is felt that certain plasma potential measurement methods may still apply. The probe designs being considered for this task make use of the emissive hairpin probe technique, scaled to very small sizes. Construction of these nonperturbing probes and the sensing equipment is presently underway.

ADVANCED ACCELERATOR SYSTEM DESIGN

Graeme Aston

It is generally desirable to increase beam current densities substantially above the values of present grid systems and previous ion-optics studies have shown that reducing the screen-to-accelerator grid separation distance increases the beam current density most dramatically.[7,8] Figure 26 shows this effect in the form of a plot of grid separation ratio (ℓ_g/d_s) against maximum perveance per hole for the case where the accelerator hole diameter ratio (d_a/d_s) is 0.642. The correlation of maximum perveance per hole with the natural log of the natural log of the grid separation parameter is empirical rather than physical in basis. Although a number of other parameters were held constant for the data of Figure 26, the correlation is quite useful because previous studies[7] have shown that parameters other than the grid separation ratio and accelerator hole diameter ratio do not affect the maximum perveance significantly, as long as the screen hole diameter d_s is greater than 2 mm. Changes in propellant do change perveances, but this effect can be accounted for by multiplying the argon perveance values of Figure 26 by the square root of the ratio of the atomic weight of argon to the atomic weight of the propellant being used. The accelerator hole diameter ratio (d_a/d_s) for the data of Figure 26 is typical of values used in current grid systems, and the effect of changes in this parameter on maximum perveance can be estimated from previously published ion optics data.[7]

Conventional two-grid accelerator systems are limited in the maximum beam current they can extract from the discharge plasma by the requirement that the grids not touch during operation; this leads to the condition

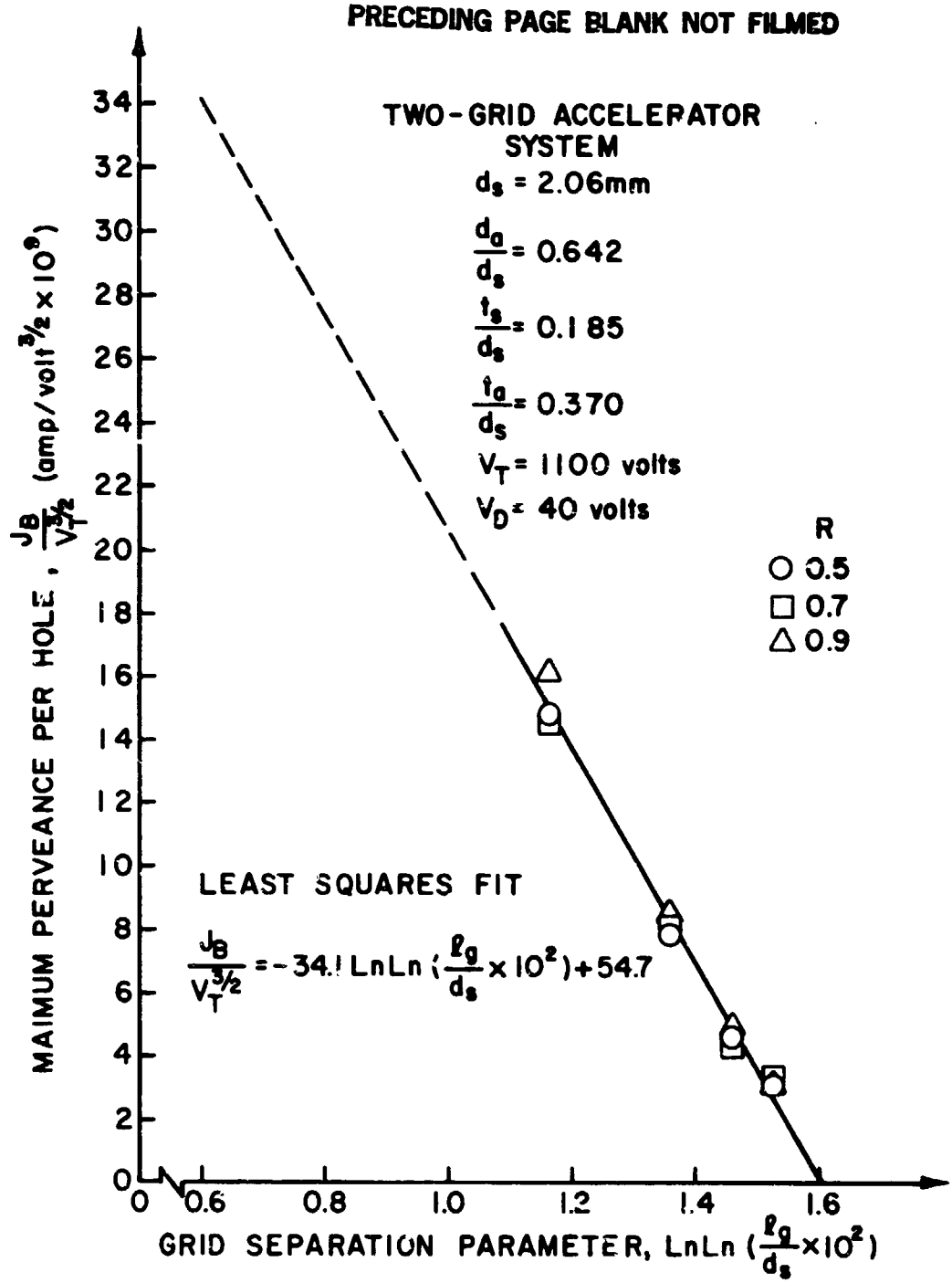

FIGURE 26. EFFECT OF GRID SEPARATION ON MAXIMUM PERVEANCE PER HOLE

of maintaining specified span-to-gap ratios. Figure 26 suggests that the screen and accelerator grids would have to be spaced about 0.2 mm apart to facilitate operation at a beam current density per hole of about 30 mA/cm^2 at V_T = 1100 v. Such a grid spacing would necessitate an accelerator grid system diameter of only a few centimeters to insure reliable operation. Even if such an accelerator system could be built and operated successfully it would still not be optimum because of the finite thicknesses of the screen and accelerator grids. These grids are necessary to maintain the required accelerating potential distribution, but the thicknesses of the grids correspond to regions through which the ions are not being accelerated appreciably. From the point of view of ion acceleration then, one would like to reduce these grid thicknesses to a minimum.

Ceramic Accelerator System

The attainment of high beam current densities without the attendant problems of closely spaced grids has been achieved using glass-coated accelerator grid systems.[9] Although such grid sets are subject to a sputter coating phenomenon which limits their lifetime, there are applications where the lifetimes one attains with them are acceptable. This grid concept was therefore considered worthy of study and a grid set was constructed which incorporated the following features: A ceramic plasma holder, a thin silver/platinum accelerator grid coating fired onto the ceramic plasma holder and a carbon decelerator grid spaced slightly downstream of the plasma holder and silver/platinum coating. Two, seven-hole hexagonal array grid sets were fabricated and tested;

their design features are shown in Fig. 27. The basic design is similar in concept to the composite grids of Banks and Bechtel.[9] However, in this case the plasma holder was made from a machinable glass ceramic (MACOR) obtained from the Corning Glass Works. Because this material is machinable it affords the designer greater flexibility in grid design and more accurate control during fabrication. Figure 28 shows a comparison of the grid leakage current properties of MACOR ceramic, compared with the borosilicate glass used by Banks and Bechtel. At temperatures above about 500°K where grids might be expected to operate the volume resistivity of the MACOR is higher and it exhibits lower leakage currents. Unlike the composite grids of Banks and Behtel, where borosilicate glass was electrodeposited over a conventional molybdenum grid, a silver/platinum coating was fired onto the downstream side of the ceramic plasma holder to serve the function of an accelerator grid. This silver/platinum coating was a precious metal ink (Engelhard #A3147) containing 78% silver and 2% platinum by weight in solution. This ink was painted onto the ceramic plasma holder and fired at 850°C for 10 min. at an average heating and cooling rate of 7°C per minute.

Guidelines developed during three-grid accelerator system tests suggest that the decelerator grid hole diameter should be 25% larger than the accelerator grid hole.[8] Attempts to fabricate a carbon grid which would satisfy this criterion and match the hole spacings of the ceramic grid apertures of Figure 27 were not successful. The decelerator grids of Figure 27, having aperture diameters $\sim$ 15% greater than those of the accelerator grid, were therefore made. These smaller decelerator grid holes resulted in decelerator grid impingement currents that were higher than would be observed with properly designed apertures.

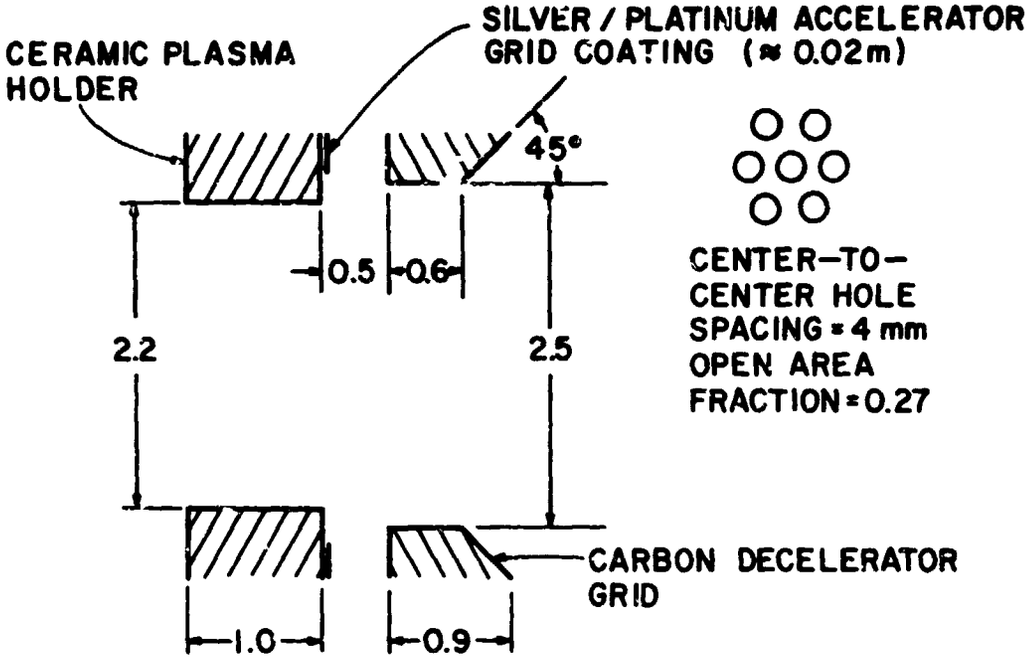

LARGE SEVEN HOLE GRID SET

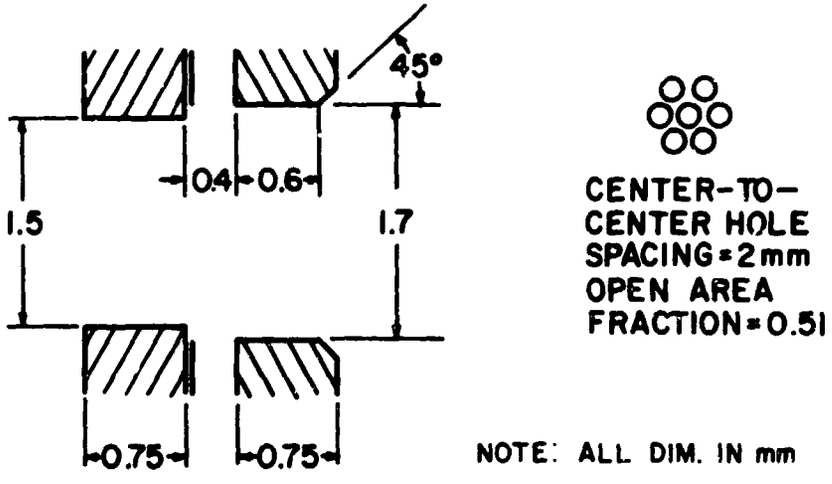

SMALL SEVEN HOLE GRID SET

FIGURE 27. CERAMIC GRID APERTURE CONFIGURATIONS

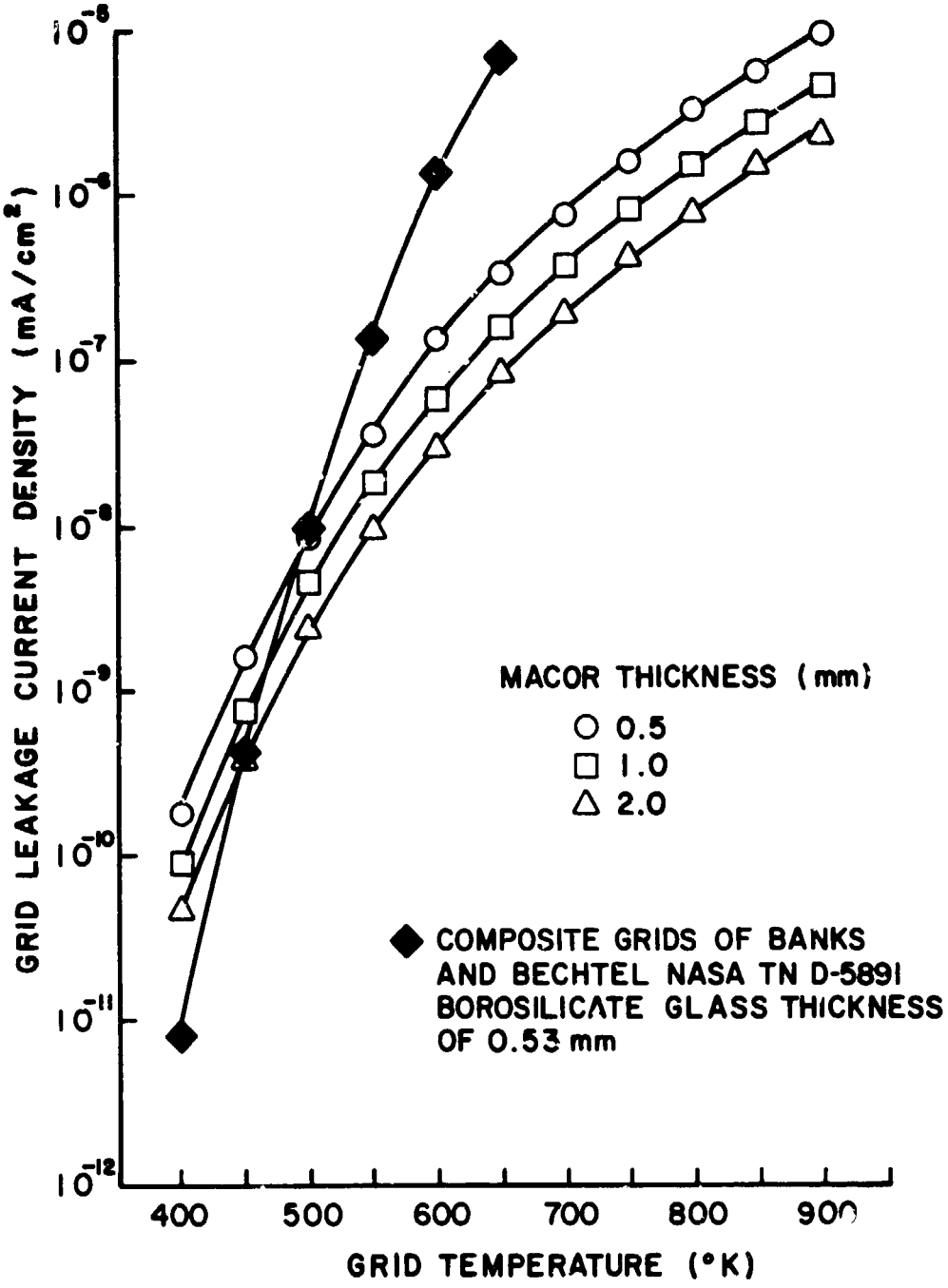

FIGURE 28. GLASS GRID CURRENT LEAKAGE AS A FUNCTION OF TEMPERATURE

It was noted that putting a small 45° chamfer on the downstream side of the decelerator grid holes (Fig. 27) reduced the decelerator grid impingement currents.

Single hole grid sets fabricated prior to the seven-hole designs shown in Fig. 27 indicated that while the ceramic plasma holder could be machined successfully to a thickness of 0.25 mm, such a thin grid was not necessary. The plasma sheath surrounding a thick single hole ceramic plasma holder was probed and found to be well inside the hole. The plasma sheath moved further into the ceramic grid hole as the plasma density was increased. There appeared to be no degradation in beam current density when using a thick rather than a thin plasma holder; though some reduction in discharge losses would be expected with the thin plasma holder.

Table I compares the maximum beam current densities for both the large and small seven-hole ceramic grid sets of Fig. 27 with that of the highest perveance convential two-grid set examined during the previous ion-optics study.[7] These data were obtained by increasing the discharge current thereby increasing the discharge chamber plasma density until some physical limitation was reached. In the case of the conventional two-grid set this limitation was reached when the accelerator grid impingement currents became excessive. For the ceramic grid sets a limitation on available cathode heater and/or arc powers was reached before the accelerator grid impingement limit. Higher current densities than those given in Table I could therefore be expected with the ceramic grids. Average current densities of Column 2 of Table I were calculated by dividing the maximum beam current by the ratio of the accelerator grid open area to the accelerator grid open area fraction.

TABLE I

Maximum Beam Current Densities

V_T = 1100 volts

V_D = 40 volts

R = 0.7

Argon Propellant

ACCELERATOR SYSTEM TYPE	AVERAGE ION CURRENT DENSITY (mA/cm^2)
LARGE 7-HOLE CERAMIC GRID	7.1
SMALL 7-HOLE CERAMIC GRID	15.0
BEST 19-HOLE CONVENTIONAL CARBON 2-GRID SET	9.6

The small 7-hole ceramic grid set is observed to exhibit the highest current density, and it is noteworthy that this value could have been higher if power supply limitations had not been encountered. The large 7-hole ceramic grid set exhibited a lower average current density because the open area fraction of this grid set was substantially less than that of the small 7-hole set. The beam current per unit open area of ceramic grid sets were in fact both about 29 mA/cm^2.

A problem with the ceramic grid set designs of Figure 27 is that the beam divergence angles measured with these designs are large. Divergence half angles of 20° to 25° (for a 95% enclosed current cone) were typical for the small seven-hole ceramic grid set operated at the beam current density of Table I. Another problem was electron backstreaming. The large seven-hole ceramic grid set showed an electron backstreaming level of ≈ 20% of the beam current (the necessary correction was made in the data of Table I so only ion current is shown). The small seven-hole ceramic grid set showed no signs of any electron backstreaming.

No lifetime testing was done, but indications were that backsputtered conducting material coatings would be the dominant failure mechanism of the grids. In applications where long lifetimes were not necessary however such grids should be useful. The concept used to fabricate the grids might also be useful as a quick, low cost method to obtain thin grids for perveance testing.

Conclusion

Large beam current densities can be obtained with the ceramic grid set design outlined in this section. The thickness of the ceramic

plasma holder does not seem to affect the maximum current density which can be drawn from the grids. Probe data suggest this occurs because the sheath is located well within the plasma holder at high current density operating conditions. As plasma holder hole diameter is increased above about 1.5 mm, the accelerator grid thickness must be increased to prevent electron backstreaming. This could be accomplished by coating a ridge around the aperture with the silver/platinum coating used to form the accelerator grid in order to depress the potential on the centerline of the aperture.

DISCHARGE CHAMBER SPUTTERING STUDIES

The lifetimes of discharge chamber components are frequently determined by the erosion rates of those components. This erosion is caused by discharge chamber ions (primarily doubly-charged ones) which strike these surfaces and sputter material away. It has been observed that impurity atoms present in the discharge chamber and on discharge chamber surfaces can effect the erosion rates of these components. Nitrogen for example has been shown to reduce sputtering rates of discharge chamber materials greatly even when it is present at very small partial pressures.[10] It is considered likely that even the mercury propellant may alter the erosion rate of a surface from that which might be expected for the case of doubly-charged mercury ions bombarding a clean surface. Such an effect might be caused by singly-charged mercury ions which hit the surface with insufficient energy to cause sputtering, but enough energy to cause the iors to be imbedded in the base material where they can absorb some of the energy of the incoming doubly-charged ions.

The measurement of sputter erosion rates has become a matter of considerable interest because these rates can determine the lifetimes of thrusters. Sputtering rates can be determined in a discharge chamber environment by actually operating a discharge chamber for a known period of time, measuring the depth of sputter erosion and then calculating the erosion rate. In order to obtain accurate values however very long test times are required. In order to facilitate shorter tests, other less direct methods have been pursued. One of these methods involves installing multilayer erosion test patches. These patches are made by

alternating very thin layers (several hundred angstroms thick) of the material being tested with copper layers of similar thickness. By counting the number of layers of known thicknes that are eroded during a few hours of testing the erosion rate can be determined. A question can however be raised about the validity of such a test, namely; can the ratio of the erosion rate of copper to that for the test material be assumed to be the same as the value determined from measurements on pure copper and pure test metal? If this can be assumed then the test can be used, but if the presence of the copper induces an effect such as coning[11] then the results may not be accurate.

In order to determine the effects of such impurities as copper and nitrogen on the erosion rates of various thruster materials the tests described in the following paragraphs were conducted.

Apparatus

These tests were conduced in a 12 in. dia. bell jar facility pumped by a 4 in. dia. diffusion pumping system. The ion source used was a 15 cm dia. multipole design utilizing anodes and pole pieces on the upstream face of the source only (no sidewall anodes or pole pieces). The source used argon working fluid and the argon pressure was typically $\sim 5 \times 10^{-4}$ torr during operation. Figure 29 shows the ion source with the test specimens arranged in the ion beam for sputter erosion testing. A test specimen consisted of a flat glass substrate onto which a layer of test material had been sputter deposited. This material was then partially covered by a $\sim$ 1 mm thick graphite shield that had been undercut in the manner suggested in Figure 29. As a test specimen was exposed to an ion beam, material was protected where it was covered by the graphite

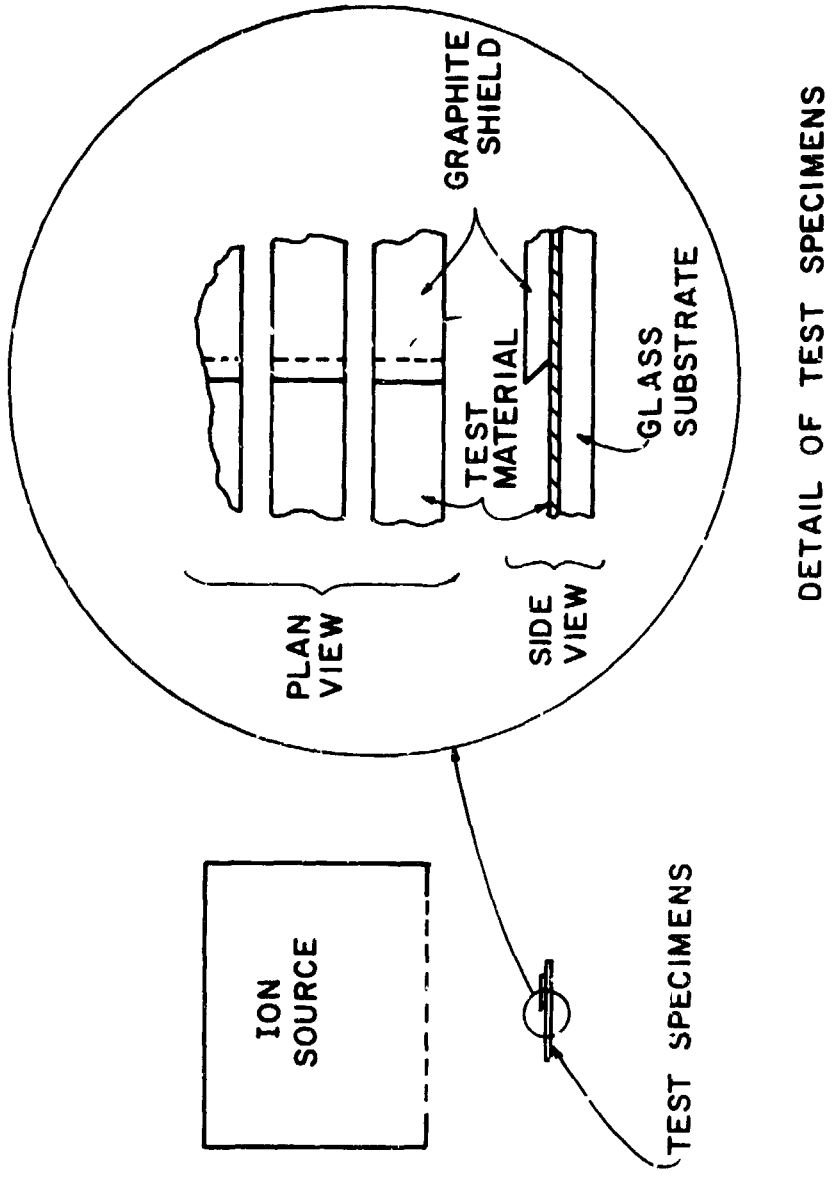

FIGURE 29. SCHEMATIC OF APPARATUS USED TO DETERMINE SPUTTERING RATES

shield and eroded where it was not. This resulted in a gradual step having a height which could be measured using an optical interferometer (Angstrometer) after exposure to the beam had been terminated. Test specimens were typically 1 cm by 4 cm and the ion beam was sufficiently uniform that five such specimens could be exposed simultaneously. Several kinds of glass substrates ranging from optical flats to photographic plate glass were tried during the course of the tests and photographic plate glass was found to be sufficiently flat for this application.

Effect of Copper on Molybdenum Erosion Rates

Several tests were conducted wherein multilayer erosion samples (copper/molybdenum) were exposed to a 150 eV argon ion beam having a current density of 0.9 mA/cm^2. In order to obtain comparative data on the effects of copper four test specimens having the following compositions were exposed to the beam simultaneously:

- One molybdenum layer - 4500 Å thick
- Five molybdenum layers alternated with copper layers - each one 900 Å thick
- Ten molybdenum layers alternated with copper - each one 450 Å thick
- Twenty molybdenum layers alternated with copper - each one 225 Å thick

These specimens were fabricated at C.S.U. and considerable care was exercised to insure that they were kept clean. Molybdenum was always used as the top layer and the specimens were kept under vacuum to minimize oxidation except when they were being transferred between vacuum facilities.

Table II shows the erosion depths measured using the Angstrometer for each of the samples exposed to the ion beam during the conduct of the five tests. Column two shows the duration of each test. Columns three through six show the total erosion depths for the four different sample configurations. Immediately under each total depth are the calculated depths of molybdenum and copper (in parenthesis). For example in the second test, the specimen having five 900 Å molybdenum layers separated by five 900 Å copper layers showed a total erosion of 5712 Å; 3012 Å, of this thickness was estimated to be molybdenum and 2700 Å was estimated to be copper. The term "estimated depth" is used when referring to the copper and molybdenum because these depths were computed on the basis of nominal layer thicknesses. These nominal layer thicknesses were in turn determined from sputter deposition times divided by deposition rates for each material. Deposition rates were determined in a series of deposition calibration tests and were not measured on the actual specimens. It is interesting to note from the data of Table II that the depth of molybdenum eroded is only slightly less when copper is present than it is when none is present.

Several tests were conducted in which the erosion rates of copper and molybdenum were measured separately. Based on these tests it was found that copper eroded at 157 $\pm$ 39 Å/min and molybdenum eroded at 26.6 $\pm$ 4.5 Å/min. Using these erosion rates the time required to erode through the thicknesses of copper and molybdenum given in Table II were computed. The calculated times are presented in Table III for each of the samples tested along with the measured duration of each test. The bottom row of data in Table III shows the mean difference between the actual test times and the corresponding calculated values normalized

TABLE II

Copper/Molybdenum Test Results

Test	Test Duration (min)	One 4500 Å Moly	EROSION DEPTH DATA FOR		
			Five 900 Å Moly/Copper	Ten 450 Å Moly/Copper	Twenty 225 Å Moly/Copper
1	120	2836 Å (2836/0)	4819 Å (2700/2119)	5585 Å (2885/2700)	5153 Å (2678/2475)
2	120	3050 Å (3050/0)	5712 Å (3012/2700)	4870 Å (2620/2250)	4810 Å (2475/2335)
3	120	3135 Å (3135/0)	4254 Å (2454/1800)	4785 Å (2535/2250)	5562 Å (2862/2700)
4	120	2827 Å (2827/0)	4207 Å (2407/1800)	4240 Å (2250/1990)	4233 Å (2208/2025)
5	96	3297 Å (3297/0	5890 Å (3190/2700)	5890 Å (3150/2740)	6063 Å (3138/2925)

Key

Total depth
(Moly depth/Cu depth)

TABLE III

Effect of Copper on Molybdenum Sample Erosion Times

Test #	Test Duration (min)	Calculated Time to Reach Measured Depth (Min)			
		One 4500 Å Moly	Five 900 Å Moly/Copper	Ten 450 Å Moly/Copper	Twenty 225 Å Moly/Copper
1	120	107	115	126	117
2	120	115	130	113	108
3	120	118	104	110	125
4	120	106	102	97	96
5	96	124	137	136	137
Mean difference between measured and calculated times		0.00 ±0.17	0.04 ±0.24	0.03 ±0.23	0.03 ±0.24

using the actual test time for each of the sample configurations. These data suggest that the presence of both materials results in a 3% to 4% increase in erosion time over that value which would be expected from calculations based on erosion rates of pure materials. Further, the thickness of the layers does not appear to affect the results. It is noted however that the scatter in the data is large (with one standard deviation being 17% to 24%). These data do suggest however that erosion rates of molybdenum obtained using detectors fabricated using alternate layers of molybdenum and copper should give a reasonably accurate measure of erosion rates of the pure molybdenum at ion energies of 150 eV.

The tests reported in the preceeding paragraphs are not considered complete. Additional tests are planned in a cleaner lower background pressure environment. These tests will be conducted at ion energies that are closer to the doubly-charged ion energies observed in mercury bombardment thrusters.

Effect of Nitrogen on Erosion Rates

Numerous tests of the effects of background impurity gases on sputtering rates of discharge chamber materials are presently being conducted. In order to minimize the times required to obtain the data however, they are generally measured using alternatively layered badges similar to those just described or else these rates are inferred from optical line radiation measurements. Such radiation measurements examine the ratio of the radiation intensities for a test material line to that for a propellant line.

The purpose of the test described here was to measure the erosion rates of various materials directly as a function of nitrogen partial pressure in the bell jar where the sputtering was taking place. It should be pointed out that nitrogen entered the ion source where it became subject to ionization and dissociation. The current density of these various nitrogen species can be calculated using the model described in the next section of this report.

This study of the effect of nitrogen partial pressure on sputtering rates of discharge chamber materials was accomplished by fabricating (sputtering) samples of the test materials on glass substrates and then eroding them in the manner suggested in Figure 29. Three materials common to thruster construction were used in the test, namely: type 304 stainless steel, molybdenum and tantalum. Three samples were exposed to the 150 eV, C.9 mA/cm^2, argon ion beam simultaneously (one sample of each material). For each test conducted, the nitrogen partial pressure in the bell jar was set and maintained at a constant value. After the samples had been sputtered, they were removed and the height of the step machined in each sample was measured optically. Figure 30 shows the erosion rates determined by dividing this height by the test duration for the various materials at nitrogen partial pressures in the range around 10^{-4} torr. The data show a several fold reduction in erosion rate as nitrogen partial pressure is increased from about 10^{-6} torr to 3×10^{-4} torr. It should be pointed out that partial pressures near zero were not measured; rather, they were estimated to be of order 10^{-6} torr based on the nitrogen impurity level in the argon test gas and the ultimate pressure of the vacuum system. Recent tests have shown that nitrogen partial pressures should be below $\sim 10^{-8}$ torr are necessary to insure the protective effects of nitrogen are eliminated.[12]

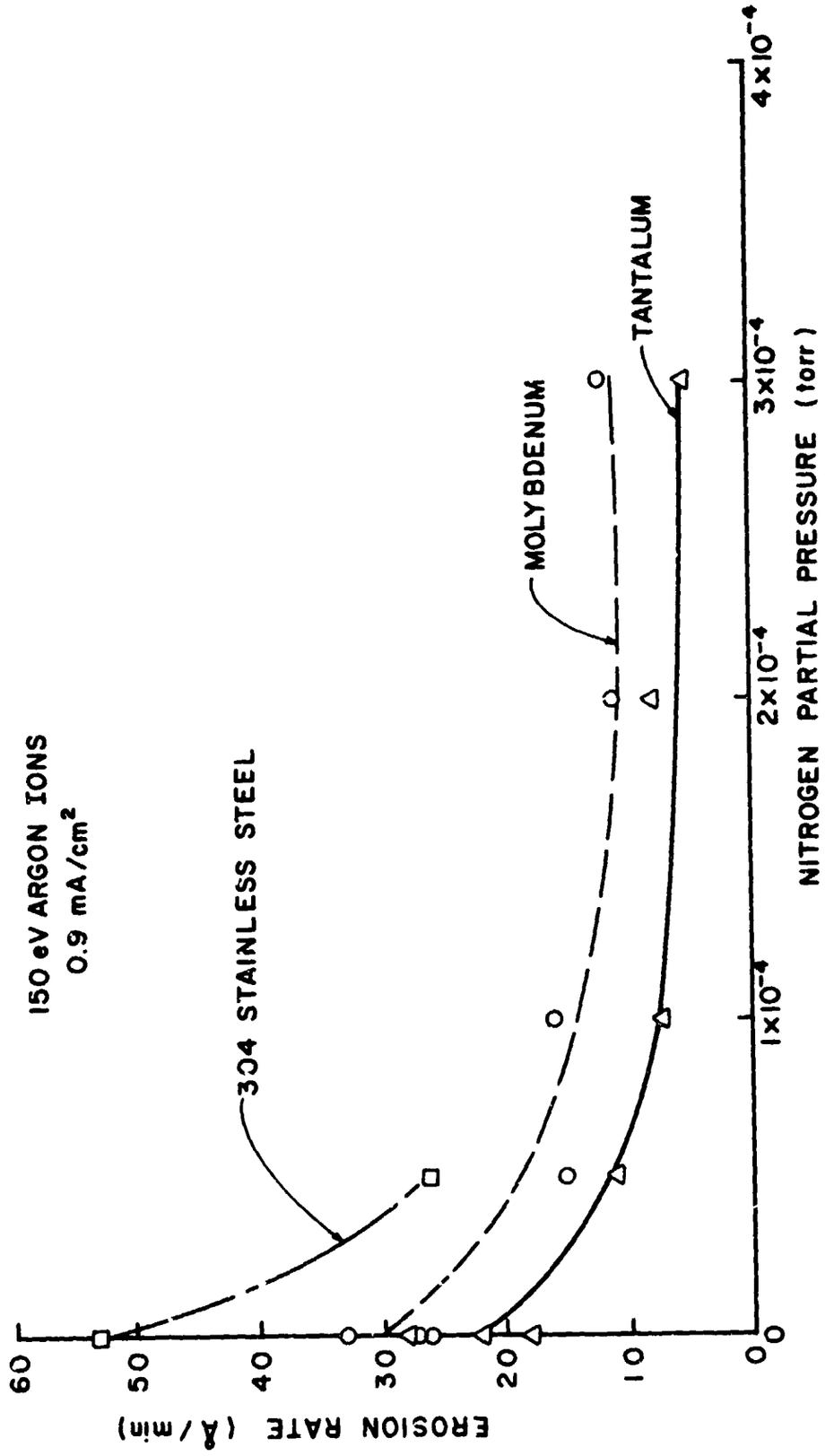

FIGURE 30. EFFECT OF NITROGEN ON SPUTTER EROSION RATES

A new, cleaner facility is being assembled to repeat these tests. They will be conducted at lower ion energies, closer to the energies of doubly-charged ions in discharge chambers.

Nitrogen Chemisorption Rates in Ion Thruster Discharge Chambers

It is desirable to be able to compute the effect of nitrogen on the erosion rates of thruster materials so data obtained with nitrogen present could be corrected. The first step in the development of such a model is to calculate the arrival rate of reactive nitrogen species on discharge chamber walls. Such a model is developed in the following paragraphs.

It appears that the observed reduction in erosion rates of thruster materials occurs as a result of sputter resistant nitrides of thruster materials which are formed when reactive atomic and ionic nitrogen produced in the thruster discharge chamber strike the thruster walls. In a typical discharge chamber, the electron-bombardment induced reactions that appear to be important in the generation of the reactive species are:

$$N_2 + e^- \rightarrow N^+ + N + 2e^- \quad (1)$$

$$N_2 + e^- \rightarrow 2N + e^- \quad (2)$$

$$N_2 + e^- \rightarrow N_2^+ + 2e^- \quad . \quad (3)$$

Of the species appearing in the above equations molecular nitrogen (N_2) is the most abundant. Nitrogen molecules probably do not react with the wall materials at a significant rate however for two reasons. First, the dissociation energy of this specie is high and sufficient energy to effect dissociation is not available at the wall. Second, the wall

temperature is sufficiently high to cause the molecules that strike chamber walls to be rejected from them almost immediately. It is obvious that atomic ions and atoms of nitrogen are very reactive and that they would be chemisorped on a surface when they strike it. The mechanism by which molecular ions are adsorped is not so obvious. This mechanism, referred to as impact-activated adsorption,[13] involves the acceleration of molecular ions to substantial energies through the plasma sheath which exists at cathode potential surfaces. These ions acquire sufficient energy as they pass through such a sheath that they can dissociate when they impact with the surface. The sticking coefficient for the atomic species should be essentially unity while that for the molecular ions is about 50% for impact with molybdenum surfaces at the ∿ 40 eV ion energies which might be expected from typical discharge chamber plasmas.[13] Calculation of arrival rates for the important species requires a knowledge of the reaction cross sections. Cross sections for the production of all atomic species lumped together (Eqn. 1 and 2) are given in Reference [13] as a function of bombarding electron energy.* Cross sections for the reaction of Equation (3) are given in Reference [14].

Theoretical Development

The rates for the reactions given in Eqns. (1), (2), and (3) are proportional to the molecular nitrogen density in the discharge chamber, and this density is in turn determined by the nitrogen balance between

* The cross sections for reaction of Eqn. (1) alone are given in Reference [15]. For the purposes of this work it is not necessary to distinguish between atomic ions and atoms so the lumped cross sections for the reactions of Eqns. (1) and (2) will be used.

inflow and outflow through the grids to and from the vacuum tank. Figure 31 is a schematic diagram of the vacuum tank containing a discharge chamber. In the vacuum chamber the nitrogen molecular density (n_o) is related to the nitrogen partial pressure (P_o) and the tank wall temperature (T_o in °K) through the state equation

$$n_o = \frac{P_o}{k\, T_o} \quad , \tag{4}$$

where k is Boltzmann's constant. It has been assumed here that the molecules are in good thermal communication with the tank walls so they equilibrate at tank wall temperatures.

The flow rate of molecular nitrogen into the thruster ($\dot{n}_o$) is given by

$$\dot{n}_o = \frac{n_o v_o A_A}{4} \tag{5}$$

where A_A is the open area of the accelerator grid and v_o, the mean molecular velocity, is given by

$$v_o = \sqrt{\frac{8\, k\, T_o}{\pi\, m_o}} \quad . \tag{6}$$

The quantity m_o is the nitrogen molecular mass.

As a result of electron bombardment of the discharge chamber, nitrogen molecules (N_2), atoms (N), ions (N^+) and molecular ions (N_2^+) will be produced and will reach equilibrium densities n_2, n_1, n_+ and n_{2+} respectively. The equivalent loss rate of nitrogen molecules ($\dot{n}$) from the discharge chamber as a result of migration of each of these species through the grids will then be

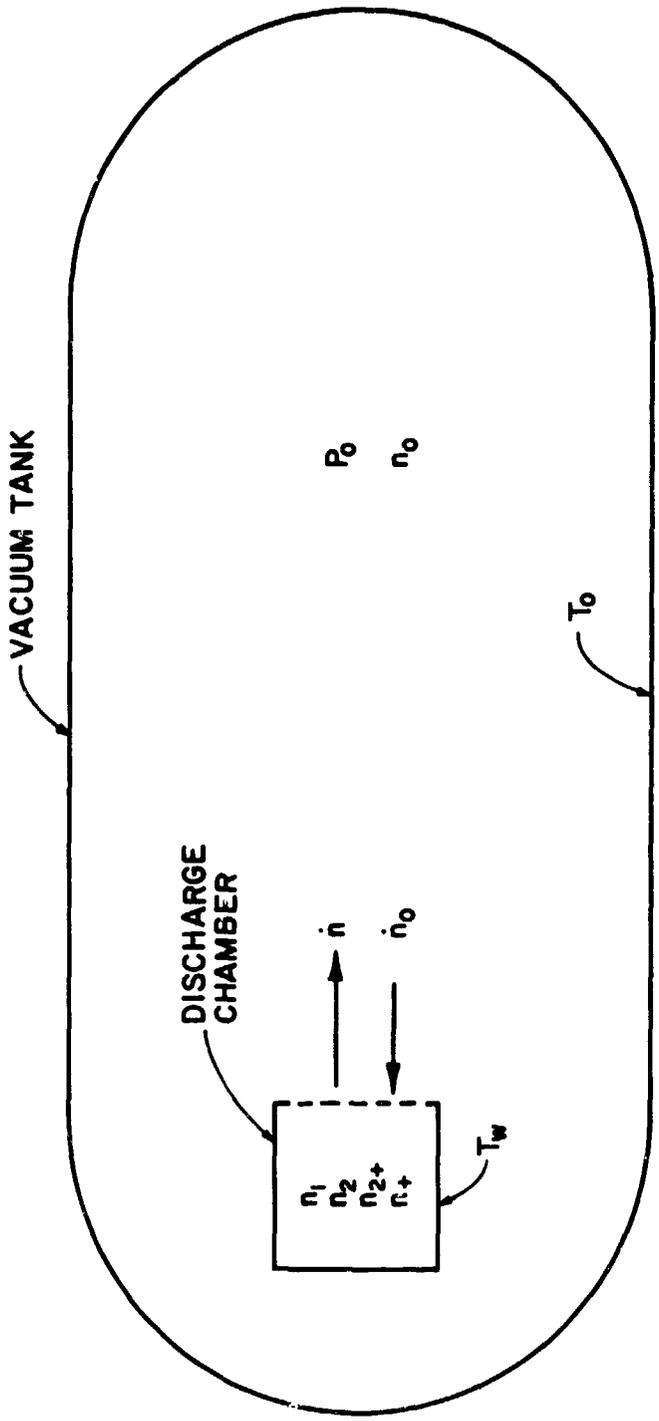

FIGURE 31. NITROGEN FLOW SCHEMATIC

$$\dot{n} = \frac{n_2 v_2 A_A}{4} + \frac{j_1 A_A}{2} + \frac{j_+ A_s}{2} + j_{2+} A_s \quad . \tag{7}$$

The symbols j_1, j_+ and j_{2+} represent respectively the particle current densities of nitrogen atoms, atomic ions and molecular ions through the grids. The quantity A_s is the screen grid open area and v_2 is the mean thermal velocity of nitrogen molecules and is given by

$$v_2 = \sqrt{\frac{8\ k\ T_w}{\pi\ m_o}} \quad . \tag{8}$$

In this equation T_w is the thruster wall temperature (°K).

Some of the nitrogen species going to the discharge chamber walls interact with the wall material and are retained in the discharge chamber after sputtering has occurred. The extent to which each of the species would be retained is not known, but because some could be retained, the equivalent molecular nitrogen loss rate from the chamber ($\dot{n}$) will be less than the rate of inflow. The fraction f describes this ratio of outflow to inflow through the equation

$$f = \dot{n}/\dot{n}_o \quad . \tag{9}$$

One would expect that while this fraction may be less than unity during the initial phases of discharge chamber operation it would eventually approach a steady-state value of unity.

Computation of the ionic and atomic specie densities is accomplished by equating the production and loss rates for each of these species to satisfy the steady-state continuity condition for each. The production rates for atomic ions ($\dot{p}_+$) and atoms ($\dot{p}_1$) and molecular ion ($\dot{p}_{2+}$) are given by

$$\dot{p}_+ = \dot{p}_1 = n_2[n_{pr}\ P_2^{1+}(\xi_{pr}) + n_{mx}\ Q_2^{1+}(T_{mx})]\ \Psi \quad , \tag{10}$$

$$\dot{p}_{2+} = n_2[n_{pr}\, P_2^{2+}(\xi_{pr}) + n_{mx}\, Q_2^{2+}(T_{mx})]\, \forall\ , \qquad (11)$$

where ξ_{pr} is the primary electron energy and $\forall$ is the primary electron region volume. The quantities n_{pr}, n_{mx}, ξ_{pr}, T_{mx} represent respectively the primary electron density, Maxwellian electron density, primary electron energy and Maxwellian electron temperature. Other quantities appearing in these equations are the production rate factors (electron velocity-cross section products) for the production of atomic ions or atoms by primary electrons ($P_2^{1+}(\xi_{pr})$) and Maxwellian electrons ($Q_2^{1+}(T_{mx})$) and the production of molecular ions by primary and Maxwellian electrons ($P_2^{2+}(\xi_{pr})$ and $Q_2^{2+}(T_{mx})$). These coefficients have been computed for nitrogen as a function of energy and temperature and they are plotted in Figures 32 through 35.

Because each of the species mentioned above are lost only as a result of migration to the surface of the primary electron region the production rates of Equations (10) and (11) can be equated to the loss rate at this boundary for each specie. This leads to the following set of equations:

$$j_1 = j_+ = \frac{\forall}{A}\, n_2[n_{pr}\, P_2^{1+}(\xi_{pr}) + n_{mx}\, Q_2^{1+}(T_{mx})] \qquad (12)$$

$$j_{2+} = \frac{\forall}{A}\, n_2\, [n_{pr}\, P_2^{2+}(\xi_{pr}) + n_{mx}\, Q_2^{2+}(T_{mx})] \qquad (13)$$

where A is the surface area of the primary electron region.

Equations (5), (6), (7), (8), (9), (12) and (13) may now be combined to obtain an expression for the molecular nitrogen density in the discharge chamber. This equation is

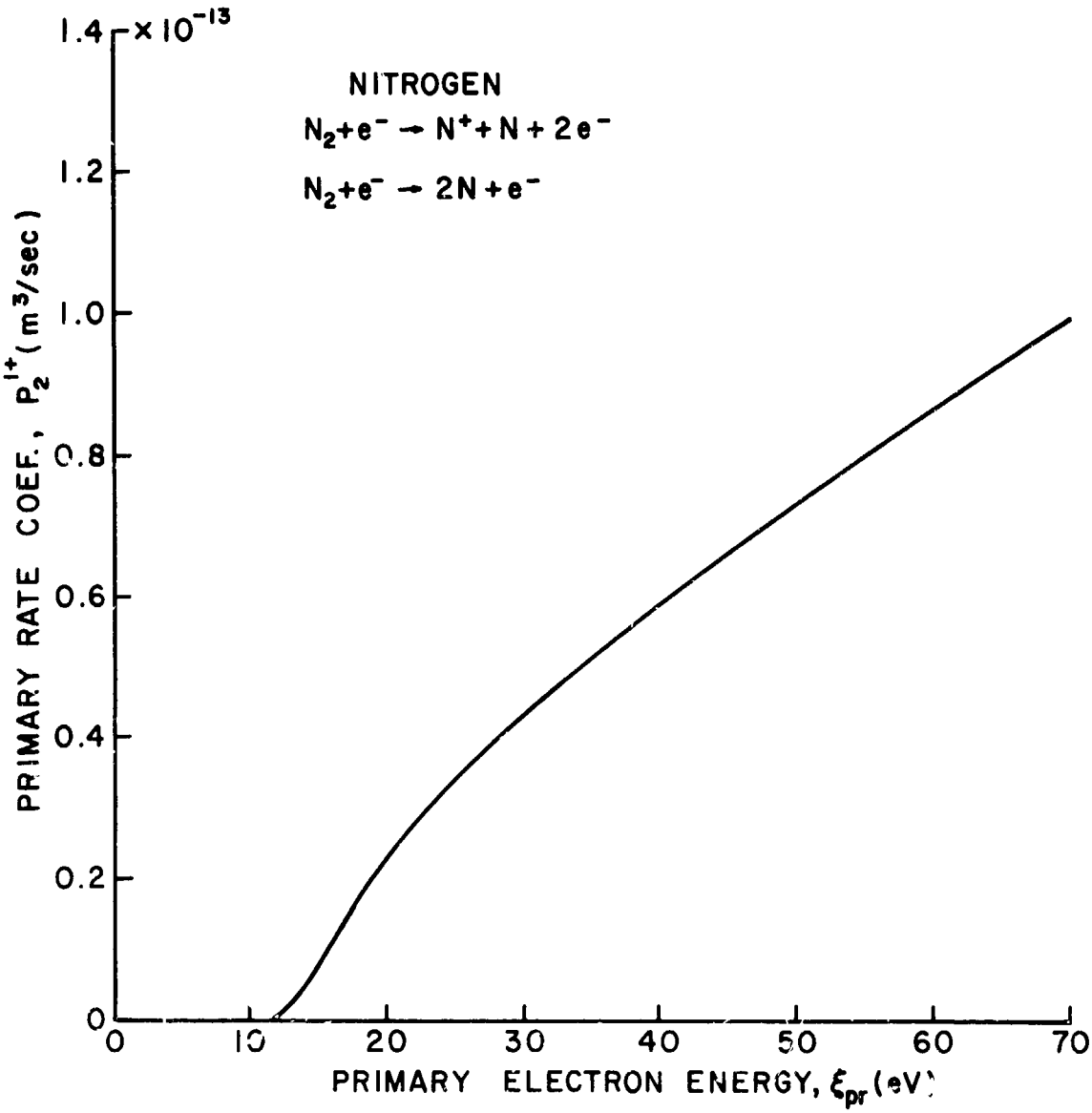

FIGURE 32. PRIMARY RATE COEFFICIENT FOR ATOMS AND ATOMIC IONS

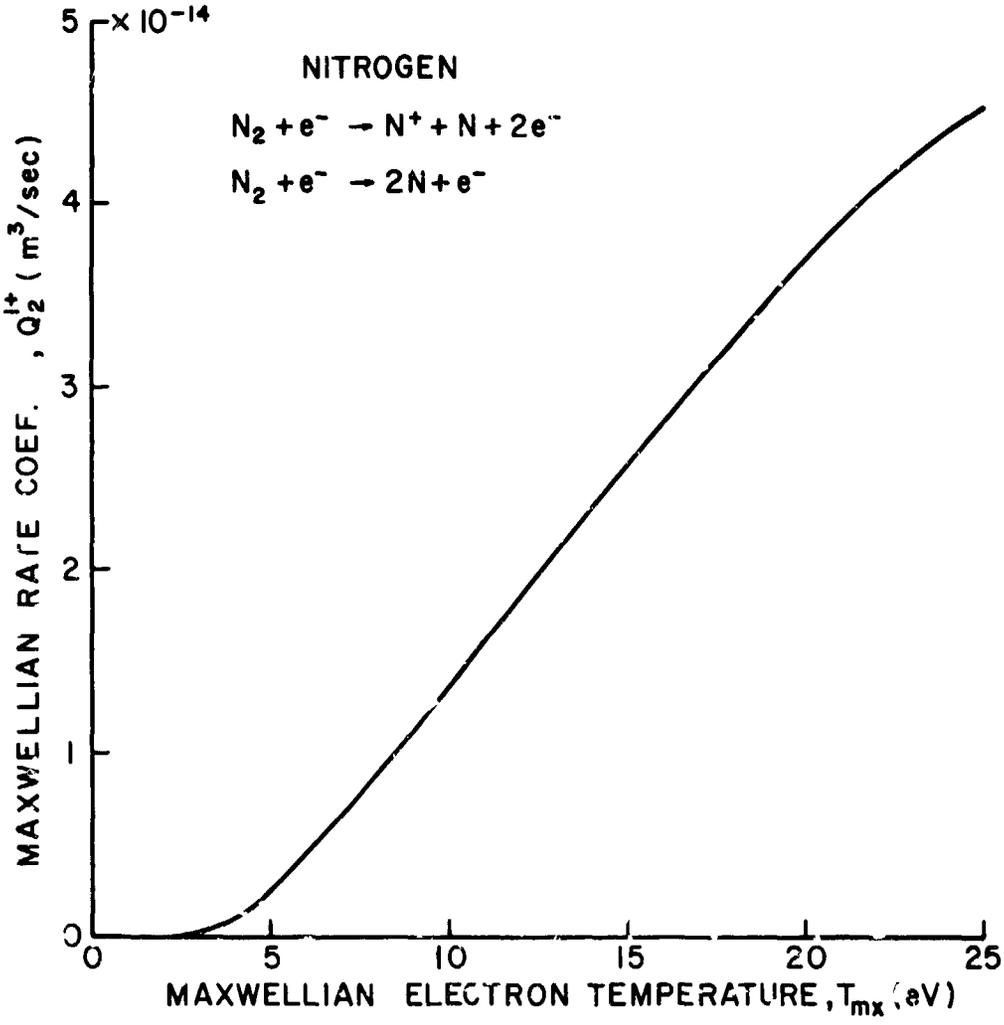

FIGURE 33. MAXWELLIAN RATE COEFFICIENT FOR ATOMS AND ATOMIC IONS

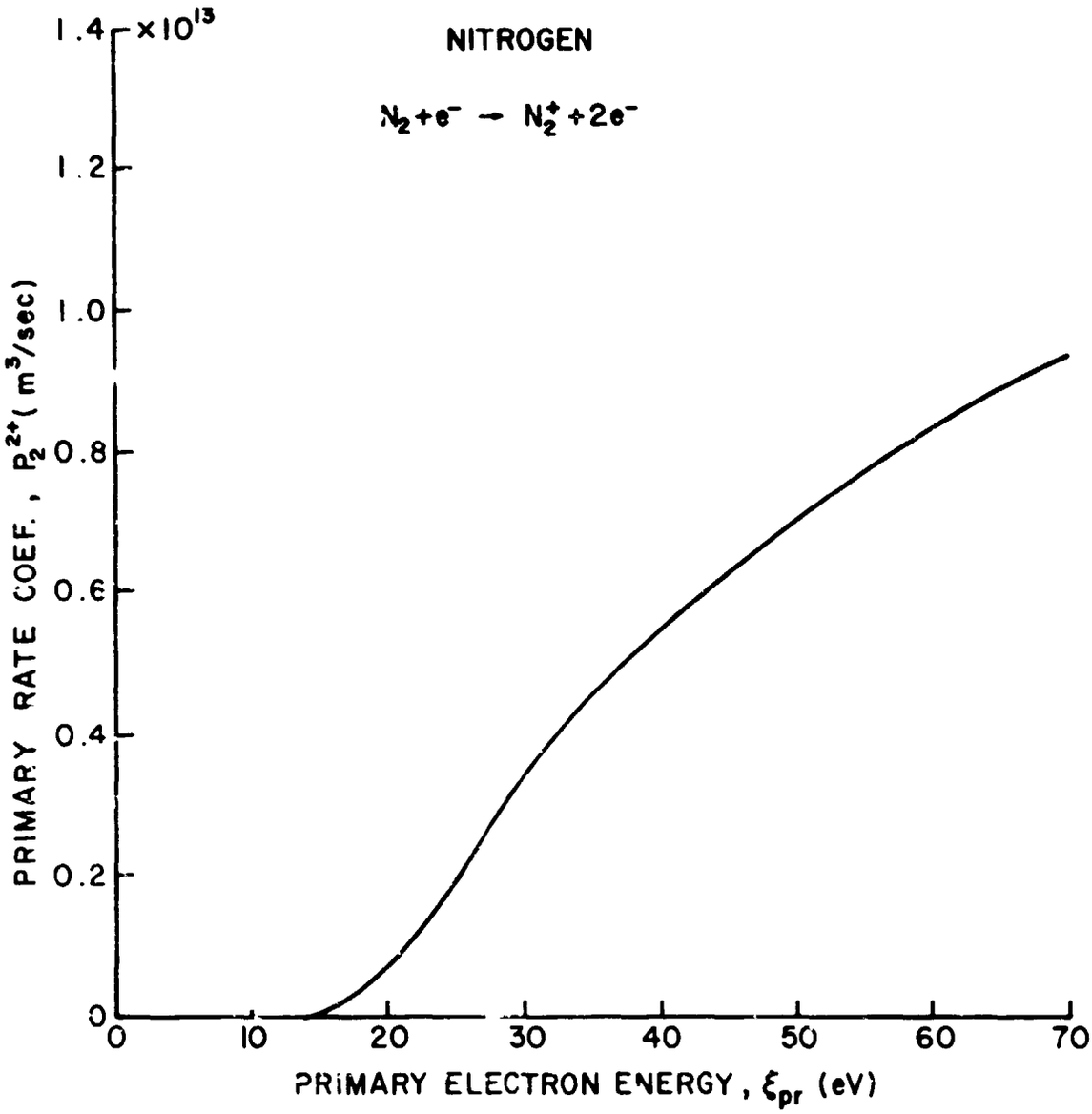

FIGURE 34. PRIMARY RATE COEFFICIENT FOR MOLECULAR IONS

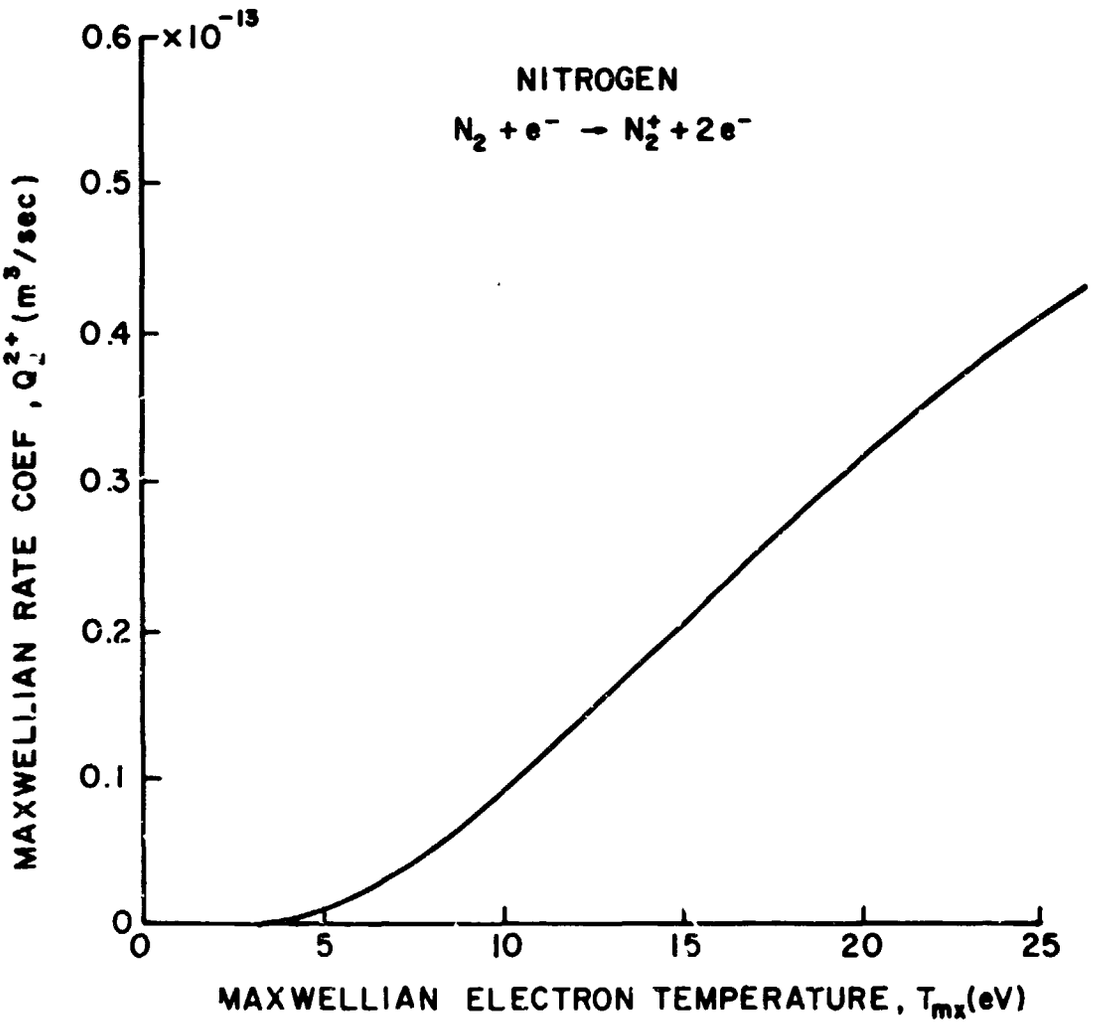

FIGURE 35. MAXWELLIAN RATE COEFFICIENT FOR MOLECULAR IONS

$$n_2 = \frac{f\, P_o\, [2\, k\, T_o\, \pi m_o]^{-\frac{1}{2}}}{\sqrt{\frac{k\, T_w}{2\, \pi m_o}} + \frac{\Psi}{2A}\left[\left(1 + \frac{A_s}{A_A}\right)\left(n_{pr}\, P_2^{1+} + n_{mx}\, Q_2^{1+}\right) + \left(n_{pr}\, P_2^{2+} + n_{mx}\, Q_2^{2+}\right)\frac{2A_s}{A_A}\right]} \quad (14)$$

Equations (12) through (14) can now be solved to determine first the density of molecular nitrogen in the discharge chamber and then the current density of the ionic and atomic species toward any discharge chamber surface or in the ion beam.

Typical Results

Using the following plasma and geometrical conditions typical of the 15 cm dia. argon thruster being used for sputtering tests along with appropriate constants one can obtain numerical values for these current densities.

T_o = 300°K

T_w = 500°K

A_s/A_A = 1

m_o = $(28)(1.67 \times 10^{-27}) = 4.68 \times 10^{-26}$ kg

V/A = 0.0182 m

k = 1.38×10^{-23} j/°K

n_{pr} = 1×10^{15} m^{-3}

n_{mx} = 1×10^{16} m^{-3}

ξ_{pr} = 40 eV

T_{mx} = 10 eV

f = 1

From Figures 32 to 35 the following rate coefficients pertaining to the primary and Maxwellian electrons are obtained at the electron temperature and energy conditions given above:

$$P_2^{2+} = 0.6 \times 10^{-13}\ m^3/sec,$$

$$Q_2^{2+} = 0.1 \times 10^{-13}\ m^3/sec,$$

$$P_2^{1+} = 0.6 \times 10^{-13}\ m^3/sec,$$

$$Q_2^{1+} = 1.4 \times 10^{-14}\ m^3/sec.$$

Using these values as input to Equations (12) through (14) the current densities in the third and fourth columns given in Table IV are calculated as a function of nitrogen partial pressure.

TABLE IV

Calculated Nitrogen Current

Densities in a Typical Thruster Plasma

Nitrogen Partial Pressure P_o (torr)	Molecular Nitrogen Density Within Thruster n_2 (m^{-3})	Atomic Specie Current Density $j_1 = j_+$ (A/m^2)	Molecular Ion Current Density j_{2+} (A/m^2)	Atom Retention Rates on Molybdenum	
				from Atomic Specie Current (atoms/m^2 sec)	from Molecular Ion Current (atoms/m^2 sec)
10^{-7}	2.4×10^{15}	0.0014	0 0011	9×10^{15}	7×10^{15}
10^{-6}	2.4×10^{16}	0.014	0.011	9×10^{16}	7×10^{16}
10^{-5}	2.4×10^{17}	0.14	0.11	9×10^{17}	7×10^{17}
10^{-4}	2.4×10^{18}	1.4	1.1	9×10^{18}	7×10^{18}
2×10^{-4}	4.9×10^{18}	2.8	2.2	2×10^{19}	1×10^{19}

To obtain atom, atomic ion or molecular ion arrival rates per unit area one must divide the values of columns three and four by the charge of an electron. Multiplying these values by the sticking probabilities appropriate to each specie, the atom retention rates given in columns

five and six of Table IV are obtained. A sticking probability of unity was used for the atomic ions and atoms (column 5). The sticking coefficient of 0.5 measured for 40 eV nitrogen molecular ions striking molybdenum[13] along with a factor of two, because two atoms are released when a molecule strikes wall, were used to obtain the results of column 6.

Conclusions

The presence of copper in multilayer molybdenum erosion detectors doesn't reduce the erosion rate by more than 3 to 4% from that rate that would be expected for pure molybdenum and copper for argon beam energies of about 150 eV. A several fold reduction in the erosion rates of thruster materials is observed as the nitrogen partial pressure is increased from about 10^{-6} to 3×10^{-4} torr.

Calculated chemisorption rates of nitrogen atoms on molybdenum screen grids in typical bombardment ion thrusters are of order 2×10^{17} m^{-2} sec^{-1} at a nitrogen partial pressure of 10^{-6} torr. About half of these atoms are produced as atomic species in the discharge plasma and the other half are produced from molecular ions which acquire sufficient energy in the plasma sheath to dissociate when they impact the surface.

PLASMA PROPERTY CORRELATIONS

It is frequently desirable to know the plasma conditions existing within a discharge chamber so calculations of such quantities as the doubly-charged ion density can be made. Collection of these data is, however, time consuming and one must have operational hardware available in which to make the measurements. During the development of the doubly-charged ion production model[16] a substantial amount of plasma property data were obtained in 15 cm dia and 30 cm dia discharge chambers. These data were correlated with parameters formulated from operational and design variables, so predictive calculations requiring plasma data could be made. Plasma property data have been collected more recently in the 8 cm discharge chamber.[17] These have been incorporated into the new volume-averaged plasma property correlations for divergent field thrusters which are shown in Figures 36 through 39. No attempt has been made in these correlations to establish a physical basis for the selection of the correlating parameters. Instead, the exponents of the variables comprising each correlating parameter were simply adjusted until the correlation coefficient r for a least squares linear curve fit for each set of data was maximized. The variables that were used to generate the correlating parameter were:

discharge voltage	- V_D
discharge current	- I_D
beam current	- I_B
volume-to-surface area ratio of the primary electron region in the discharge chamber	- $\forall/A$
open area fraction of the accelerator grid	- ϕ_a

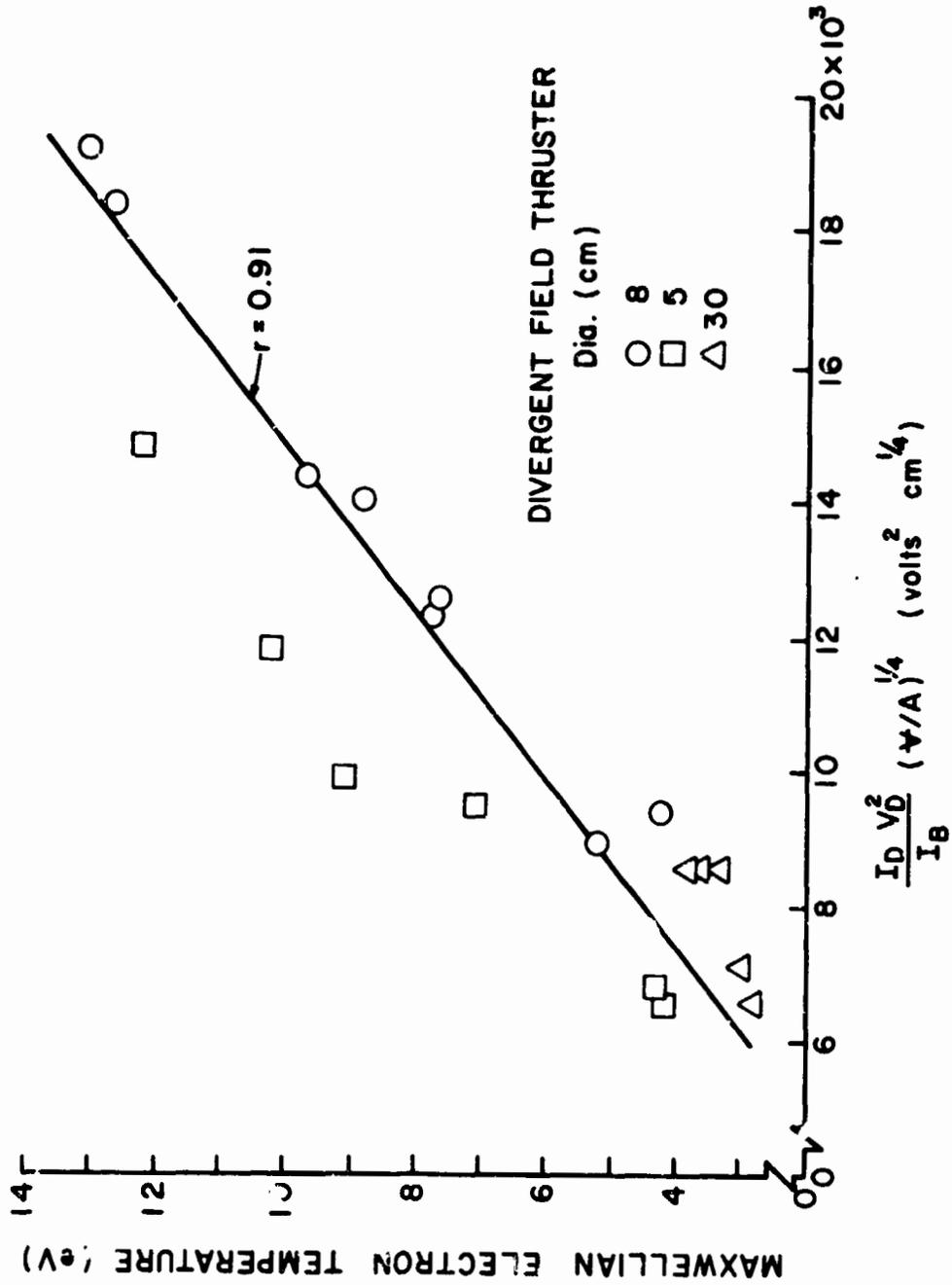

FIGURE 36. MAXWELLIAN ELECTRON TEMPERATURE CORRELATION FOR MERCURY, DIVERGENT FIELD THRUSTERS

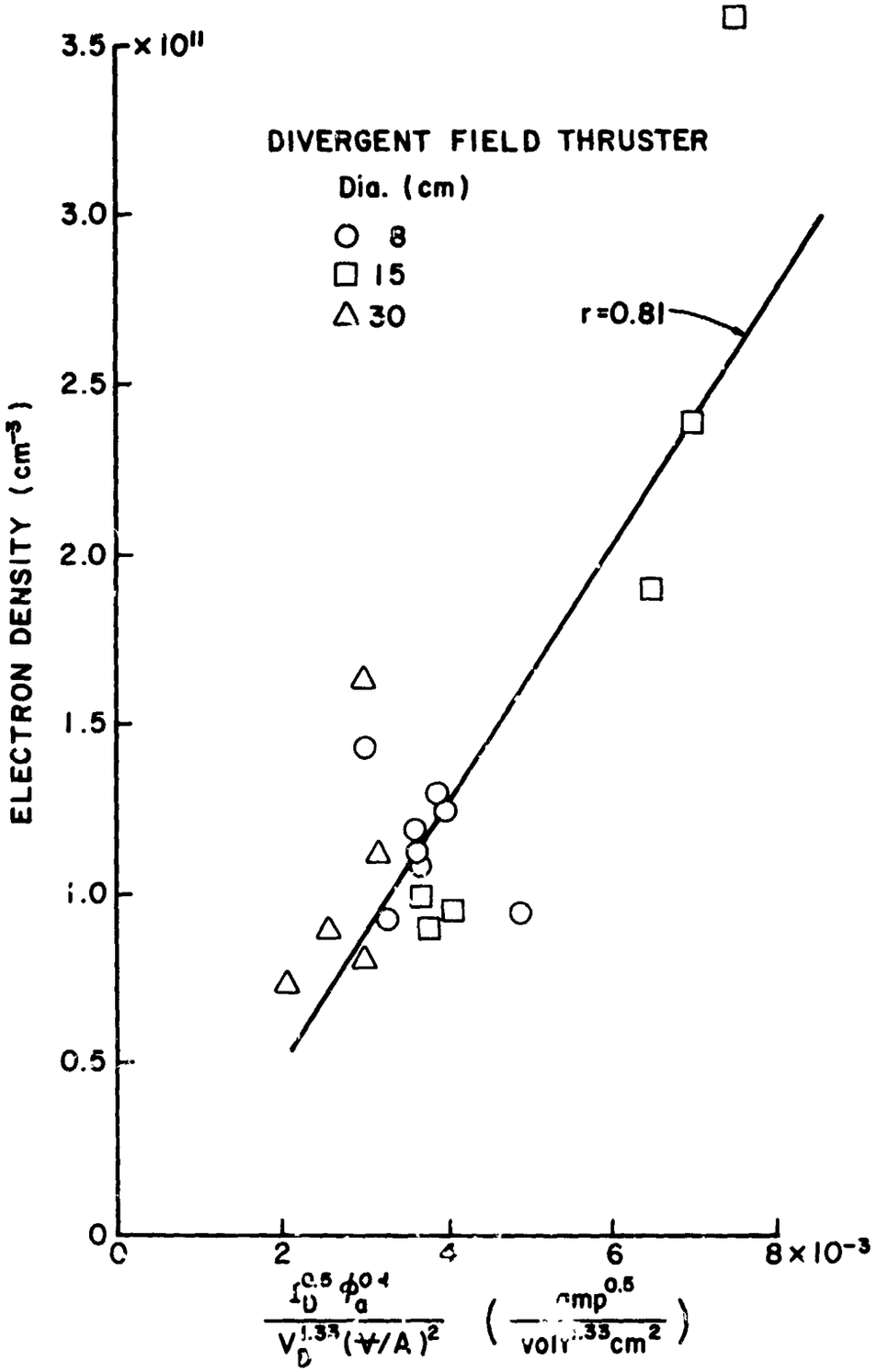

FIGURE 37. ELECTRON DENSITY CORRELATION FOR MERCURY, DIVERGENT FIELD THRUSTERS

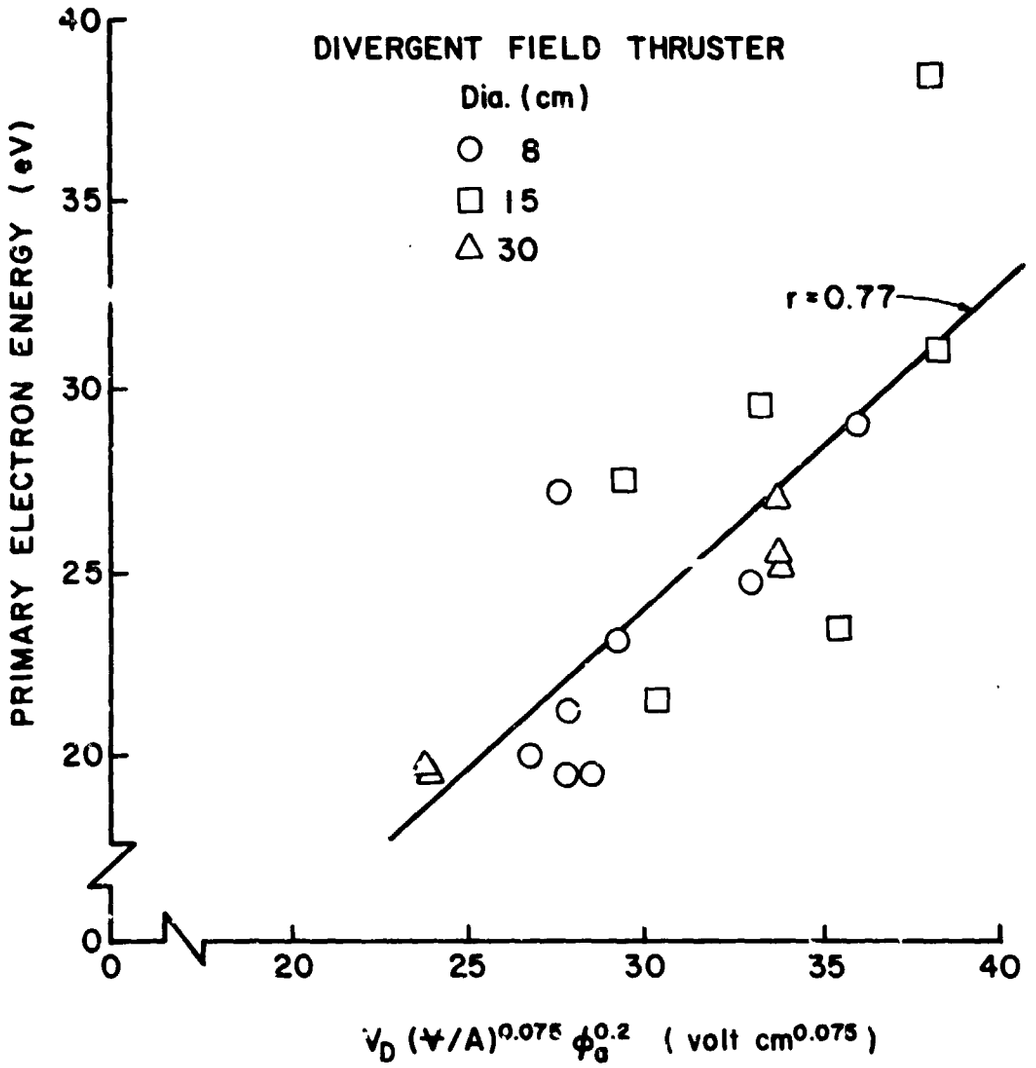

FIGURE 38. PRIMARY ELECTRON ENERGY CORRELATION FOR MERCURY, DIVERGENT FIELD THRUSTERS

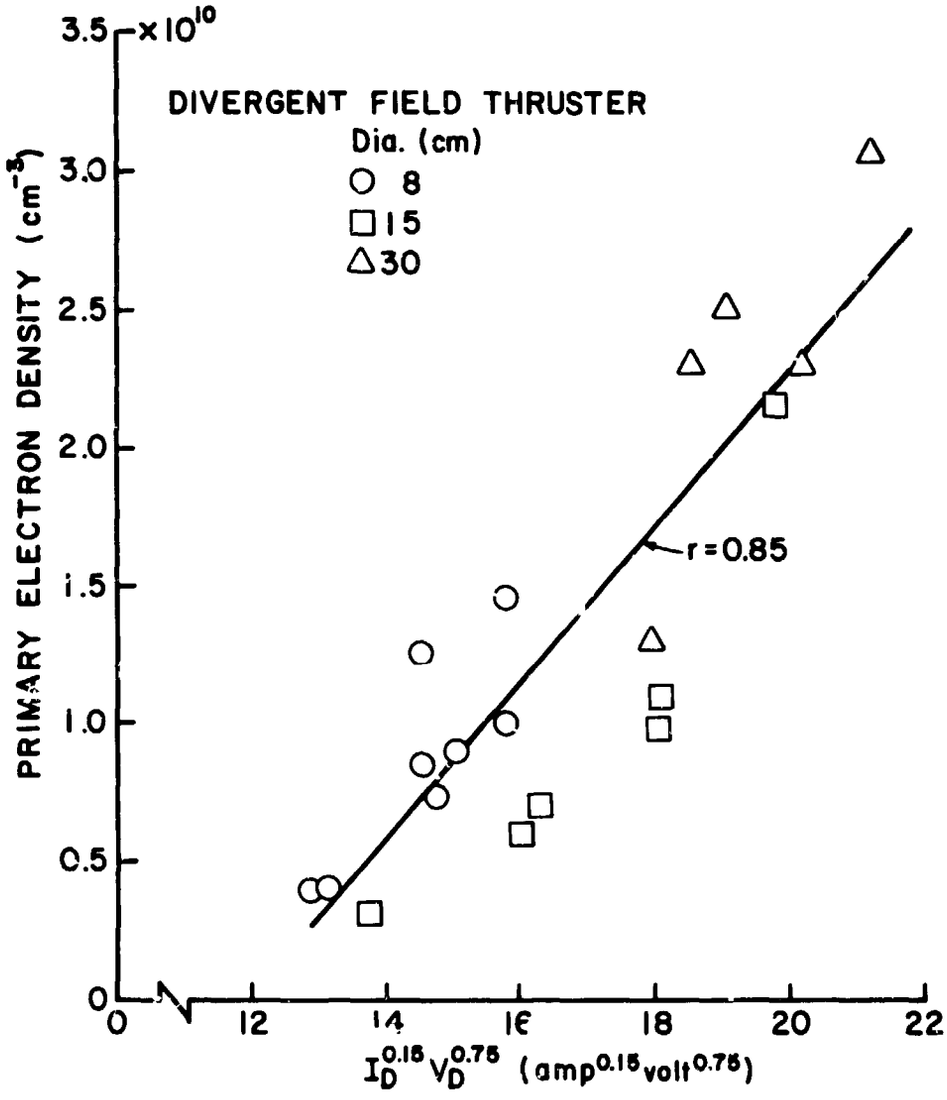

FIGURE 39. PRIMARY ELECTRON DENSITY CORRELATION FOR MERCURY, DIVERGENT FIELD THRUSTERS

Figure 36 shows for example the volume-averaged, Maxwellian electron temperature correlation with the parameter $I_D V_D^2(\Psi/A)^{1/4}/I_B$. This parameter gave a correlation coefficient of 0.91 and it represented the best correlation observed. Figures 37, 38 and 39 show similar correlations for other volume-averaged plasma properties of interest, namely total electron density, primary electron energy and primary electron density respectively. The data used to obtain these correlations while they were all obtained in divergent field thrusters were collected at a variety of operating conditions and with various accelerator grids. There is always a possibility that some variable, unaccounted for in an empirical correlation will be varied in a new design or at a new operating condition. The attempt to vary design and operating conditions as much as possible in order to minimize the chances for this has been made however in the data of Figures 36 through 39.

RADIAL FIELD THRUSTER

This discharge chamber design concept, first proposed by Knauer, Poeschel and Ward,[18] has been investigated because it offers the potential of operation under conditions where the lifetime limiting screen grid erosion observed in other designs could be reduced. The means whereby this should be possible can be understood by considering Figure 40, a schematic of the thruster with an iron filings magnetic field map super-imposed.

In the operating mode proposed by Knauer, Poeschel and Ward, electrons generated at the cathode were accelerated into the main discharge region through the series of small holes shown in the center pole piece. These primary electrons were generally confined to the primary electron region shown in Figure 40 by the radial magnetic field lines-of-force. As these electrons gyrate within the primary electron region, they undergo collisions and are able to migrate upstream toward the anode under the influence of the prevailing electric field. As a result of the collisions, electrons having a Maxwellian distribution function and ions are produced. Two sets of magnets shown in Figure 40 are used to produce the desired magnetic field shape. Radial magnets are used to produce the general field in both configurations, intensity and the axial magnets are used to tune it up by adjusting axial location of the critical field lines near the outer radius of the discharge chamber. The cathode has a 0.32 cm dia orifice plate with a 0.76 mm dia. orifice in it. The center pole piece is 1.9 cm in outside diameter and 1.5 cm inside diameter. The discharge chamber diameter for the thruster used in these tests was about 14 cm. The unit was operated with a high perveance dished grid set having a 67% open area

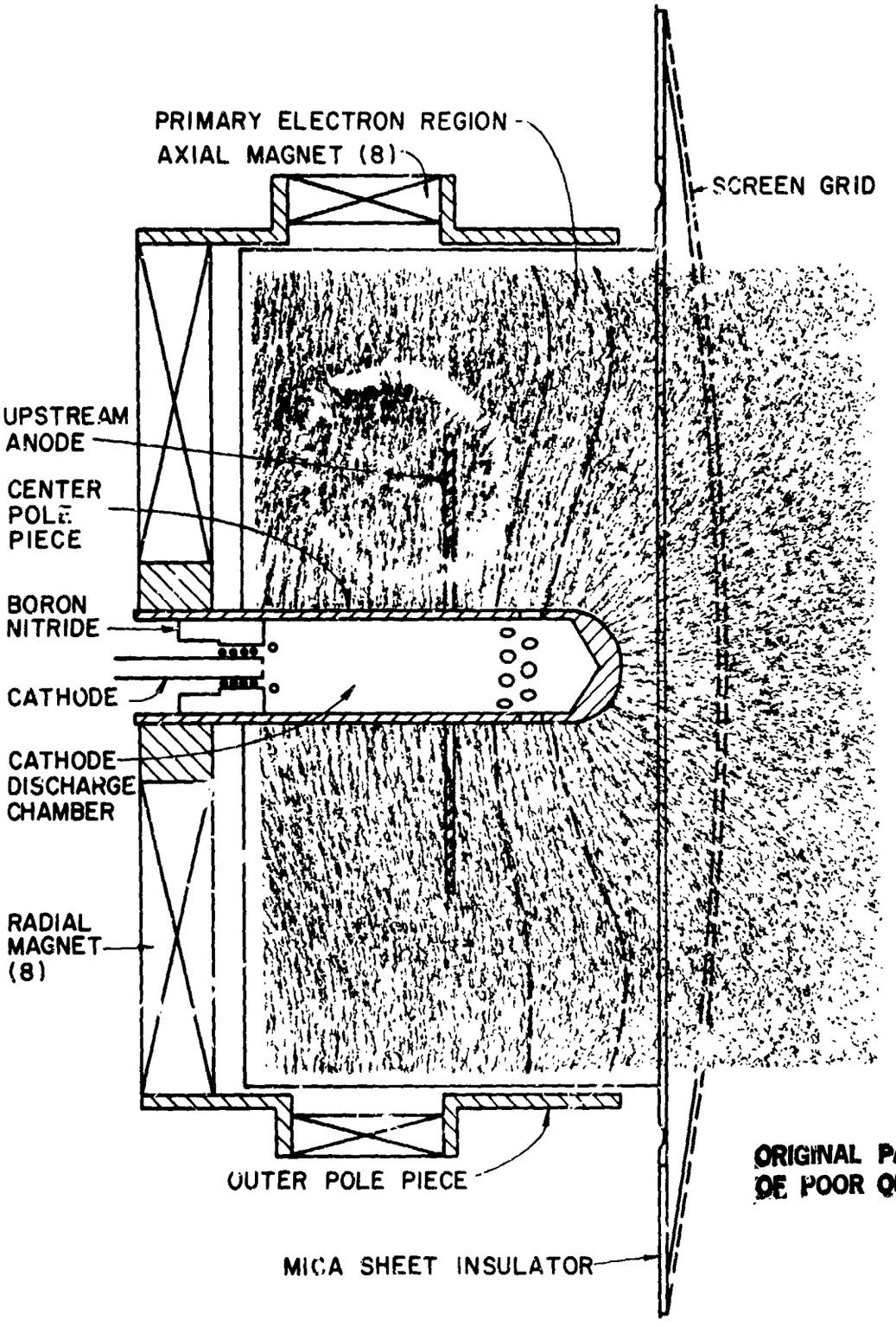

RADIAL MAGNETIC FIELD THRUSTER SCHEMATIC

FIGURE 40

screen grid and a 54% open area accelerator grid.

The method for reducing screen grid erosion with this discharge chamber involves biasing the screen grid above cathode potential. This reduces screen grid erosion damage because increasing the potential of the screen grid results in a reduction of the energy of the incoming ions that are responsible for sputtering damage (this energy is proportional to the difference between plasma potential and screen grid potential). Because the sputtering yield varies as the cube of the energy at which these ions impact (in this energy range), small increases in the screen grid potential result in substantial reductions in the rate of screen grid erosion. With this particular discharge chamber configuration it was expected that the screen grid could be biased substantially above the cathode potential at which screen grids normally operate without degrading discharge chamber performance. This was anticipated because the primary electron region does not intersect the radial thruster screen grid - primary electrons should, therefore, not have direct access to it.

Experimental Results

This concept has been examined experimentally and the results obtained with the configuration shown in Figure 40 have been reported previously.[19] The data were obtained at a screen potential of + 1000 v and an accelerator potential of - 500 v. The configuration of Figure 40 did not perform satisfactorily however because a suitable hole size for the apertures in the center pole piece could not be found. These holes were either too small, in which case the main discharge could not be ignited once the cathode was operating, or they were too large and the proper impedance

could not be maintained across them. The configuration shown in Figure 41 was therefore adopted. With this center pole piece arrangement magnetic field lines passed through the aperture from the center pole piece to the center pole piece tip. This resulted in adequate impedance in the aperture and a substantial improvement in performance. The performance achieved with this configuration is shown in Figure 42 at a total flow rate of 730 mA eq. as the dotted line. This performance was observed with the screen grid at cathode potential. The three solid symbols shown indicate performance at a discharge voltage of 37 v. The discharge power-propellant utilization curve for the divergent magnetic field SERT II thruster is shown as the solid line to facilitate comparison. The SERT II discharge chamber is observed to exhibit substantially better performance.

A number of discharge chamber modifications were attempted in an effort to improve the radial field thruster performance. These included adjusting the position of the anode, varying the width of the aperture gap, changing the magnetic field intensity and shape through the use of the radial and axial electromagnets and moving the cathode axially within the center pole piece. The thruster was arranged so all of the alterations could be accomplished while the thruster was operating. The greatest improvement in performance was brought about by moving the cathode downstream to a location very near the aperture. The preferred anode position was slightly upstream of the aperture and the preferred aperture gap was 0.89 cm. Tuning of these variables resulted in the performance shown by the lowest curve in Figure 42. While the performance observed with this configuration is much improved over that observed with the cathode upstream and slightly better than that observed with SERT II,

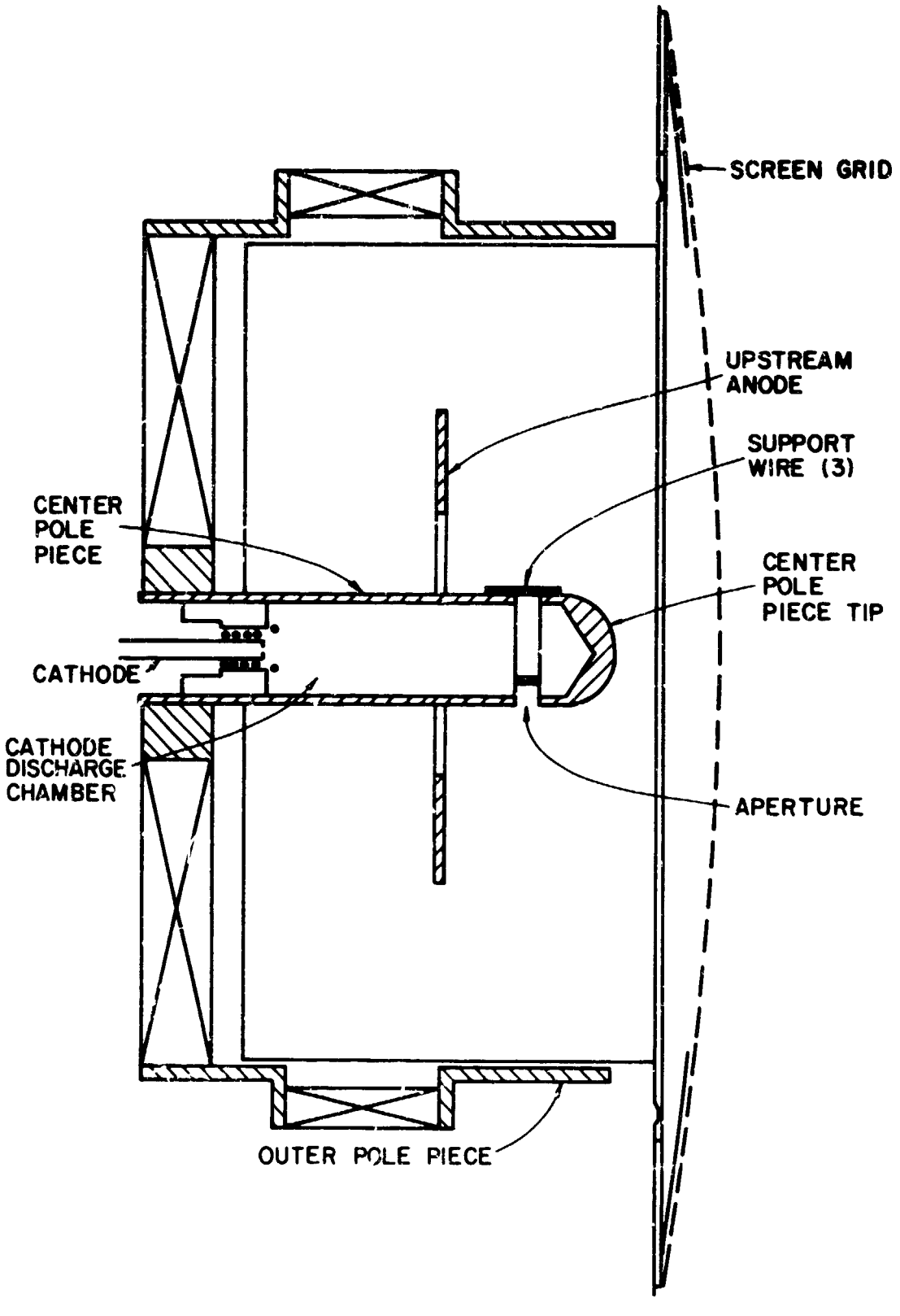

RADIAL THRUSTER/SLOT APERTURE CONFIGURATION

FIGURE 41.

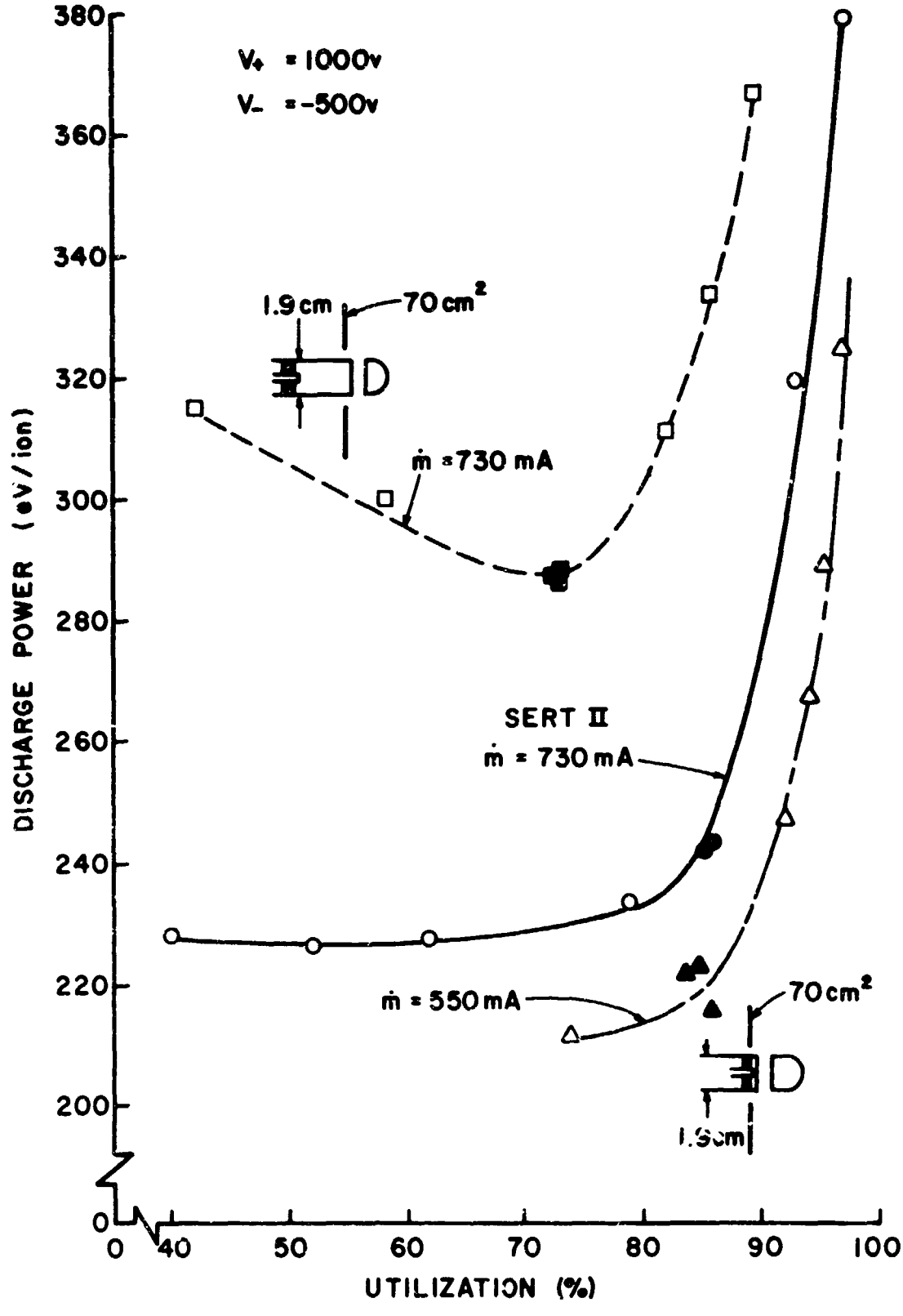

FIGURE 42. RADIAL FIELD THRUSTER PERFORMANCE COMPARISON

it was found that the maximum flow rate at which this discharge chamber could operate was substantially reduced. As Figure 42 suggests this limiting flow rate was about 550 mA. Flow rates beyond this resulted in excessive impingement currents and high voltage cycling. With the thruster in this configuration the effect of screen grid bias on thruster performance was examined. It was observed that this grid could be biased over the range from cathode potential to floating potential without causing any noticeable change in the lowest curve shown in Figure 42. Typically the floating potential was about 10 volts and attempts to bias the screen grid to potentials above the floating potential resulted in a rapid degradation in performance.

In order to extend the flow rate range over which the discharge chamber could be operated, the center pole piece diameter was increased. The justification for this was that the discharge chamber operated stably at a higher flow rate when the cathode was upstream and it was postulated that this occurred because the cathode discharge region volume was greater. It was argued that increasing the center pole piece diameter would again increase this volume and hence the maximum flow rate.

The solid line on Figure 43 shows the performance curve obtained with the radial field thruster when the pole piece outside diameter was increased to 2.5 cm from the 1.9 cm diameter used in obtaining the data of Figure 42. The larger pole piece diameter did facilitate operation at a higher flow rate, but it resulted in poorer thruster performance. In order to regain some of this performance loss, the upstream anode area was increased from the 70 cm^2 used to obtain the previous data (all of Figure 42 and the solid line date of Figure 43) to 120 cm^2. This resulted in a thruster performance improvement to the level shown by the

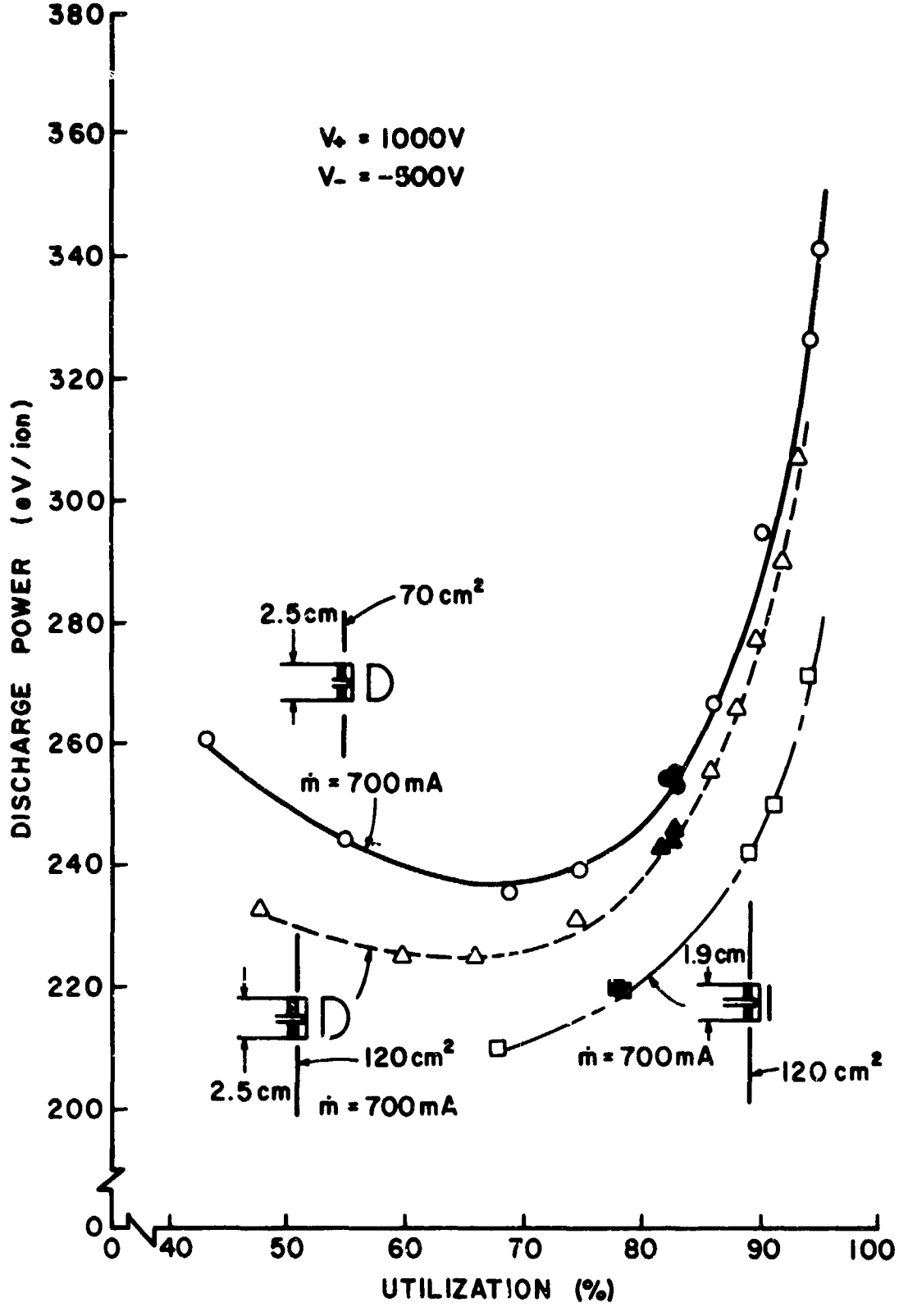

FIGURE 43. RADIAL FIELD THRUSTER PERFORMANCE

dotted line of Figure 43 without the loss of capacity to perform at the higher flow rates. Next the pole piece diameter was reduced to 1.9 cm^2 and the center pole piece tip was replaced by a flat baffle. This resulted in a further improvement in performance again without any loss in capacity to perform at the higher flow rate level. One additional test was run using a 2.5 cm dia. pole piece, 120 cm^2 anode and a flat baffle. The performance achieved with this configuration was similar to that represented by the lowest curve on Figure 43 at a 700 mA flow rate. Operation at flow rates above 700 mA were possible with this configuration although some degradation in performance was observed when the flow rate was increased to 830 mA. It is noted that increasing the anode area in divergent field thrusters has not been observed to improve their performance[20] while it does appear to have done so for the radial field thruster data of Figure 43. Eliminating volumes such as that of the center pole piece tip, which tends to displace ionizing electrons and provide a surface for recombination, in favor of a simple flat baffle has previously been observed to improve performance.[19]

In testing each of the configurations represented on Figure 43 the screen grid was operated at both cathode potential and floating potential (~10 v). Changing between these potentials resulted in negligible shifts in the performance curves. These results suggest that the radial field thruster can be operated with the screen grid at floating potential with no adverse effect on performance.

One aspect of radial field thruster operation which was disappointing pertains to the flatness of the ion beam profile from this thruster. It was anticipated that these profiles would be considerably flatter than profiles measured on divergent field configurations. Figure 44 shows

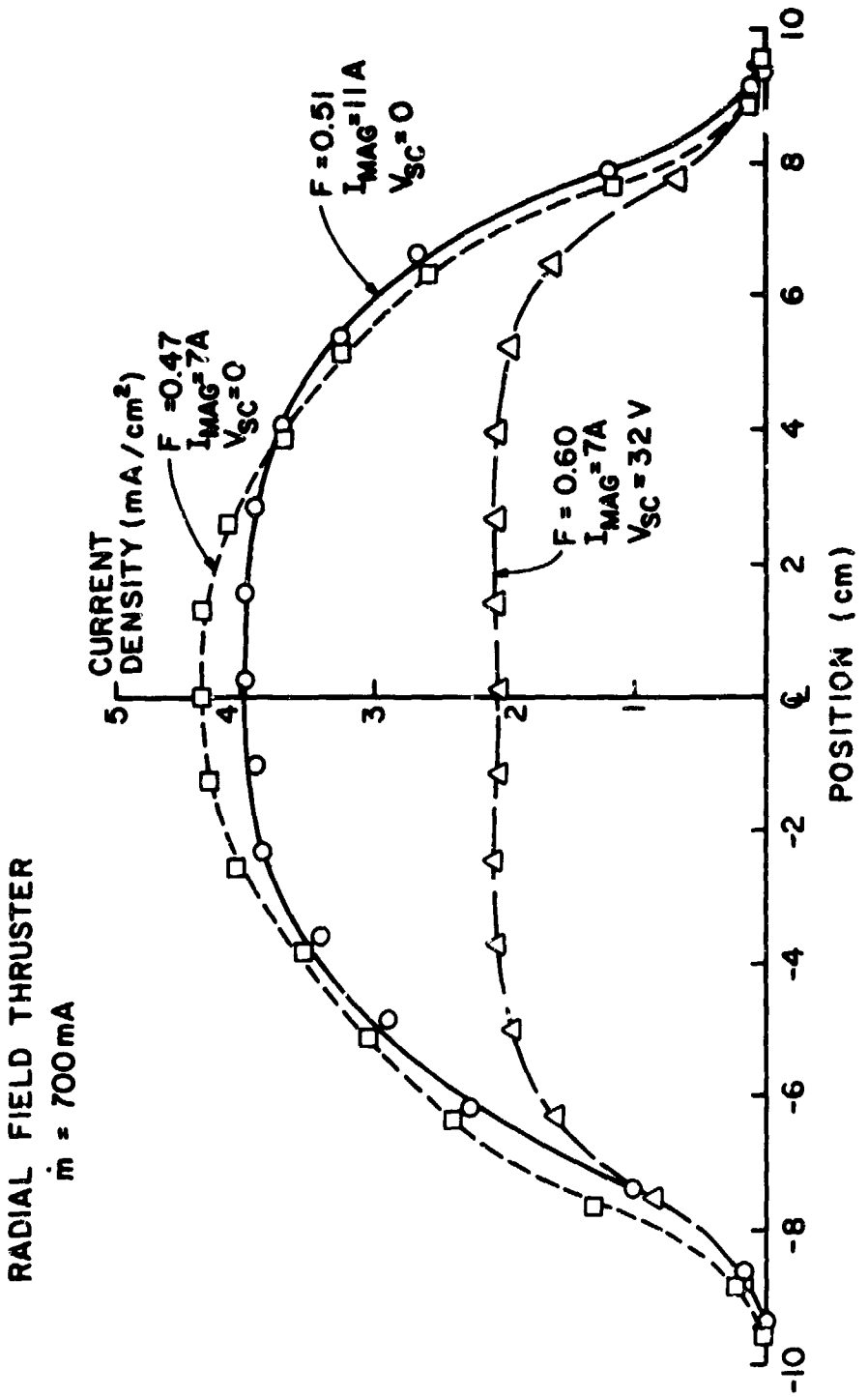

FIGURE 44. RADIAL FIELD THRUSTER ION BEAM PROFILES

some typical ion beam profiles measured on the radial field thruster using a Faraday probe located 2.5 cm downstream of the accel grid at its centerline. The parameter F describes the beam profile flatness and is defined as the ratio of average to peak beam current densities. For the SERT II thruster this parameter had a value near 0.49.[21] The design changes introduced into the radial field thruster to improve its performance (anode area and location, cathode location, center pole piece diameter and baffle aperture width) were observed to have no significant effect of the ion beam profile. One parameter which did seem to have an effect on ion beam profile was the radial magnet field current (I_{mag}). As it was increased from 7 A to 11 A it caused the profile to flatten slightly as suggested by comparing the dotted and solid curves on Figure 44. It is interesting to note that increasing the magnet current from 7 A to 11 A also resulted in an increase in the floating potential of the screen grid from near 10 volts to near 17 volts. It appears therefore that increasing the magnetic field intensity is beneficial for two reasons; namely because it flattens the beam profile and it increases the floating potential of the screen grid thereby making it possible to reduce the energy of ions sputtering its surface.

Physically one would expect the ion beam to flatten and the floating potential of the screen grid to increase as magnetic field intensity was increased. These effects are presumably a result of the more effective confinement of electrons to the primary electron region (Figure 40) brought about by the increased magnetic fields. These effects of the magnetic field have not yet been studied systematically, but such a study is planned over a larger range of magnetic fields than have been investigated here.

The data represented by the solid and dotted lines of Figure 44 were obtained with the screen grid at cathode potential, but allowing the screen grid to float resulted in no measurable change in these data. Biasing the screen grid to near-anode potential did, however, result in additional flattening of this profile. With the screen grid at 32 v (anode voltage 37 v), the ion beam profile represented by the dashed line was measured. The reason for the flattening of the beam profile here can be understood by considering the discharge chamber schematic shown in Figure 40. When the screen grid is biased near anode potential, electrons located downstream of the primary electron region can be collected. These electrons, while they may not be true primary electrons, generally have sufficient energy to ionize some propellant atoms. When these electrons are collected ion production near the thruster centerline is reduced. This not only flattens the ion beam profile, but also degrades the thruster performance because of the loss of electrons which have sufficiently high energies that they can ionize atoms.

Conclusions

Performance comparable to that of the SERT II thruster can be achieved in the radial field thruster. The screen grid of the radial field thruster can be biased to floating potential with no adverse effect on discharge chamber performance. This bias, which is of order 10 volts, should be sufficient to reduce the energy of doubly charged propellant ions about 20 eV, and hence, reduce the sputtering damage which they cause substantially. For example, in the 30 cm dia thruster reducing the potential difference through which ions are accelerated into the grids from 38 to 28 volts should result in about a fivefold increase

in grid lifetime and reducing this potential difference from 36 to 26 volts should result in about a tenfold increase in lifetime.[22]

The ion beam profile of this thruster is not as flat as was expected. Attempts to flatten it further will focus on changing the magnetic field intensity in the discharge chamber.

REFERENCES

1. Longhurst, G. R., "Prediction of Plasma Properties in Mercury Ion Thrusters," NASA CR 159448, Dec. 1978.

2. Banks, B. A., "8-cm Mercury Ion Thruster System Technology," AIAA Paper 74-1116, AIAA/SAE 10th Propulsion Conference, San Diego, Calif., 1974.

3. Herron, B. G. et al, "Engineering Model 8-cm Thruster System," AIAA Paper 78-646, AIAA/DGLR 13th Electric Propulsion Conference, San Diego, Calif., 1978.

4. Siegfried, D. E. and Wilbur, P. J., "An Investigation of Mercury Hollow Cathode Phenomena," AIAA Paper No. 78-705, April 1978.

5. Hamza, V. and Richley, E. A., "Numerical Evaluation of Ion-Thruster Optics," NASA TN D-1665, May, 1963.

6. Golden, D. S. and Cohen, E., "Plasma Extraction Optics Study," TRW Report No. 14176-6001-TO-00, Sept., 1971.

7. Aston, G., Kaufman, H. R. and Wilbur, P. J., "Ion Beam Divergence Characteristics of Two-Grid Accelerator Systems," AIAA Journal, Vol. 16, No. 5, May 1978, pp. 516-524.

8. Aston, G. and Kaufman, H. R., "Ion Beam Divergence Characteristics of Three-Grid Accelerator Systems," AIAA Paper No. 78-669, 1978.

9. Banks, B. A. and Bechtel, R. T., "1000-Hour Endurance Test of a Glass-Coated Accelerator Grid on a 15-centimeter-Diameter Kaufman Thruster," NASA TN D-5891, July, 1970.

10. Rawlin, V. K. and M. A. Mantenieks, "Effect of Facility Background Gases on Internal Erosion of the 30-cm Hg Ion Thruster," AIAA Paper 78-665, April 1978.

11. Wehner, G. K. and D. J. Hajicek, "Cone Formation on Metal Targets During Sputtering," Jour. of App. Phys., V. 42, No. 3, March, 1971, pp. 1145-1149.

12. Poeschel, R. L., "Primary Electric Propulsion Technology Study," Monthly Report No. 12, 1 Aug. 1978-1 Sept. 1978, Contract NAS 3-21040.

13. Winters, H. F., "Ionic Adsorption and Dissociation Cross Section for Nitrogen," J. Chem. Phys., V. 44, No. 4, pp. 1472-1475, 15 Feb. 1966.

14. Rapp, Donald and Paula Englander-Golden, "Total Cross Sections for Ionization and Attachment in Gases by Electron Impact I. Positive ionization" J. Chem. Phys., V. 43, No. 5, pp. 1464-1479, Sept., 1965.

15. Rapp, Donald, et al., "Cross Sections for Dissociative Ionization of Molecules by Electron Impact," J. Chem. Phys., V. 42, No. 12, pp. 4081-4084, 15 June 1965.

16. Peters, R. R. et al., "A Doubly Charged Ion Model for Ion Thrusters," Journ. Spacecraft and Rockets, V. 14, No. 8, Aug. 1977, pp. 461-468.

17. Wilbur, P. J., "Mercury Ion Thruster Research - 1977," NASA CR-135317, December 1977, pp. 96-104.

18. Knauer, W., et al., "Radial Field Kaufman Thruster," Journ. Spacecraft and Rockets, V. 7, No. 3, March 1970, pp. 248-250.

19. Wilbur, P. J., "Mercury Ion Thruster Research - 1977," NASA CR-135317, December 1977, pp. 105-116.

20. Reader, P. D., "Investigation of a 10 Centimeter Diameter Electron Bombardment Ion Rocket," NASA TN D-1163, 1962.

21. Longhurst, G. R. and P. J. Wilbur, "Multipole Mercury Ion Thruster," AIAA Paper No. 78-682, April 25-27, 1978.

22. Kerslake, W. R., private communication to P. J. Wilbur, January 3, 1979.